

University of St Andrews



Full metadata for this thesis is available in
St Andrews Research Repository
at:

<http://research-repository.st-andrews.ac.uk/>

This thesis is protected by original copyright

Multifractal Analysis and Modelling of Rainfall

A thesis submitted to the University of St. Andrews
for the degree of Doctor of Philosophy

Birger Lammering
8th June 2000



TR
D 690

Acknowledgements

I would like to start by thanking my supervisor Kenneth Falconer, at St Andrews University, for his support, guidance and especially for his patience throughout the past years. I also thank Ian Dwyer, formerly at Institute of Hydrology, Wallingford, and now at NERC, Swindon, for his help and support.

Furthermore, I would like to thank the members of the analysis group at St Andrews University for help and advice. I thank the Global Climate Change group at the Institute of Hydrology for useful discussions and for making the rain data used in chapter 3 available.

A special thank you goes to Birgit for always motivating and distracting me at the right time and to Pia, Kurt and Bernhard for making the time in St Andrews (and in the Scottish mountains) much more enjoyable. Vielen herzlichen Dank an meine Eltern für ihre Unterstützung und Hilfe in allen Lebenslagen. (I also owe a large dept of thanks to my parents for their support and for always being there when they were needed.)

I am very grateful to the European Union for awarding me a Marie Curie Transport and Mobility for Researchers Fellowship. Without this generous funding this degree would not have been possible. I also thank EPSRC and the Institute of Hydrology for their initial funding.

Abstract

In this thesis we study novel aspects of the multifractal properties of rainfall. Our aim is to use multifractal methods to improve the representation of rainfall distributions in climate simulations, in particular by disaggregating spatial rainfall using random cascades. For this we utilise recent mathematical ideas from multifractal analysis, develop computational methods based on these ideas and apply them to the central hydrological question of rainfall representation in climate simulations.

First we present the background to fractal and multifractal theory, with an introduction to the fine, coarse and Legendre transform multifractal spectrum. We consider algorithms for computing the auxiliary function and the Legendre multifractal spectrum, which we test on some measures with well-known multifractal properties. We review the motivation for applying multifractal analysis, in particular random cascade measures, to hydrological problems.

To provide a non-isotropic test example, we introduce and analyse a self-affine measure supported by a variant of the Sierpiński triangle.

As a main application, we incorporate a random cascade disaggregation of spatial rainfall into the hydrological component of the UK Meteorological Office Surface Exchange Scheme and compare the resulting water balance variables with those gained from simulations using more conventional rainfall distributions. We show that a disaggregation using random cascades gives closer values to the reference simulation than the other approaches.

The multifractal properties of random cascades depend on the parameters used in their generation process. We present some simple schemes for estimating parameters that give random cascades with specific multifractal features. These schemes are applied to standard examples and spatial rainfall data. We question the assumption that random cascades are always appropriate for modelling observed multifractals.

In the final chapter we discuss the relationship of the multifractal functions of a plane measure and those of slices of the measure by a line. Based on recent mathematical ideas about the multifractal properties of slices we formulate the ‘slice hypothesis’. We investigate the use of the slice hypothesis to estimate multifractal properties of spatial rainfall fields from data from slices and from temporal data at a fixed site.

I, Birger Lammering, hereby certify that this thesis, which is approximately 29,000 words in length, has been written by me, that it is the record of work carried out by me and that it has not been submitted in any previous application for a higher degree.

date 11/11/2000 signature

I was admitted as a research student in September, 1996 and as a candidate for the degree of Doctor of Philosophy in September, 1997; the higher study for which this is a record was carried out in the University of St. Andrews between 1996 and 2000.

date 11/11/2000 signature

I hereby certify that the candidate has fulfilled the conditions of the Resolution and Regulations appropriate for the degree of Doctor of Philosophy in the University of St. Andrews and that the candidate is qualified to submit this thesis in application for that degree.

date 11/11/2000 signature

In submitting this thesis to the University of St. Andrews I understand that I am giving permission for it to be made available for use in accordance with the regulations of the University Library for the time being in force, subject to any copyright vested in the work not being affected thereby. I also understand that the title and abstract will be published, and that a copy of the work may be made and supplied to any *bona fide* library or research worker.

date 11/11/2000 signature

Contents

1	Background	7
1.1	Fractal and multifractal theory	7
1.1.1	Properties of fractals	7
1.1.2	Multifractal analysis	9
1.1.3	Construction and analysis of fractal sets and multifractal measures	12
1.2	Cascades and random cascades	15
1.2.1	Cascade measures	16
1.2.2	Random cascade measures	16
1.2.3	The multifractal spectrum of a random cascade	18
1.2.4	The random cascade process with discrete weights	19
1.3	Algorithms	20
1.3.1	Basic algorithms	20
1.3.2	Performance of algorithms	22
1.3.3	Techniques to improve box-counting	23
1.3.4	Preliminary results of the algorithms on fractal measures and rainfall data	25
1.4	Hydrological background	36
1.4.1	Theoretical basis for fractal and multifractal rainfall analysis	36
1.4.2	Experimental evidence for fractals and multifractals in rainfall	37
1.4.3	Rainfall representation in circulation models	39
2	Generalised Sierpiński triangles	41
2.1	Matrix estimates	42
2.2	Calculation of box-counting dimensions	44
2.3	Multifractal calculations	47
3	Improvement of water balance in climate simulation by random cascade disaggregation of rainfall	53
3.1	Overview	53
3.2	Background	54
3.3	The model	55
3.4	Model runs	56
3.4.1	Rainfall representations	56
3.4.2	Results	62
3.4.3	Conclusion	67
4	Selection of parameters for the random cascade process	68
4.1	Multifractal random cascades and rainfall distribution	68
4.2	The choice of the cascade probability distribution	69
4.2.1	A scheme with $k = 3$	72
4.2.2	A scheme with $k = 4$	73

4.2.3	A scheme with a general k	74
4.2.4	Results of trials	74
4.3	Limitations of random cascades for representing multifractal processes . . .	78
4.3.1	Inequalities satisfied by the auxiliary function of an N -ary random cascade	80
4.3.2	Moment conditions for an auxiliary function to be reproducible by a random cascade process	82
4.3.3	Conclusion	84
5	Slices of multifractal measures and applications to rainfall distributions	85
5.1	Introduction	85
5.2	Theoretical background	85
5.2.1	Slices of measures	85
5.2.2	Fractal and multifractal properties of slices	86
5.2.3	The slice hypothesis	87
5.2.4	Negative dimensions	87
5.2.5	An example	88
5.3	Computation of slices of measures	89
5.4	Examination of the slice hypothesis using standard examples	90
5.4.1	Random cascade measure	90
5.4.2	Self-similar measure on a Sierpiński triangle	95
5.4.3	Self-affine measure on a generalised Sierpiński triangle	95
5.4.4	Discussion of computational results	98
5.5	The slice hypothesis and rainfall analysis	98
5.5.1	Introduction	98
5.5.2	Slice of a radar composite	102
5.5.3	Temporal observations at a fixed site	102
5.5.4	Discussion	105
6	Conclusions	109

Chapter 1

Background

This chapter gives the general background to multifractal theory, the practical computation of multifractal spectra and multifractal aspects of rainfall.

First we review basic ideas of fractals, in particular box-counting and Hausdorff dimension. This is followed by an introduction to multifractal analysis and the fine, coarse and Legendre transform multifractal spectra. We then examine the multifractal properties of some standard measures, including the random cascade which is of particular interest in hydrological applications. We present a way of generating these measures and calculating their Legendre transformation spectra.

We review various algorithms for calculating the Legendre transform spectrum. Algorithms for use on discrete data and on data defined by a mesh are compared. Some preliminary results on the box-counting algorithms on some standard multifractal measures are given in order to assess which methods are most suitable for later work.

In the final section the basis for applying multifractal analysis and in particular random cascade measures to hydrological problems is reviewed.

1.1 Fractal and multifractal theory

In this section we give basic definitions of fractals, in particular box-counting and Hausdorff dimensions, see Falconer (1990) for more details.

1.1.1 Properties of fractals

A characteristic property of fractals is their scaling behaviour, which is reflected by a power law behaviour of measurements at small scale. For a very basic example we consider an experiment for measuring Norway's coastline. Let r be the length of the ruler and $N(r)$ the number of rulers needed to traverse the coastline. Because of the irregularity of the coastline, $N(r)$ will not be proportional to r^{-1} , but might satisfy a relationship like

$$N(r) \sim r^{-D}, \quad (1.1)$$

when $D > 1$. This exponent D is sometimes termed a *scaling exponent* or *fractal dimension*. More generally, such scaling may be observed if in (1.1) $N(r)$ is one of a variety of measurements of a set at scale r . Certain definitions of fractal dimension are particularly common, and we review some of them.

Box-counting dimension

For practical and computational purposes box-counting dimension is the most frequently used fractal dimension.

Let F be a nonempty bounded subset of \mathbb{R}^d . For $r > 0$, define the r -mesh cubes in \mathbb{R}^d to be the half open cubes of the form $[m_1r, (m_1 + 1)r) \times \cdots \times [m_dr, (m_d + 1)r)$, where $m_1, \dots, m_d \in \mathbb{Z}$. Let $N_r(F)$ be the number of r -mesh cubes intersecting F . The *lower* and *upper box-counting dimension* of F are defined as:

$$\begin{aligned}\underline{\dim}_B F &= \underline{\lim}_{r \rightarrow 0} \frac{\log N_r(F)}{-\log r}, \\ \overline{\dim}_B F &= \overline{\lim}_{r \rightarrow 0} \frac{\log N_r(F)}{-\log r}.\end{aligned}\tag{1.2}$$

If these values are equal, the common value is called the *box-counting* or *box dimension* of F :

$$\dim_B F = \lim_{r \rightarrow 0} \frac{\log N_r(F)}{-\log r}.\tag{1.3}$$

In algorithms for calculating the box-counting dimension the set is usually covered with a grid of cubes with side length r . The number of boxes $N_r(F)$ that intersect F are counted for varying values of r . An estimate of the box-counting dimension is then given by the slope of graph $\log N_r(F)$ against $-\log r$ for $r \rightarrow 0$.

There are many equivalent definitions. For example (1.2)-(1.3) give the same values of the box-counting dimensions if $N_r(F)$ is taken to be the smallest number of sets with diameter r needed to cover F , see Falconer (1990, chapter 3).

Hausdorff dimension

For theoretical analysis Hausdorff dimension is often used. As it is based on measures it is suited for mathematical theory. The disadvantage of Hausdorff dimension is that it is almost impossible to estimate it empirically, since it involves coverings by sets which may be of widely differing sizes, unlike the coverings by boxes of equal size used for box-counting.

We first define Hausdorff measure. An r -covering $\{U_i\}$ of a set $F \subset \mathbb{R}^d$ is a countable collection of sets with $|U_i| \leq r$ that covers the set F , where the diameter of a set is written as $|\cdot|$. Let $s > 0$. The r -pre-measure $\mathcal{H}_r^s(F)$ of F is defined as

$$\mathcal{H}_r^s(F) = \inf \left\{ \sum_{i=1}^{\infty} |U_i|^s : \{U_i\} \text{ is a } r\text{-covering of } F \right\},\tag{1.4}$$

for $r > 0$. As r decreases, $\mathcal{H}_r^s(F)$ increases to a limit, which may be infinite:

$$\mathcal{H}^s(F) = \lim_{r \rightarrow 0} \mathcal{H}_r^s(F),$$

and $\mathcal{H}^s(F)$ is called the s -dimensional Hausdorff measure of F . The measure $\mathcal{H}^s(F)$ is a Borel measure on \mathbb{R}^d .

From (1.4) we can see that \mathcal{H}_r^s is non-increasing in s , if $r < 1$. Moreover for $t > s$ and a r -covering $\{U_i\}$ of F

$$\sum_i |U_i|^t \leq r^{t-s} \sum_i |U_i|^s.\tag{1.5}$$

By taking the infima over all r -coverings $\mathcal{H}_r^t(F) \leq r^{t-s} \mathcal{H}_r^s(F)$. Letting $r \rightarrow 0$, if $\mathcal{H}^s(F) < \infty$ and $t > s$ then $\mathcal{H}^t(F) = 0$. Thus, there is a critical value s where $\mathcal{H}^s(F)$ ‘‘jumps’’ from infinity to zero. This value is called the *Hausdorff dimension* $\dim_H(F)$. Thus,

$$\dim_H(F) = \inf \{s : \mathcal{H}^s(F) = 0\} = \sup \{s : \mathcal{H}^s(F) = \infty\}.\tag{1.6}$$

Relationship to box-counting dimension

If a set F intersects $N_r(F)$ r -mesh cubes with diameter $r\sqrt{d}$, then it follows from (1.4) that

$$\mathcal{H}_{r\sqrt{d}}^s(F) \leq N_r(F)r^s.$$

If $\mathcal{H}^s(F) > 1$ and r is sufficiently small, then $\log N_r(F) + s \log r > 0$ so $s \leq \underline{\lim}_{r \rightarrow 0} [\log N_r(F) / (-\log r)]$ and thus,

$$\dim_H F \leq \underline{\dim}_B F \leq \overline{\dim}_B F.$$

In general these dimensions are not equal; nevertheless for many familiar fractals, including self-similar sets, the Hausdorff and box dimensions coincide.

1.1.2 Multifractal analysis

A measure of widely varying intensity may give rise to a hierarchy of fractals, corresponding to sets of points at which the measure scales with particular exponents. Such measures may have either fractal or non-fractal support. Multifractal analysis attempts to quantify the singularity structure of such measures and study systems where scaling occurs with a range of different power laws; this is usually presented as a “multifractal spectrum”. We give a heuristic description of multifractal spectra adequate for our needs. For more detailed descriptions see Halsey et al. (1986), Falconer (1990, 1997) and Evertsz and Mandelbrot (1992).

Throughout μ will be a Borel measure on \mathbb{R}^d with $0 < \mu(\mathbb{R}^d) < \infty$. Such measures are often thought of as “mass” or “charge” distributions.

The fine multifractal spectrum

With $B(x, r)$ as the ball centred at x with radius r , we define the *local dimension* or *local Hölder exponent* of μ at x by

$$\dim_{\text{loc}} \mu(x) = \lim_{r \rightarrow 0} \frac{\log \mu(B(x, r))}{\log r}, \quad (1.7)$$

provided the limit exists. For each $\alpha > 0$ we consider the set E_α of points x at which $\dim_{\text{loc}} \mu(x) = \alpha$. If E_α is non-empty and fractal over a range of α we think of μ as being a multifractal measure. For such measures we define the *fine multifractal spectrum* or *singularity spectrum* to be $f(\alpha) = \dim_H E_\alpha$.

The fine spectrum has been computed for many theoretical examples. However, it is computationally inaccessible and moreover the limit (1.7) may not exist for many x . Nevertheless, the upper and lower limits may provide information about the singularity spectrum of μ .

The coarse multifractal spectrum

The coarse multifractal spectrum is defined along the lines of box-counting dimension. We write \mathcal{C}_r for the r -mesh cubes, that is the half open cubes in \mathbb{R}^d of the form $[m_1 r, (m_1 + 1)r) \times \cdots \times [m_d r, (m_d + 1)r)$, where $m_1, \dots, m_d \in \mathbb{Z}$. For $\alpha \geq 0$ we write

$$N_r(\alpha) = \#\{r\text{-mesh cubes } B \text{ with } \mu(B) \geq r^\alpha\}. \quad (1.8)$$

The *coarse multifractal spectrum* is defined as

$$f(\alpha) \equiv \lim_{\delta\alpha \rightarrow 0} \lim_{r \rightarrow 0} \frac{\log(N_r(\alpha + \delta\alpha) - N_r(\alpha - \delta\alpha))}{-\log r}, \quad (1.9)$$

if the limit exists. Thus, if $\delta\alpha$ is small, the number of r -mesh cubes B with $r^{\alpha+\delta\alpha} \leq \mu(B) < r^{\alpha-\delta\alpha}$ scales as $r^{-f(\alpha)}$, if r is small.

Using this definition there is an obvious box-counting algorithm for estimating the coarse multifractal spectrum of data sets, called the *Histogram method*, see section 1.3.1. The variable α is subdivided into intervals by points $0 < \alpha_0 < \alpha_1 < \dots < \alpha_{\max}$. A histogram is created of numbers of squares B such that

$$r^{\alpha_{k+1}} \leq \mu(B) < r^{\alpha_k},$$

for small r , so that $\log[N(\alpha_{k+1}) - N(\alpha_k)] / -\log r$ is an estimate for $f(\alpha_k)$.

The Legendre transform formalism

The Legendre transform formalism was introduced by Halsey et al. (1986) and is also known as the *Method of Moments*, an expression that originates from statistical mechanics where parallel methods occur. This involves calculations of a spectrum as the Legendre transform of a function defined in terms of moment sums. Under reasonable conditions the spectrum is the same as the fine and the coarse multifractal spectra. A more detailed motivation of this method can be found in Falconer (1990) and Evertsz and Mandelbrot (1992).

We define a *partition function* or *moment sum* $\mathcal{M}_r(q)$ using box-counting over the r -mesh cubes \mathcal{C}_r ,

$$\mathcal{M}_r(q) = \sum_{B \in \mathcal{C}_r} \mu(B)^q, \quad (1.10)$$

with the convention that $0^q = 0$ for all q . For $q > 0$ most weight is given to regions of dense measure, while negative moments reflect scaling of the distribution in sparse regions.

We define the *multifractal auxiliary function* β by

$$\beta(q) = \lim_{r \rightarrow 0} \frac{\log \mathcal{M}_r(q)}{-\log r}, \quad (1.11)$$

assuming the limit exists. Note that many authors, especially in the physics literature, use $\tau(q) = -\beta(q)$ as the auxiliary function (Borgani et al., 1993; Halsey et al., 1986).

For $\alpha > 0$ assume that the number of r -cubes B with $r^{\alpha+\delta\alpha} \leq \mu(B) < r^\alpha$ is of the order $r^{-f(\alpha)}\delta\alpha$ for small r . Approximating (1.10) by an integral

$$\begin{aligned} \mathcal{M}_r(q) &\simeq \int_0^\infty r^{q\alpha} r^{-f(\alpha)} d\alpha \\ &= \int_0^\infty r^{q\alpha - f(\alpha)} d\alpha \\ &\sim r^{-\sup(f(\alpha) - q\alpha)}, \end{aligned} \quad (1.12)$$

since the dominant contribution to the integral for small r occurs near values of α for which $f(\alpha) - q\alpha$ is largest.

Thus, we might expect that

$$\beta(q) = \sup_{\alpha} (f(\alpha) - q\alpha), \quad (1.13)$$

with

$$\mathcal{M}_r(q) \sim r^{-\beta(q)}. \quad (1.14)$$

It is sometimes convenient to work with the *generalised dimension* D_q defined by

$$D_q = \beta(q)/(1 - q), \quad (1.15)$$

for $q \neq 1$, rather than with $\beta(q)$ itself. Note that $0 \leq D_q \leq d$, with $D_q = d$ if μ is the d -dimensional volume measure on a bounded subset of \mathbb{R}^d , see for example McCauley (1993).

If we assume that the supremum in (1.13) is attained at $\alpha = \alpha(q) > 0$ and that f is differentiable, then

$$\frac{d}{d\alpha}(f(\alpha) - q\alpha) = 0,$$

so

$$q = \frac{df}{d\alpha}(\alpha(q)). \quad (1.16)$$

From (1.13)

$$\beta(q) = f(\alpha(q)) - q\alpha(q), \quad (1.17)$$

so assuming that the functions involved are sufficiently smooth we get, using (1.16), that

$$\frac{d\beta}{dq}(q) = \frac{df}{d\alpha}(\alpha(q)) \frac{d\alpha}{dq} - q \frac{d\alpha}{dq} - \alpha(q) = -\alpha(q). \quad (1.18)$$

Thus,

$$\alpha(q) = -\frac{d\beta}{dq}(q) \quad (1.19)$$

and

$$f(\alpha(q)) = \beta(q) + q\alpha(q) = \beta(q) - q \frac{d\beta}{dq}(q), \quad (1.20)$$

which is a Legendre transformation which transforms the independent variables β and q to the independent variables f and α . The function $f(\alpha)$ defined in this way is called the *Legendre spectrum* of μ .

This motivates the approach of obtaining a multifractal spectrum by finding $\beta(q)$ given by (1.11) and calculating its Legendre transform.

From (1.16) and (1.19),

$$\frac{d^2 f}{d\alpha^2}(\alpha(q)) = \frac{dq}{d\alpha} = \left(\frac{d\alpha}{dq}\right)^{-1} = -\left(\frac{d^2 \beta}{dq^2}\right)^{-1} < 0,$$

so the function f is concave in α . By (1.16) $f(\alpha)$ has a maximum corresponding to $q = 0$, and by (1.10) $f(\alpha) = D_0$, the box dimension of the support of μ .

When $q = 1$, $\mathcal{M}_r(1) = 1$ for all r , so $\beta(1) = 0$, $\frac{df}{d\alpha}(\alpha(q)) = 1$ and $\alpha(1) = f(\alpha(1))$. At $q = 1$ the line $f(\alpha) = \alpha$ is tangent to the curve of $f(\alpha)$. At this point $f(\alpha)$ gives us the *information dimension* D_1 , which is the dimension of the set on which μ is concentrated. The ends of the range of α for which $f(\alpha)$ is defined correspond to $q = \infty$ and $q = -\infty$. These points are marked in figure 1.1.

We emphasise that this treatment is heuristic and depends on several limiting processes working nicely. However many examples are known when this formalism is valid and where the fine, coarse and the Legendre spectrum are equal, see Falconer (1990, 1997), Evertsz and Mandelbrot (1992) and Olsen (2000).

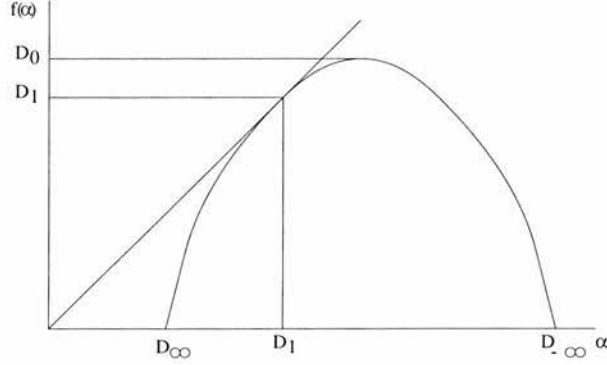


Figure 1.1: Properties of the $f(\alpha)$ curve

1.1.3 Construction and analysis of fractal sets and multifractal measures

Iterated function systems

A way of constructing many fractals including self-similar and self-affine sets is by using iterated function systems. An *iterated function system* (IFS) is a family of contractions $\{S_1, \dots, S_m\}$ with $S_i : \mathbb{R}^d \rightarrow \mathbb{R}^d$, that is, maps for which there exist $0 < r_i < 1$ such that $|S_i(x) - S_i(y)| \leq r_i|x - y|$ for all $x, y \in \mathbb{R}^d$. Given an IFS there is a non-empty compact set F such that

$$F = \bigcup_{i=1}^m S_i(F), \quad (1.21)$$

called the *attractor* or *invariant set* for the S_i , see Falconer (1990, section 9.1). If the IFS consists of similarities, the attractor is called a *self-similar set*, if it consists of affine maps then F is called a *self-affine set*.

Let J_k denote the collection of all k -term sequences formed using the integers $1, \dots, m$. Thus, compositions of the S_i may be coded by $\mathbf{i} \equiv (i_1, \dots, i_k) \in J_k$, where $i_j \in \{1, \dots, m\}$ for all j , with

$$S_{\mathbf{i}} = S_{i_1} \circ S_{i_2} \circ \dots \circ S_{i_k}. \quad (1.22)$$

If D is an initial non-empty compact set such that $S_i(D) \subset D$ for $i = 1, 2, \dots, m$, we may construct F as the intersection of a nested sequence of sets, with

$$F = \bigcap_{k=1}^{\infty} \bigcup_{\mathbf{i} \in J_k} S_{\mathbf{i}}(D). \quad (1.23)$$

When the union (1.21) is disjoint we say the IFS $\{S_1, \dots, S_m\}$ satisfies the *strong separation condition* (SSC). This condition is too strong for many purposes, therefore we sometimes use a weaker separation condition: the IFS $\{S_1, \dots, S_m\}$ satisfies the *open set condition* (OSC) if there exists a bounded non-empty open set U such that

$$U \supseteq \bigcup_{i=1}^m S_i(U),$$

with this union disjoint.

In the case of an IFS consisting of similarities S_i with contraction ratios r_i , the value of s given by

$$\sum_{i=1}^m r_i^s = 1 \quad (1.24)$$

is the Hausdorff and box-counting dimension of the self-similar set F provided that F satisfies either the strong separation or open set condition, see Falconer (1990, section 9.2).

Example: Sierpiński triangle The IFS with similarities $S_1, S_2, S_3 : \mathbb{R}^2 \rightarrow \mathbb{R}^2$

$$\begin{aligned} S_1 \begin{bmatrix} x_1 \\ x_2 \end{bmatrix} &= \begin{bmatrix} 0.5 & 0 \\ 0 & 0.5 \end{bmatrix} \begin{bmatrix} x_1 \\ x_2 \end{bmatrix} + \begin{bmatrix} 0 \\ 0.5 \end{bmatrix} \\ S_2 \begin{bmatrix} x_1 \\ x_2 \end{bmatrix} &= \begin{bmatrix} 0.5 & 0 \\ 0 & 0.5 \end{bmatrix} \begin{bmatrix} x_1 \\ x_2 \end{bmatrix} + \begin{bmatrix} 0 \\ 0 \end{bmatrix} \\ S_3 \begin{bmatrix} x_1 \\ x_2 \end{bmatrix} &= \begin{bmatrix} 0.5 & 0 \\ 0 & 0.5 \end{bmatrix} \begin{bmatrix} x_1 \\ x_2 \end{bmatrix} + \begin{bmatrix} 0.5 \\ 0 \end{bmatrix}, \end{aligned} \tag{1.25}$$

has the Sierpiński triangle as attractor, see figure 1.2. This IFS satisfies the OSC but

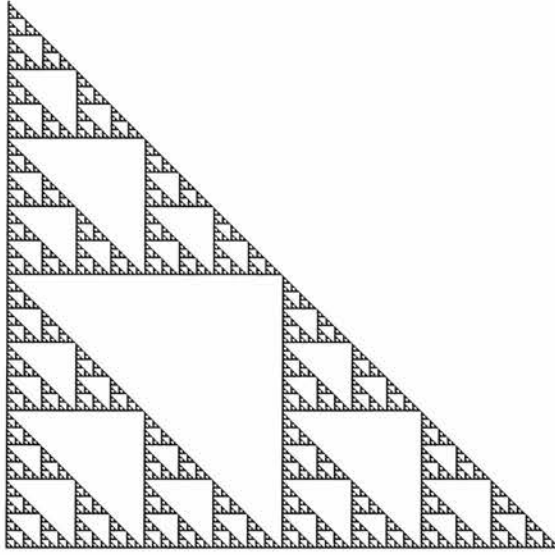


Figure 1.2: Sierpiński triangle

not the SSC and has Hausdorff and box-counting dimension $\log 3 / \log 2$ using (1.24). A generalised version of the Sierpiński triangle is considered in chapter 2.

Weighted iterated function systems

Weighted iterated function systems are used to generate measures, just as iterated function systems are used to generate sets.

A *weighted iterated function system* (WIFS) consists of a family of contractions $\{S_1, S_2, \dots, S_m\}$ with $S_i : \mathbb{R}^d \rightarrow \mathbb{R}^d$ and associated weights $\{w_1, w_2, \dots, w_m\}$ with $w_i > 0$ and $\sum w_i = 1$. Then there exists an unique probability measure μ with $\mu(\mathbb{R}^d) = 1$, called the *attractor* of the WIFS, that is invariant in the sense that

$$\mu(B) = \sum_{i=1}^m w_i \mu(S_i^{-1}(B)) \tag{1.26}$$

for all sets $B \in \mathbb{R}^d$, see, for example, Falconer (1997). Note that some authors refer to WIFSs as *probabilistic iterated function systems* or *iterated function systems with probabilities*.

The support of μ is the IFS attractor of $\{S_1, \dots, S_m\}$. Attractors of WIFSs provide basic examples of multifractal measures, which in general have nontrivial multifractal spectra. The measure μ is called *self-similar*, respectively *self-affine*, if the S_i are similarity, respectively affine, transformations.

We may regard μ as being constructed by the process of *repeated subdivision*. If $\{S_1, S_2, \dots, S_m\}$ satisfies a strong separation or open set condition, let D be a region, that is the closure of an open set, such that $S_1(D), \dots, S_m(D)$ are disjoint, except possibly at the boundaries. This leads to a nested family of sets $\{S_{i_1} \circ S_{i_2} \circ \dots \circ S_{i_k}(D)\}$, with $S_{i_1} \circ S_{i_2} \circ \dots \circ S_{i_k}(D) \supset \cup_{i=1}^m S_{i_1} \circ S_{i_2} \circ \dots \circ S_{i_k} \circ S_i(D)$, with this union disjoint except possibly at the boundaries, provided the S_i are reasonable maps. We define

$$\mu(S_{i_1} \circ S_{i_2} \circ \dots \circ S_{i_k}(D)) = w_{i_1} w_{i_2} \dots w_{i_k},$$

so that the mass of $S_{i_1} \circ \dots \circ S_{i_k}(D)$ is divided between $S_{i_1} \circ \dots \circ S_{i_k} \circ S_i(D)$ in the ratios w_i ($1 \leq i \leq m$). It is clear that μ is additive on finite unions of sets of the form $\{S_{i_1} \circ \dots \circ S_{i_k}(D) : \{i_1, \dots, i_k\} \in J_k\}$, and μ extends to a Borel measure on \mathbb{R}^d supported by the attractor F . Under reasonable conditions, including if the S_i are similarities or affinities, μ is just the attractor of the WIFS, as above.

Under suitable conditions it is possible to calculate the multifractal spectrum of a self-similar WIFS attractor. Provided the S_i satisfy a separation condition such as the strong separation condition or open set condition, the auxiliary function β (see (1.13)) is given by

$$\sum_{i=1}^m w_i^q r_i^{\beta(q)} = 1, \quad (1.27)$$

see Arbeiter and Patzschke (1996) and Falconer (1997). Then $f(\alpha)$ may be found parametrically by Legendre transformation using (1.19) and (1.20), and it turns out that this indeed gives the coarse and the fine multifractal spectra.

Example: Binomial measure on middle-third Cantor set Let $S_1, S_2 : \mathbb{R} \rightarrow \mathbb{R}$ be given by

$$\begin{aligned} S_1(x) &= \frac{1}{3}x, \\ S_2(x) &= \frac{1}{3}x + \frac{2}{3} \end{aligned} \quad (1.28)$$

and consider the WIFS $\{S_1, S_2\}$ with weights $\{w, 1-w\}$, where $0 < w < 1$. The IFS attractor F is the middle-third Cantor set and the WIFS attractor μ is a binomial measure supported by F , see figure 1.3.

From (1.27)

$$\beta(q) = \lim_{r \rightarrow 0} \frac{\log \mathcal{M}_r(q)}{-\log r} = \frac{\log(w^q + (1-w)^q)}{\log 3}.$$

The multifractal spectrum $f(\alpha)$ may be obtained in terms of parameter q by Legendre transformation of β using (1.19) and (1.20):

$$f(\alpha(q)) = \frac{\log(w^q + (1-w)^q) - \frac{q(w^q \log w + (1-w)^q \log(1-w))}{w^q + (1-w)^q}}{\log 3} \quad (1.29)$$

$$\alpha(q) = -\frac{w^q \log w + (1-w)^q \log(1-w)}{(w^q + (1-w)^q) \log 3}.$$

It may be shown that this gives both the coarse and fine multifractal spectra of μ , see Falconer (1990, chapter 17).

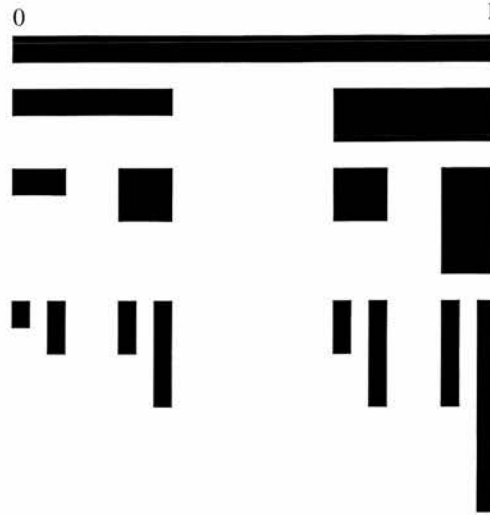


Figure 1.3: Construction by repeated subdivision of a multifractal multinomial measure on the middle-third Cantor set

Example: Self-similar measure on the Sierpiński triangle For a self-similar measure on the Sierpiński triangle with $\{S_1, S_2, S_3\}$ as in (1.25) and weights $\{w_1, w_2, w_3\}$, we get

$$\beta(q) = \frac{\log(w_1^q + w_2^q + w_3^q)}{\log 2}. \quad (1.30)$$

As with the binomial measure on the Cantor set, $f(\alpha)$ may be obtained parametrically by Legendre transform. In chapter 2 we generalise this to self-affine measures on generalised Sierpiński triangles. Multifractal analysis for certain self-affine measures based on Sierpiński carpets (obtained by repeated subdivision of rectangles into rectangles) is addressed in King (1995); Olsen (1998b).

Sets and measures generated by the chaos game

The *chaos game* (Peitgen et al., 1992) is an algorithm to approximate the attractor of an IFS (1.21) and the measure defined by a WIFS. Let $\{S_1, \dots, S_m\}$, $\{w_1, \dots, w_m\}$ be a WIFS and choose an initial point z_0 . For $n = 1, 2, \dots$ select an independent random integer j_n with $1 \leq j_n \leq m$ such that $j_n = j$ with probability w_j , and set $z_n = S_{j_n}(z_{n-1})$. Plotting the sequence $\{z_n\}$ gives approximations to F ; we omit the first few iterations to allow the sequence to reach the attractor if $z_0 \notin F$. The invariant measure of the WIFS satisfying (1.26) is approximated by the proportion of z_i lying in a set. More precisely

$$\mu(A) = \lim_{n \rightarrow \infty} \frac{1}{n} \{\#i : 1 \leq i \leq n \text{ and } z_i \in A\}$$

for $A \subset \mathbb{R}^d$ with probability one. A measure defined in this way is called *residence measure*. The chaos game can be used in numerical simulation of the invariant measure of an WIFS and thus in estimation of its multifractal spectrum.

1.2 Cascades and random cascades

Random cascade processes provide measures or mass distributions commonly used for simulating spatial and temporal rainfall distributions. Cascades are special cases of WIFSs and the construction may be realised as described below.

1.2.1 Cascade measures

Let $C_0 = [0, 1]^d$ be the d -dimensional unit cube (meaning an interval if $d = 1$ and a square if $d = 2$). We fix an integer $N \geq 2$, the *subdivision number*, and set $m = N^d$, the *branching number*. We divide C_0 into m closed sub-cubes C_1, \dots, C_m of sides N^{-1} in the natural way. We divide each of these cubes C_i into m closed sub-cubes $C_{i,1}, \dots, C_{i,m}$ of side length N^{-2} . Continuing in this way we get a nested family of cubes with sides parallel to the coordinate planes. Thus, there are m^k k -th level cubes each of side length N^{-k} .

There is a natural coding of the cubes. Let $J_k = \{(i_1, \dots, i_k) : 1 \leq i_j \leq m\}$ denote the collection of all k -term sequences formed using the integers $1, \dots, m$ and set $J = \cup_0^\infty J_k$ for the set of all such sequences. For convenience we sometimes write $\mathbf{i} \equiv (i_1, \dots, i_k) \in J_k$. The cubes in the construction are indexed by J . Thus, each k -th level cube C_{i_1, \dots, i_k} is a union of the $(k+1)$ -th level cubes $C_{i_1, \dots, i_k, 1}, \dots, C_{i_1, \dots, i_k, m}$, where the sub-cubes are ordered in the same pattern in each case. We write \mathcal{C}_k for the set of k -th level cubes.

We use this nested family of cubes to construct a measure on $[0, 1]^d$. Let $\{w_1, \dots, w_m\}$ be a set of weights, where $0 \leq w_i < 1$ and $\sum_i^m w_i = 1$. We define μ by repeated subdivision, by defining $\mu(C_{i_1, i_2, \dots, i_k}) = w_{i_1} w_{i_2} \dots w_{i_k}$, and as before this extends to a (Borel) measure μ on $[0, 1]^d$. Clearly, μ is a self-similar measure which is the attractor of the WIFS $\{S_1, \dots, S_m\}, \{w_1, \dots, w_m\}$, where the S_i are similarity transformations of ratios $1/N$ that preserve orientation, and the OSC holds with $U = (0, 1)^d$.

For example, for a 2×2 subdivision, with $d = 2$ and $N = 2$ we have

$$\begin{aligned} S_1 \begin{bmatrix} x_1 \\ x_2 \end{bmatrix} &= \begin{bmatrix} 0.5 & 0 \\ 0 & 0.5 \end{bmatrix} \begin{bmatrix} x_1 \\ x_2 \end{bmatrix} + \begin{bmatrix} 0 \\ 0 \end{bmatrix} \\ S_2 \begin{bmatrix} x_1 \\ x_2 \end{bmatrix} &= \begin{bmatrix} 0.5 & 0 \\ 0 & 0.5 \end{bmatrix} \begin{bmatrix} x_1 \\ x_2 \end{bmatrix} + \begin{bmatrix} 0 \\ 0.5 \end{bmatrix} \\ S_3 \begin{bmatrix} x_1 \\ x_2 \end{bmatrix} &= \begin{bmatrix} 0.5 & 0 \\ 0 & 0.5 \end{bmatrix} \begin{bmatrix} x_1 \\ x_2 \end{bmatrix} + \begin{bmatrix} 0.5 \\ 0 \end{bmatrix} \\ S_4 \begin{bmatrix} x_1 \\ x_2 \end{bmatrix} &= \begin{bmatrix} 0.5 & 0 \\ 0 & 0.5 \end{bmatrix} \begin{bmatrix} x_1 \\ x_2 \end{bmatrix} + \begin{bmatrix} 0.5 \\ 0.5 \end{bmatrix}. \end{aligned} \tag{1.31}$$

The support of μ is the IFS attractor of the family $\{S_i : w_i > 0\}$. For the support to be fractal at least one of the w_i must be 0. From (1.27) we get $\beta(q) = \log \sum_{i=1}^4 w_i^q / \log 2$, and as before Legendre transform gives the coarse and the fine spectra of μ .

1.2.2 Random cascade measures

A *self-similar random cascade measure* is created by using the same IFS as in the construction of the weighted cascade, but with weights given by random variables.

We use the family of nested cubes introduced in section 1.2.1 to define a random measure or mass on C_0 in a statistically self-similar way. We do this by defining $\mu_k(C_{i_1, \dots, i_k})$ for each k -th level cube C_{i_1, \dots, i_k} and using a limiting process to obtain a measure μ on $[0, 1]^d$. Let (W_1, W_2, \dots, W_m) be a random variable vector which will define the ratios between the masses of cubes and their sub-cubes in a statistically self-similar way.

We require the (W_1, W_2, \dots, W_m) to fulfil the following conditions:

1. There exist numbers m_- and m_+ , $0 < m_- \leq m_+ < 1$, such that for all i almost surely

$$\text{either } W_i = 0 \text{ or } m_- \leq W_i \leq m_+. \tag{1.32}$$

2. The mass is conserved on average, that is

$$\mathbb{E}\left(\sum_{i=1}^m W_i\right) = 1. \quad (1.33)$$

For each $(i_1, \dots, i_k) \in J_k$ let $(W_{i_1, \dots, i_k, 1}, \dots, W_{i_1, \dots, i_k, m})$ be a random vector with identical distribution to (W_1, \dots, W_m) independent for each (i_1, \dots, i_k) . We define \mathcal{S}_k to be the (finite) σ -field consisting of all unions of k -th level cubes C_{i_1, \dots, i_k} . We define a random set function μ_k on \mathcal{S}_k for $k = 0, 1, 2, \dots$ inductively. We set $\mu_0([0, 1]^d) = 1$. Assuming that μ_k has been defined on \mathcal{S}_k we define μ_{k+1} on \mathcal{S}_{k+1} as follows. Let $C_{i_1, \dots, i_k} \in \mathcal{C}_k$. For $i = 1, 2, \dots, m$ set

$$\mu_{k+1}(C_{i_1, \dots, i_k, i}) = \mu_k(C_{i_1, \dots, i_k})W_{i_1, \dots, i_k, i}, \quad (1.34)$$

where $(W_{i_1, \dots, i_k, 1}, \dots, W_{i_1, \dots, i_k, m})$ is the random vector introduced above. We extend μ_{k+1} to finite unions of the $(k+1)$ -level cubes, that is to \mathcal{S}_{k+1} , by addition.

We claim that μ_k tends to a limiting random measure μ on $[0, 1]^d$ in an appropriate sense. This follows from the martingale convergence theorem which may be used to show that, for every cube C of the construction, $\mu_k(C)$ converges almost surely as $k \rightarrow \infty$. We write \mathcal{F}_k for the σ -field underlying the probability distribution of the random variables $\{W_i : |i| \leq k\}$.

Let $C = C_{i_1, \dots, i_j} \in \mathcal{C}_j$. It follows from (1.33) and statistical self-similarity that $(\mu_k(C), \mathcal{F}_k)_{k \geq j}$ is a martingale, that is

$$\mathbb{E}(\mu_{k+1}(C) | \mathcal{F}_k) = \mu_k(C), \quad (1.35)$$

for $k \geq j$, where $\mathbb{E}(\mu_{k+1}(C) | \mathcal{F}_k)$ is the conditional expectation of $\mu_{k+1}(C)$ given \mathcal{F}_k . To check this, note that for all i_1, \dots, i_k ,

$$\begin{aligned} \mathbb{E}(\mu_{k+1}(C_{i_1, \dots, i_k}) | \mathcal{F}_k) &= \mathbb{E}\left(\sum_{i=1}^m \mu_{k+1}(C_{i_1, \dots, i_k, i}) \Big| \mathcal{F}_k\right) \\ &= \mathbb{E}\left(\mu(C_{i_1, \dots, i_k}) \sum_{i=1}^m W_{i_1, \dots, i_k, i} \Big| \mathcal{F}_k\right) \\ &= \mu_k(C_{i_1, \dots, i_k}) \mathbb{E}\left(\sum_{i=1}^m W_{i_1, \dots, i_k, i}\right) \\ &= \mu_k(C_{i_1, \dots, i_k}) \mathbb{E}\left(\sum_{i=1}^m W_i\right) \\ &= \mu_k(C_{i_1, \dots, i_k}), \end{aligned}$$

by using independence and (1.33). Summing over the k -th level cubes in $C \in \mathcal{C}_j$ gives (1.35), so $(\mu_k(C), \mathcal{F}_k)_{k \geq j}$ is a non-negative martingale. By the martingale convergence theorem $\mu_k(C)$ converges almost surely to a finite number $\mu(C)$ for each $C \in \mathcal{C}_j$.

For each j , if $k \geq j$, μ_k is additive on \mathcal{S}_j , so μ is additive on \mathcal{S}_j for each j almost surely. By the usual limiting process for measures we have almost surely that μ is a measure on the σ -field generated by $\cup_i^\infty \mathcal{S}_j$, that is on the Borel subsets of $[0, 1]^d$.

With a little effort $(\mu_k(C) | \mathcal{F}_k)_{k \geq j}$ may be seen to be a square integrable martingale, that is $\sup_k \mathbb{E}(\mu_k(C)^2) < \infty$ (Falconer, 1990, 1997; Olsen, 1995). This implies that with positive probability $\mu(C) > 0$ and in particular $\mu([0, 1]^d) > 0$.

If we allow the W_i to be 0 with positive probability, then there is a positive probability of extinction, that is $\mu_k([0, 1]^d) = 0$ for sufficiently large k , so $\mu([0, 1]^d) = 0$. In fact $\mu([0, 1]^d) = 0$ if and only if the branching process with distribution

$$\Pr(\# \text{ offspring} = n) = \Pr(\{\#i : W_i > 0\} = n) \quad (1.36)$$

becomes extinct. By standard branching process theory, see for example Grimmett and Stirzaker (1982), the probability of this extinction p_e is the smallest non-negative root of the equation $G(s) = s$, where $G(s)$ is the generating function of the process, that is

$$G(s) = \sum_{n=0}^{\infty} \Pr(\# \text{ offspring} = n) s^n. \quad (1.37)$$

In particular, if $\mathbb{E}(\# \text{ offspring}) > 1$ then $p_e < 1$.

1.2.3 The multifractal spectrum of a random cascade

In this section we summarise the multifractal behaviour of the random measure μ generated by the random cascade process described in the previous section. Technical details may be found in Falconer (1990), Olsen (1995) and Arbeiter and Patzschke (1996).

Given (W_1, \dots, W_m) satisfying (1.32) and (1.33) we define $\beta(q)$ by

$$1 = \mathbb{E} \left(\sum_{i=1}^m W_i^q N^{-\beta(q)} \right), \quad (1.38)$$

that is

$$\beta(q) = \frac{\log \mathbb{E}(\sum_{i=1}^m W_i^q)}{\log N}. \quad (1.39)$$

Conditional on the non-extinction of the random cascade process, the auxiliary function of μ , see (1.11), is almost surely given by this β . (Note that (1.38) is a random analogue of the formula (1.27) for $\beta(q)$ of a self-similar set.) This again may be shown using the martingale convergence theorem. Briefly, this is achieved by considering the random moment sum

$$U_r = U_{q,\beta}^r = \left(\sum_{|i|=r} (W_i)^q \right) (N^{-r})^{\beta(q)}.$$

With β given by (1.38), a calculation using the statistical self-similarity of the random cascade construction gives

$$\mathbb{E}(U_{r+1} | \mathcal{F}_r) = U_r. \quad (1.40)$$

By the martingale convergence theorem $U_r \rightarrow U$ for some random variable U where a.s. $U < \infty$ and $0 < U$ in the case of non-extinction. It follows in this case that $\log \mathcal{M}_r(q) / -\log(r) \rightarrow \beta(q)$ where $\mathcal{M}_r(q)$ is the moment sum (1.10). It may be shown, see Arbeiter and Patzschke (1996), that in this situation the Legendre transform of β equals the coarse and fine multifractal spectrum of μ .

1.2.4 The random cascade process with discrete weights

To provide statistical homogeneity it is convenient to simplify the random cascade process by choosing the W_i to be identical and independently distributed, with the distribution of a random variable W , say. Thus from (1.39),

$$\beta(q) = \frac{\log(m\mathbb{E}(W^q))}{\log N} = \frac{\log(m \int h(t)t^q dt)}{\log N}, \quad (1.41)$$

if W has the probability distribution function $h(t)$.

Moreover, for computational and mathematical convenience, we often take W to be a discrete random variable. Thus, letting $0 = a_0 < a_1 < \dots < a_k$ be numbers and p_0, \dots, p_k be probabilities, so $p_0 \geq 0$ and $p_1, p_2, \dots, p_k > 0$ with

$$\sum_{j=0}^k p_j = 1 \quad (1.42)$$

and

$$m \sum_{j=0}^k p_j a_j = 1, \quad (1.43)$$

from (1.32) and (1.33), we define the W by

$$\Pr(W = a_j) = p_j. \quad (1.44)$$

We term a cascade process of this form a *random cascade process with discrete weights*.

The distribution of cubes in this construction assigned zero measure depends only on the parameter p_0 . Hence, the fractal dimension of the support of μ and the probability of total extinction p_e depends only on p_0 . There is a positive probability of extinction, that is $\mu([0, 1]^d) = 0$, if $p_0 > 0$. Recall that the probability p_e is the smallest non-negative root of the equation $G(s) = s$, where $G(s)$ is the generating function of the associated branching process, that is

$$G(s) = \sum_{n=0}^m (1 - p_0)^n p_0^{m-n} \binom{m}{n} s^n, \quad (1.45)$$

see (1.37). A branching process argument gives that the expected number of l -th level cubes with positive measure is

$$[m(1 - p_0)]^l, \quad (1.46)$$

where $m = N^d$ is the branching number. The dimension of the support of μ conditional on non-extinction is

$$\dim_H \text{spt}\mu = \dim_B \text{spt}\mu = \frac{\log m(1 - p_0)}{\log N}, \quad (1.47)$$

provided $m(1 - p_0) > 0$.

With W given by (1.44) we get for the multifractal auxiliary function using (1.41)

$$\beta(q) = \frac{\log(m \sum_{i=0}^k p_i a_i^q)}{\log N}. \quad (1.48)$$

(As always we follow the convention $0^q = 0$ for all q .) The multifractal spectrum is then given parametrically using (1.19) and (1.20) as

$$\alpha(q) = -\frac{d\beta(q)}{dq} = \frac{-\sum_{i=0}^k p_i a_i^q \log a_i}{\log N \sum_{i=0}^k p_i a_i^q} \quad (1.49)$$

$$f(\alpha(q)) = \beta(q) + q\alpha(q). \quad (1.50)$$

1.3 Algorithms

The work in this thesis involves substantial computations of auxiliary functions $\beta(q)$ and multifractal spectra $f(\alpha)$ from empirical data. In this section we review the computational algorithms available for determining these functions. We first make some general remarks on estimating the multifractal properties of “real life data”.

The data sets can be classified as two types, discrete data sets and data sets supported by an r -mesh. A discrete data set consists of a sequence of points in \mathbb{R}^d with the density of points representing the measure. Examples include the outcomes of the chaos game, see section 1.1.3, and of iterated data from dynamical systems. The other method of presenting data is by recording the measure of every grid cube in an r -mesh \mathcal{C}_r , see section 1.1.2, for some suitably small r . For example, most experimental data, such as rainfall radar images or time series, are presented in this form.

All algorithms presented in this section have in common that the slope of a log-log plot has to be estimated. This kind of calculation is delicate, since the presentation of data in a log-log plot tends to over-emphasise the correlation between the axes.

Theoretical multifractal analysis relies on taking limits as the scale approaches 0. Real life data is only available over a finite range of scales, and scale limits have to be inferred by extrapolation. Such approximations become better on increasing the size of the data sets to enable finer scales to be considered. Unfortunately it can be difficult to obtaining large enough data sets in applications such as hydrology.

The scaling regime of multifractals, that is the range over which the log-log plot is linear, is limited. Sometimes there may be several scaling regimes each with a different scaling behaviour, with *phase transitions* between one and the next. It therefore can be difficult to automate the analysis of log-log plots reliably in the algorithms.

Note that each method leads to a function $f(\alpha)$ that gives some quantification of fractality. However such $f(\alpha)$ need not to be the same for different algorithms, though for many standard theoretical examples that have been analysed they are often equal.

1.3.1 Basic algorithms

We outline the main algorithms that have been used in multifractal analysis. Some further refinements will be made in subsequent sections.

Histogram method This method is the most direct way to calculate the coarse grained multifractal spectrum $f(\alpha)$ of μ by directly using the definition (1.9) of $f(\alpha)$.

The measure μ is coarse grained with an r -mesh of cubes B . The range of α is subdivided into intervals of suitably small size $\delta\alpha$ by points $\alpha_0 < \alpha_1 < \dots < \alpha_N$. The local Hölder exponents α of the measure $\mu(B)$ on the mesh cubes are estimated by $\alpha = \log \mu(B) / \log r$. The number $N_r(\alpha_k)$ of cubes for which $\alpha_k \leq \alpha < \alpha_{k+1}$ is stored. The procedure is repeated for several values of r . The multifractal spectrum can be estimated using (1.9) by plotting an estimate of $\log N_r(\alpha) / \log r$ aggregated from a range of values of r against α .

This method is easy to implement and does not rely on Legendre transformations. On the other hand it converges very slowly for some standard measures. Therefore this method is usually not used for the estimation of the $f(\alpha)$ spectrum from physical data. The histogram method is described, for example, in Evertsz and Mandelbrot (1992).

The remaining methods calculate the multifractal auxiliary function $\beta(q)$ using some *partition function*, from which an $f(\alpha)$ may be found using Legendre transformation.

Method of moments The method of moments is the most widely used algorithm for estimating the multifractal spectrum. The most common partition function is the standard box-counting sum

$$\mathcal{M}_r(q) = \sum_{B \in \mathcal{C}_r} \mu(B(r))^q, \quad (1.51)$$

where \mathcal{C}_r is the family of r -mesh cubes. This is the natural way of estimating the partition sum from a measure (see sect 1.1.2). Following (1.11) we estimate for each fixed q

$$\beta(q) = \lim_{r \rightarrow 0} \frac{\log \mathcal{M}_r(q)}{-\log(r)} \quad (1.52)$$

by finding $\mathcal{M}_r(q)$ for a set of small values of r and estimating the slope of the log-log graph with linear regression.

In practice $\mathcal{M}_r(q)$ is estimated by coarse graining μ with an r -mesh. The range of r depends strongly on the resolution of the data. The range of q may be chosen arbitrarily depending on the application, with the values of greatest interest being typically $-5 < q < 5$. The limit in (1.52) is approximated by linear regression using a range of small r . The finer the data mesh, the greater is the number of regression points possible in the log-log plots and hence the greater the accuracy. By inspecting these log-log plots we can assess the quality of the scaling. In particular we can detect phase transitions, that is sudden discontinuities in the scaling exponents. For each q , the error of the regression is an indicator of the quality of the scaling. For larger $|q|$ the slope describes the scaling of μ in regions with very high, respectively very low, density. Such regions are typically very small and hence require a finer grid of boxes in order to detect them accurately. This leads to greater errors for the regression of the log-log plots for large $|q|$ than for small $|q|$. Although $\frac{\log \mathcal{M}_r(q)}{-\log(r)}$ is convex in q for each r , the regression process means that the estimates for $\lim_{r \rightarrow 0} \frac{\log \mathcal{M}_r(q)}{-\log(r)}$ need not be convex in q , particularly when the $\frac{\log \mathcal{M}_r(q)}{-\log(r)}$ are close to linear in q .

Correlation integral method If μ is a probability measure on \mathbb{R}^n and $q > 0$, it may be shown (Grassberger and Procaccia, 1983; Pesin, 1997) that $\beta(q)$ of (1.11) is also given by the correlation integral

$$\beta(q) = \lim_{r \rightarrow 0} \frac{\log \int \mu(B(x, r))^{q-1} d\mu(x)}{-\log r}, \quad (1.53)$$

where $B(x, r)$ is the ball with centre x and radius r .

The correlation integral algorithm is a discrete analogue of this, convenient if the data consists of discrete data points with the density of the points representing the measure. Thus, a partition function is defined by

$$Z_r(q) = \frac{1}{N^q} \sum_i C_i(r)^{q-1},$$

with N the number of data points. In this case $C_i(r)$ is the number of points within distance r of the i th data point. As in the method of moments, a scaling $Z_r(q) \sim r^{-\beta(q)}$ is anticipated, so $\beta(q)$ can be estimated as the slope of the graph of $\log Z_r(q)$ against $\log r$ for a suitable range of r .

The methods above use a fixed box size. The next three algorithms use a fixed mass. That is, the measure is covered with boxes such that each box contains roughly the same mass. Here β is now the exponent in the partition function and q is the scaling parameter observed, which depends on β . All these algorithms are applicable to discrete data sets.

Density Reconstruction Method This algorithm is the inverse of the correlation integral method. Instead of counting the numbers of points in the ball with a fixed radius for each point, the number of points is fixed and the radius of the ball around each point that contains this number of points is estimated (Badii and Broggi, 1988).

Let N be the total number of data points. For $2/N \leq p \leq 1$ and $\beta \in \mathbb{R}$ we define the partition function

$$W(p, \beta) = \frac{1}{N} \sum_i R_i^{-\beta}(p),$$

where $R_i(p)$ is the radius of the smallest ball centered at the i -th point that contains Np points. Then $W(p, \beta) \sim p^{1-q}$, for small p gives a scaling exponent $q = q(\beta)$.

Nearest Neighbour Algorithm A variant of the density reconstruction method is the nearest neighbour algorithm (Badii and Politi, 1984). For a range of large N , select N points at random from a discrete data set representing the measure. We fix a positive number k and introduce the partition function

$$G_k(N, \beta) = \frac{1}{N} \sum_{i=1}^N \left[\delta_i^{(k)}(N) \right]^\beta,$$

where $\delta_i^{(k)}$ is the distance of the i -th point of the data set to its k -th nearest neighbour. A scaling of the form $G_k(N, \beta) \sim N^{q-1}$ for large N is anticipated and this can be used to estimate $q = q(\beta)$. Usually $k = 3$ or 4 is chosen since small scale random errors affect the estimation for smaller k .

Minimal Spanning Tree An algorithm has been developed based on a partition function involving the sum of β -th powers of the edge lengths of the minimal spanning tree of a discrete data approximation (Martinez et al., 1990). The calculation of a minimal spanning tree is a highly non-trivial task, making this algorithm very time consuming and difficult to use.

1.3.2 Performance of algorithms

Fixed box and fixed mass algorithms in general were described and compared by Mach et al. (1996). The fixed box algorithms gave a smaller error than the fixed mass algorithms when $q > 0$. The fixed mass algorithms gave a smaller error than the fixed box algorithm for $\beta > 0$, corresponding to $q < 0$. This is due to clipping errors, see below. The best algorithm might be a combination of both methods.

Borgani et al. (1993) compared the different algorithms described in section 1.3.1 on measures with different fractal and multifractal features and different sizes of approximating data sets. The authors found reasonable results with the method of moments and the correlation integral. Even with smaller sample size, these two algorithms gave reliable results for positive q . For negative q the results were less reliable due to clipping effects. The density reconstruction method gave better results for negative q but required a larger sample size. Nearest neighbour and minimal spanning tree methods delivered unreliable results in almost all tests. The standard box-counting and the correlation integral are

easy to implement and perform much faster than the other three. The density reconstruction, the nearest neighbour and the minimal spanning tree methods need time consuming sorting programs.

1.3.3 Techniques to improve box-counting

From the algorithms presented in section 1.3.1 the method of moments is most applicable to the type of data we obtain from rainfall radar and random cascade processes. It is almost as easy to implement as the histogram method. Although the method of moments requires Legendre transformation of β to give the multifractal spectrum it gives more reliable results than the histogram method. Therefore the method of moments is widely used for calculating multifractal properties of empirical data in many fields of physics, and it has been adopted for multifractal analysis in this thesis. We now discuss some refinements to the basic box-counting method.

Clipping

A fundamental difficulty with the box-counting algorithm is that of clipping errors. When $q < 0$, boxes containing only a small amount of measure contribute disproportionately to the partition function (1.51), see figure 1.4. In particular the limit in (1.52) is

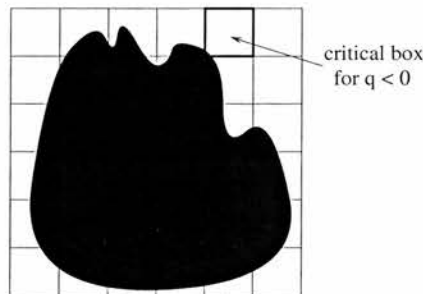


Figure 1.4: Boxes with low mass produce clipping problems for negative moments

unlikely to exist. Similarly, for $q < 0$ the partition function is unstable with respect to small movements in the grid of boxes, due to boxes containing small mass appearing unpredictably. In order to improve the box-counting method some modifications of the partition sum have been introduced to improve stability for $q < 0$.

Enlarged box-counting Riedi (1995) and Pastor-Satorras and Riedi (1996) attempt to improve the partition sum by expanding each r -mesh box

$$B = \prod_{k=1}^d [l_k r, (l_k + 1)r),$$

by a factor 3 about its centre and defining

$$B^* = \prod_{k=1}^d [(l_k - 1)r, (l_k + 2)r),$$

and hence defining a new partition sum \mathcal{M}_r^* based on these boxes,

$$\mathcal{M}_r^*(q) = \sum_{\mu(B) \neq 0} (\mu(B^*))^q.$$

By not including in the sum boxes with no measure in the centre, it is ensured that only boxes that have significant intersections with the measure are considered. Riedi (1995) show that the extended multifractal auxiliary function,

$$\beta^*(q) = \lim_{r \rightarrow 0} \frac{\log \mathcal{M}_r^*(q)}{-\log r},$$

performs better from a theoretical point of view, for example, on multinomial measures, measures on the Sierpiński Gasket and the Hénon attractor. The enlarged box-counting is suited for both discrete data and data defined on a grid and hence proves useful for analysing both spatial and temporal rainfall data.

Fuzzy box-counting The fuzzy box counting algorithm is another refinement involving overlapping displaced cubes. A set of displacements \mathbf{d}_j with $|\mathbf{d}_j| < 1/4$ and $j = 1, \dots, k$ is fixed. The measure is covered with r -meshes \mathcal{C}_r for a range of cube lengths r . The fuzzy box counting algorithm attempts to eliminate the clipping errors by defining a quantity $\hat{\mu}(B)$ based on the mass μ around the mesh cube B with $B \in \mathcal{C}_r$. Write $B + r\mathbf{d}_j$ for the cube obtained by translating B by the vector $r\mathbf{d}_j$. The geometric mean over all displaced cubes

$$\hat{\mu}(B) = \left[\prod_{j=1}^k \mu(B + r\mathbf{d}_j) \right]^{1/k}$$

replaces the measure $\mu(B)$ in calculating the partition function:

$$\hat{\mathcal{M}}_r(q) = \sum \hat{\mu}(B)^q.$$

Using $\hat{\mathcal{M}}_r$ rather than \mathcal{M}_r reduces clipping errors, because if one of the displaced boxes contains no measure, then $\hat{\mu}(B) = 0$. The fuzzy box-counting algorithm is only suitable for discrete data and not generally for data supported by a grid. Therefore this method is less useful for hydrological applications than enlarged box-counting.

Use of balls Caswell and Yorke (1986) demonstrate that the use of partition sums involving balls rather than cubes reduces the clipping error. A mesh of balls may be used in any of the above methods, including in a *fuzzy ball* counting algorithm (Alber, 1998).

Results These improvements of the box-counting algorithm reduce the clipping problem for negative q at least in theory. For positive q the standard method gives more accurate results. However, for enlarged or fuzzy box counting finer data sets are required to obtain estimates to a given degree of accuracy, and this effect increases in larger spatial dimensions. A compound approach – standard for $q > 0$ and enlarged box or fuzzy box counting for $q < 0$ – would be an improvement on using the standard algorithm for all q .

The error of the multifractal functions may be calculated by applying the rule of error propagation to the error of the regression on the moments, while computing $\beta(q)$. The error bars in the $\beta(q)$ plot itself would have been too small to get any information out of them.

The cut-off effect of empirical data

Empirical data, such as temporal rainfall data collected from tipping bucket rain-gauges, may have a cut-off in that there is a minimum threshold below which a zero reading is

recorded in any interval in the data set. Even if this threshold is small, its effect can swamp the actual data in the computation of $\beta(q)$ for $q < 0$. From the definitions (1.10)-(1.11), it is the regions of low measure density that contribute significantly to $\beta(q)$ when $q < 0$. If the data has a cut-off, then such low density regions are eliminated.

Theoretical sources of errors

We summarise the possible sources of errors in algorithms that we have identified above from theoretical considerations.

- The data set must be large if regression analysis is to be done over a wide enough range of scales. The inadequacy of small data sets is particularly significant when $|q|$ is large. Since the crucial factor is the range of scales that can be considered, the size of data sets required increases rapidly with the dimension d of the overall space \mathbb{R}^d .
- Clipping will lead to difficulty in determining the partition sums and their behaviour for $q < 0$. A method such as enlarged box-counting would be expected to be superior in this case.
- For data sets with a recording threshold, the cut-off effect may swamp calculations for $q < 0$.

These effects are observed in some of the computational examples that follow.

1.3.4 Preliminary results of the algorithms on fractal measures and rainfall data

In order to verify and compare the performance of the algorithms just described, we apply them to a variety of measures for which the multifractal spectrum may be found analytically and also to some empirical rainfall data. The algorithms best suited for the analysis of data distributed on a grid, as for example rainfall data, are the standard and the enlarged box-counting algorithms. Whilst the auxiliary function $\beta(q)$ is the primary function computed, and therefore more appropriate for direct comparison, the multifractal spectrum $f(\alpha)$, obtained from $\beta(q)$ by Legendre transform, permits easier visual comparison. In the following examples error-bars are only applied to the results of standard box-counting for positive q and to those of enlarged box-counting for negative q .

The binomial measure on the Cantor set

We compute the multifractal functions of a binomial measure on the middle third Cantor set in the unit interval given by the IFS (1.28) and weights

$$\boxed{w_1 = 1/3 \quad w_2 = 2/3}$$

and compare them to the analytically calculated functions, (1.27) and (1.29).

The measure is computed by the chaos game, on the unit interval subdivided into 2^{19} intervals.

One of the features of this test is that the measure is generated on ternary subintervals, whilst the box-counting is done on binary intervals, so that clipping is likely. This affects both box-counting methods.

From the graphs we observe overall a good agreement between the computed and the calculated functions (1.27) and (1.29). For positive values of q the standard box-counting

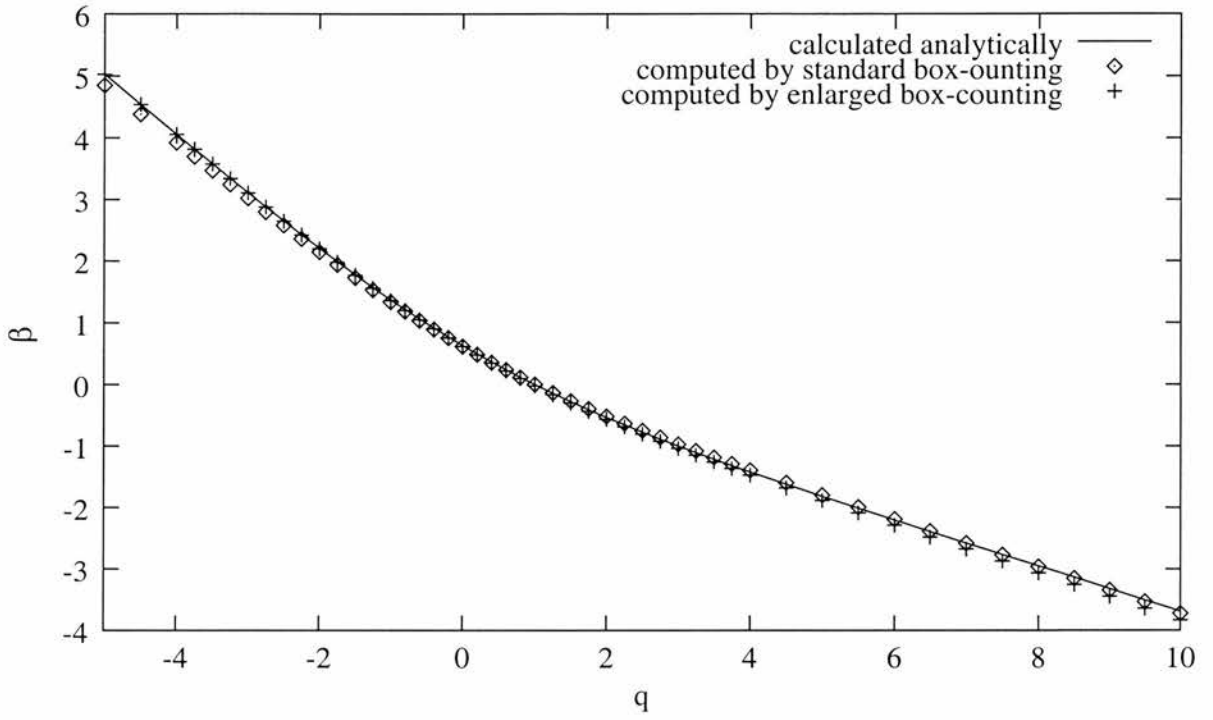


Figure 1.5: $\beta(q)$ of the binomial measure on the middle third Cantor set

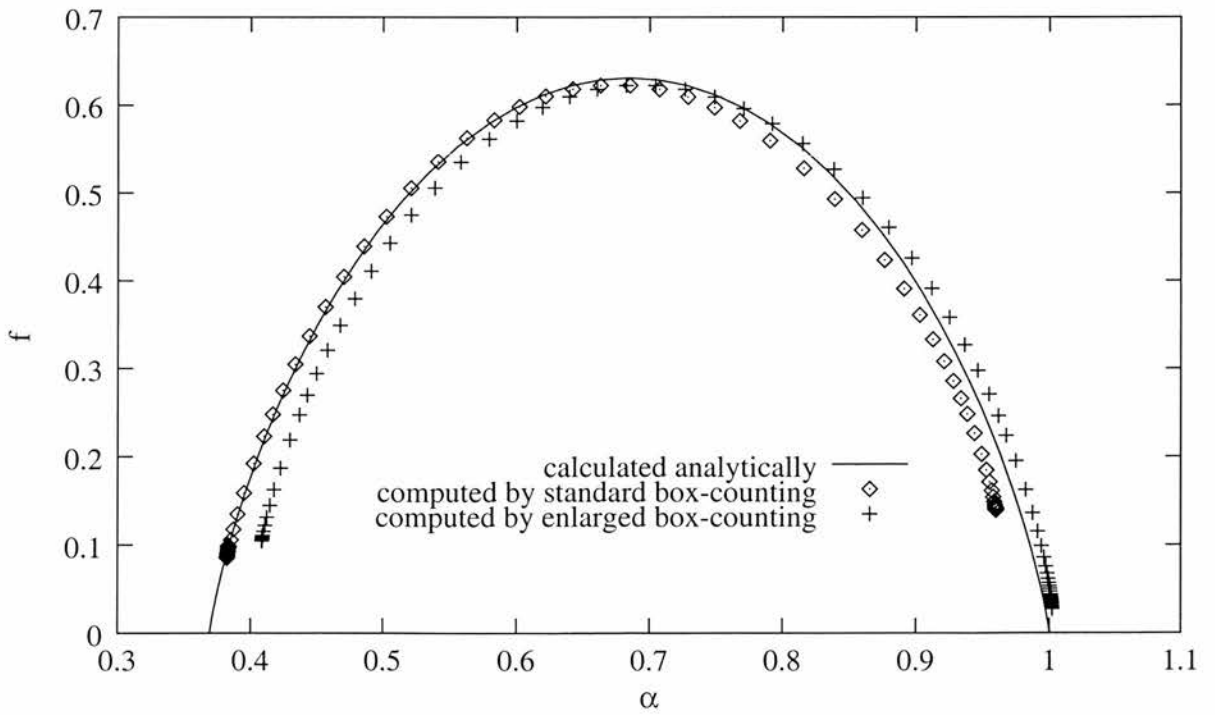


Figure 1.6: $f(\alpha)$ of the binomial measure on the middle third Cantor set

algorithm results in better agreement than the enlarged box-counting, probably because latter effectively runs on a wider grid. For negative values of q the enlarged box-counting algorithm gives better results. The high irregularity of the measure results in clipping errors for negative q , which is coped with better by the enlarged box-counting algorithm, as expected. For large values of $|q|$ the results of both algorithms diverge more from the calculated results than for small $|q|$.

The random cascade measure

In this example we compute the multifractal functions of a measure generated by a random cascade process with discrete weights as described in section 1.2.4. We take the IFS (1.31) on \mathbb{R}^2 , with subdivision number $N = 2$. The weights are chosen as independent random variables with identical distribution for each square of each subdivision with W_1, W_2, W_3, W_4 each independently taking values a_i with probabilities p_i , see (1.44):

$p_0 = 0.136$	$p_1 = 0.200$	$p_2 = 0.300$	$p_3 = 0.364$
$a_0 = 0.000$	$a_1 = 0.170$	$a_2 = 0.380$	$a_3 = 0.280$

The almost sure multifractal spectrum resulting from the random cascade is given by (1.49) and (1.50).

We generate the measure by computing 12 iterations of the random cascade process resulting in a data set of 4096×4096 points. One might expect this to be a reasonable approximation to the 12th iteration of a realisation of that random cascade process. The multifractal functions are computed using the standard box-counting and the enlarged box-counting algorithms. The results are shown in figures 1.7 and 1.8.

We observe a good agreement for small $|q|$ for both algorithms. Because of the binary character of both the construction of the random cascade and the two box-counting methods, the clipping effect would be rather small in this example.

The self-similar measure on the Sierpiński triangle

In this example we compute the multifractal functions of a self-similar measure on the Sierpiński triangle given by the IFS (1.25), and compare it to the analytically calculated functions, see (1.30). The weights used are

$w_1 = 0.2$	$w_2 = 0.3$	$w_3 = 0.5$
-------------	-------------	-------------

The multifractal measure is calculated by using the chaos game, see section 1.1.3. We calculate 1000000 points on a 4096×4096 grid and use the standard box-counting and the enlarged box-counting algorithms to compute the multifractal functions, see figures 1.9 and 1.10.

Again, for positive q the standard box-counting algorithm performs better than the enlarged box-counting. For very small negative values of q both algorithms seem to perform equally well and for larger valued negative q the enlarged box-counting seems to be superior, presumably because the clipping effect is reduced.

The self-affine measure on the generalised Sierpiński triangle

We now compute the multifractal functions of a self-affine measure on the generalised Sierpiński triangle. The measure is generated by a weighted iterated function system as

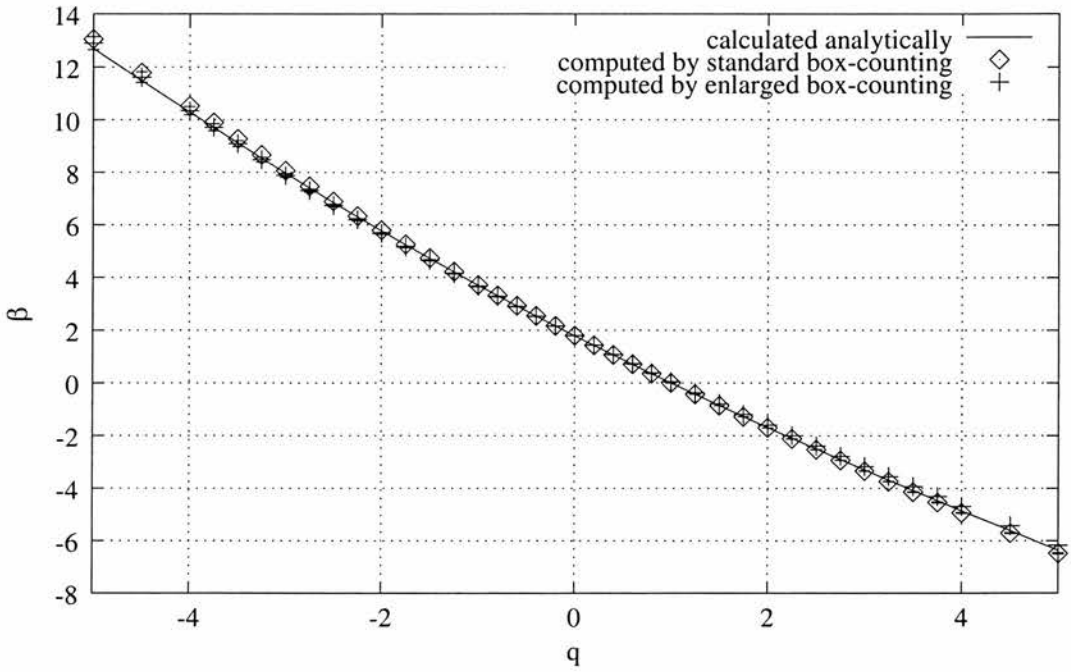


Figure 1.7: $\beta(q)$ of the random cascade measure with error bars indicating 95% certainty in regression

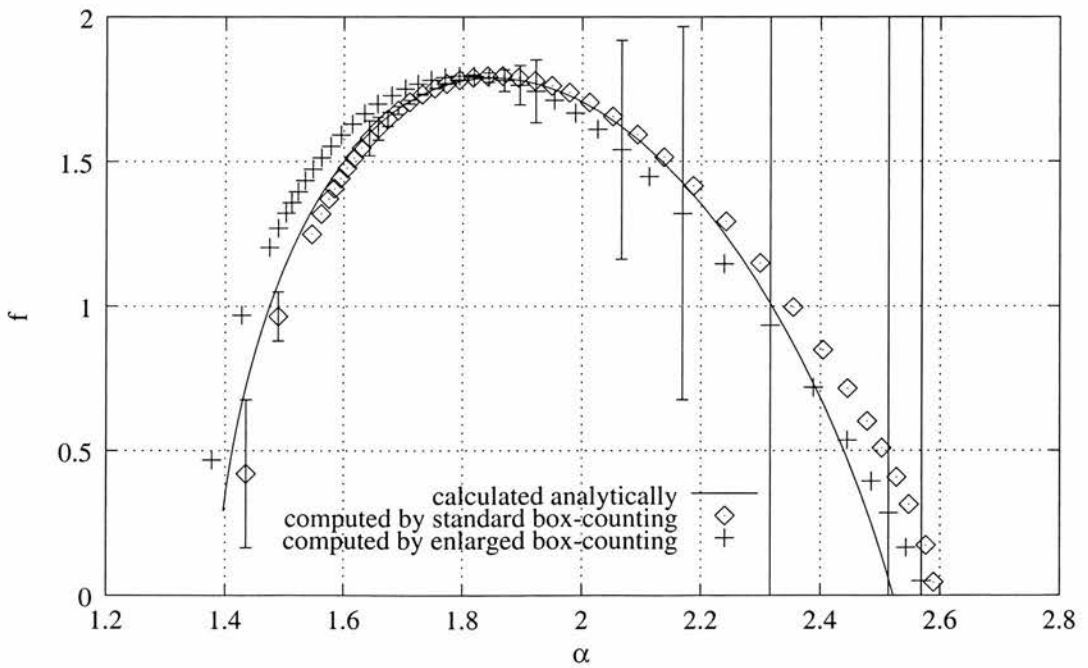


Figure 1.8: $f(\alpha)$ of the random cascade measure with error bars indicating 95% certainty in regression

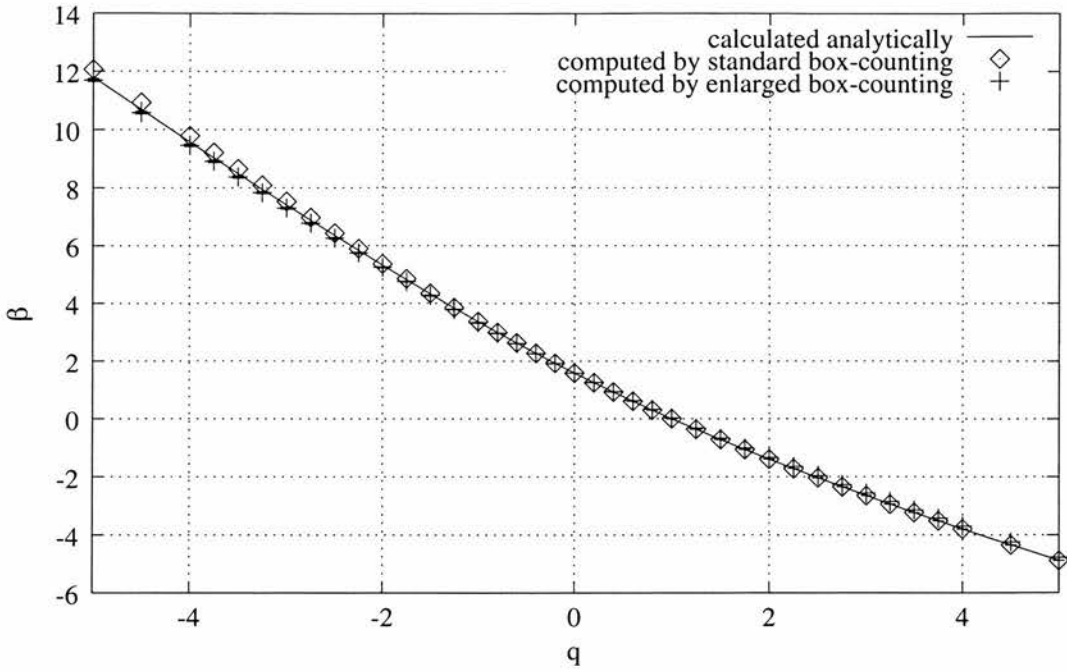


Figure 1.9: $\beta(q)$ of the self-similar measure on the Sierpiński triangle with error bars indicating 95% certainty in regression

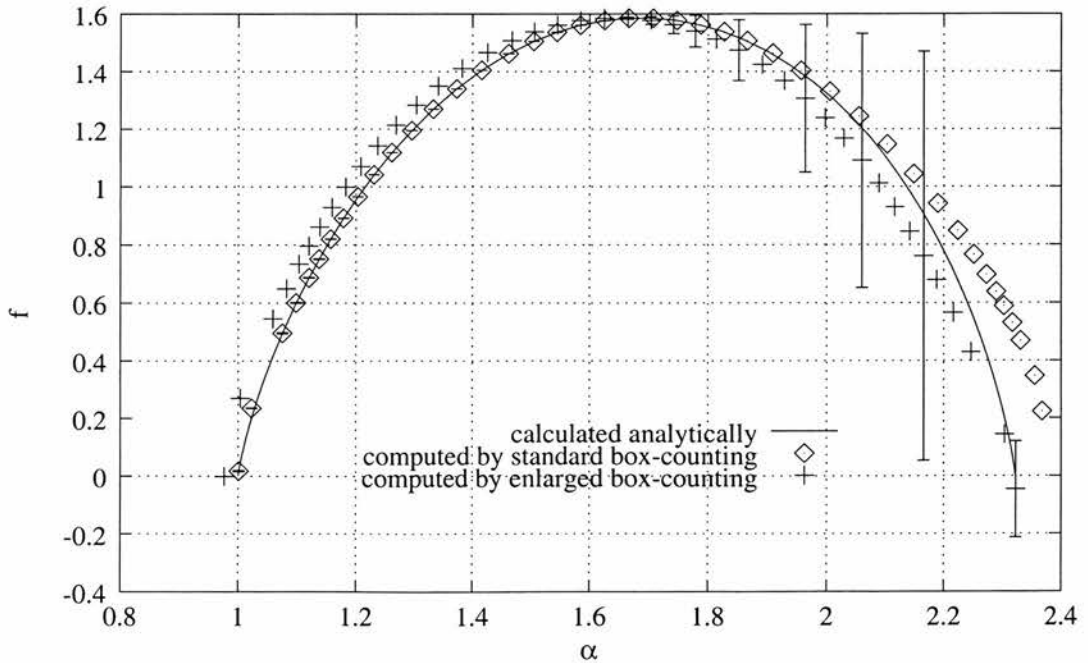


Figure 1.10: $f(\alpha)$ of the self-similar measure on the Sierpiński triangle with error bars indicating 95% certainty in regression

in (1.26), using the contractions $S_1, S_2, S_3 : \mathbb{R}^2 \rightarrow \mathbb{R}^2$

$$\begin{aligned} S_1 \begin{bmatrix} x_1 \\ x_2 \end{bmatrix} &= \begin{bmatrix} 0.25 & 0 \\ 0 & 0.25 \end{bmatrix} \begin{bmatrix} x_1 \\ x_2 \end{bmatrix} + \begin{bmatrix} 0 \\ 0.75 \end{bmatrix} \\ S_2 \begin{bmatrix} x_1 \\ x_2 \end{bmatrix} &= \begin{bmatrix} 0.4 & 0 \\ 0 & 0.75 \end{bmatrix} \begin{bmatrix} x_1 \\ x_2 \end{bmatrix} + \begin{bmatrix} 0 \\ 0 \end{bmatrix} \\ S_3 \begin{bmatrix} x_1 \\ x_2 \end{bmatrix} &= \begin{bmatrix} 0.6 & -0.15 \\ 0 & 0.75 \end{bmatrix} \begin{bmatrix} x_1 \\ x_2 \end{bmatrix} + \begin{bmatrix} 0.4 \\ 0 \end{bmatrix}, \end{aligned} \tag{1.54}$$

so S_1 is a similarity and S_2, S_3 are affine maps. The attractor of this IFS is shown in figure 1.11. The weights are chosen as

$w_1 = 0.2$	$w_2 = 0.3$	$w_3 = 0.5$
-------------	-------------	-------------

The fractal and multifractal properties of this example are discussed in chapter 2, where in particular $\beta(q)$ is calculated.

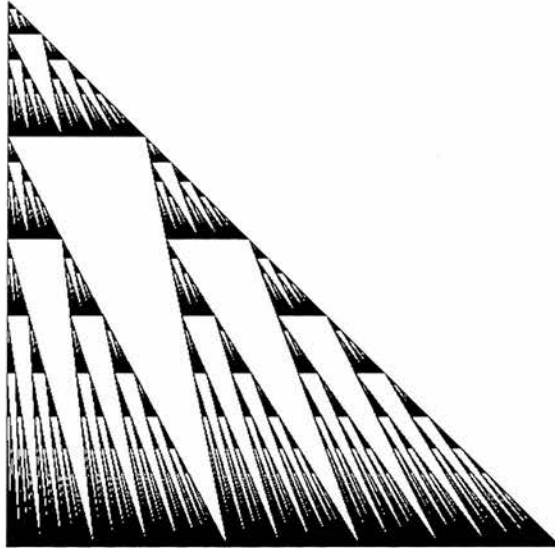


Figure 1.11: Generalised Sierpiński triangle

As before, the multifractal measure is realised using the chaos game, by calculating 1000000 points on a 4096×4096 grid. This example is non-isotropic and non-homogeneous and is of particular interest, given the applications we have in mind.

The results of the standard box-counting and the enlarged box-counting algorithms on this measure are shown in figures 1.12 and 1.13. The analytical results are only calculated for $q > 0$, see theorem 2.3. Nevertheless, it is reasonable to assume that (2.15) also holds for $q < 0$. Therefore we draw the analytic multifractal function for $q < 0$ with a dashed line.

For positive q the standard box-counting results in good agreement with the analytical functions, but for negative q it results in greater error, due to clipping. The $\beta(q)$ function, computed by standard box-counting is non-convex making the Legendre transform inappropriate. The enlarged box-counting gives more realistic results for negative q , avoiding clipping errors, but the agreement of the computed and the analytical $f(\alpha)$ is far from good.

In figure 1.13 error bars are included. From them we observe that the values of $f(\alpha)$ are more reliable in the case of standard box-counting for $q > 0$ and for enlarged box-counting for $q < 0$.

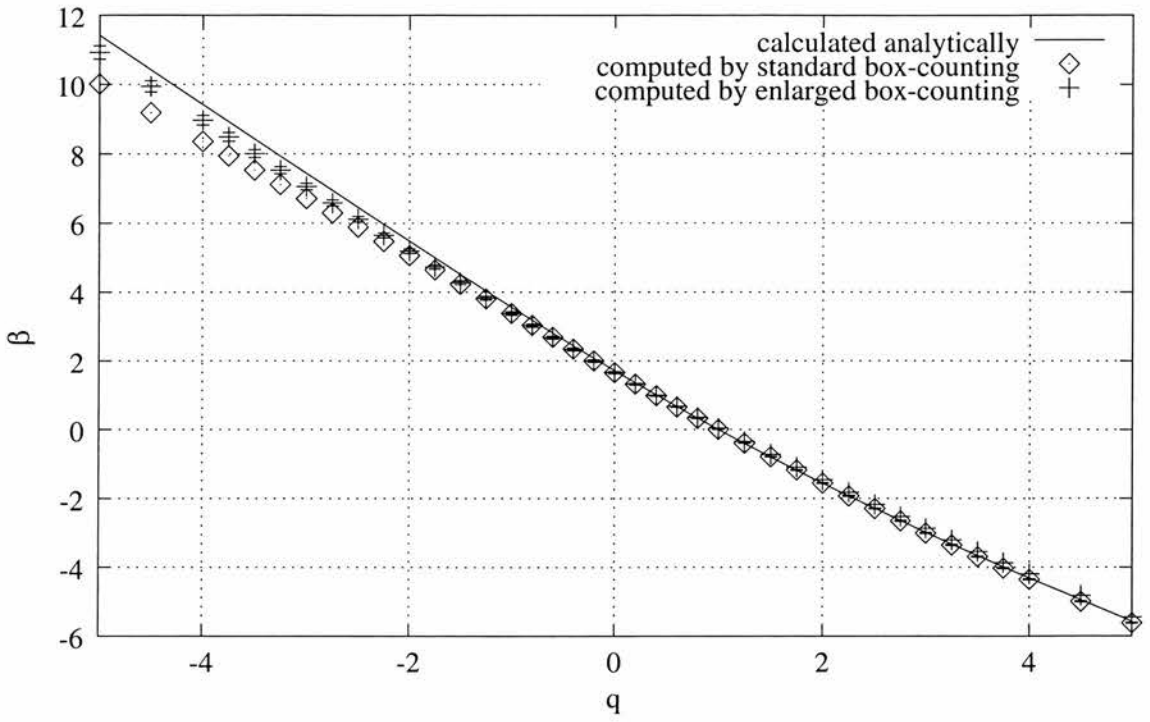


Figure 1.12: $\beta(q)$ of the self-affine measure on the generalised Sierpiński triangle with error bars indicating 95% certainty in regression

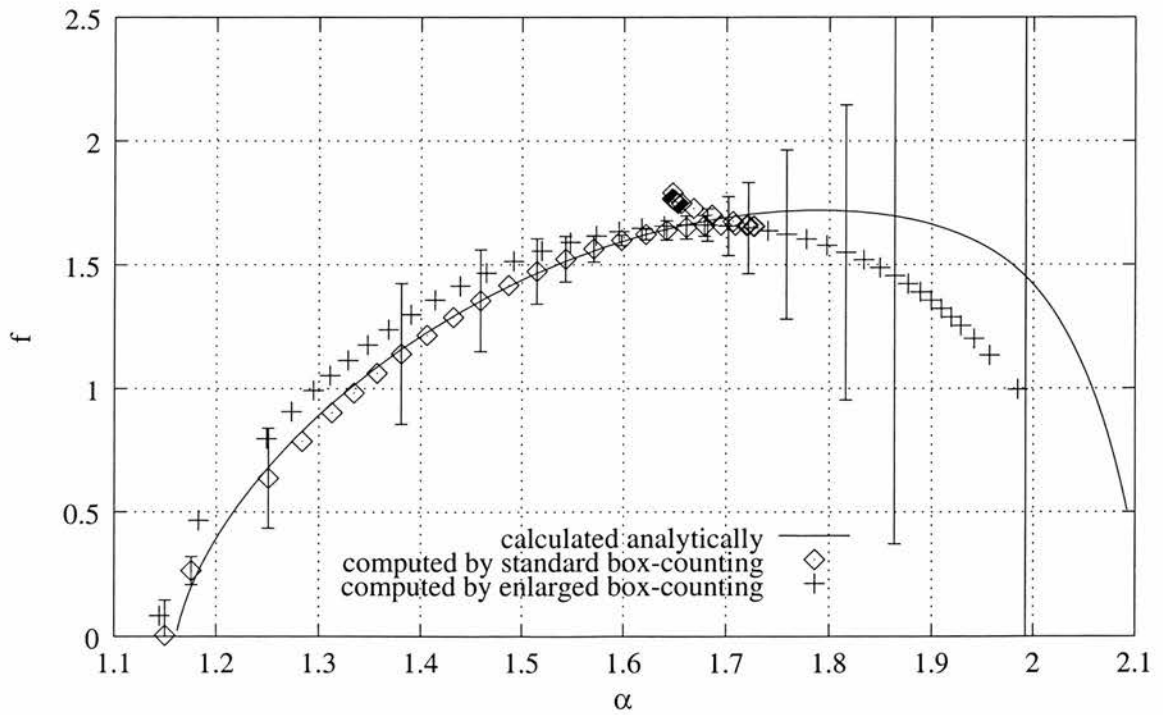


Figure 1.13: $f(\alpha)$ of the self-affine measure on the generalised Sierpiński triangle with error bars indicating 95% certainty in regression

Temporal rainfall data

We now apply the standard and the box-counting algorithms to temporal rainfall data, a time series taken at 30min intervals at Rosemount, MN, USA, from 01/10/1996 to 19/03/1997, consisting of 8192 data points. The results of the analysis are displayed in figures 1.14 and 1.15.

This data, which was collected from a tipping bucket rain gauge, has a cut-off with the smallest amount of rainfall that can be recorded being the volume of the tipping bucket. If the tipping bucket is not filled in one time step, the rainfall collected is not recorded, but carried over to the next time step. This leads to small rainfall volumes being neglected and a fixed minimum intensity across the support of the data leading to a false multifractal spectrum for $q < 0$, see section 1.3.3.

From the graphs we observe a reasonable agreement between the two algorithms for $q > 0$. From this and the fact that the multifractal spectrum stretches over a considerably large region of α we can conclude that the temporal rainfall data has multifractal character. For negative q the standard box-counting results in a non-convex multifractal auxiliary function. Reasons for this might be clipping effects, or the cut-off effect for quantised data. The enlarged box-counting algorithm compensates for the clipping effect, but there is a visible cut-off for negative q , with the points in the $f(\alpha)$ plot accumulating in one point.

Spatial rainfall data

As a final example we discuss the results of the box-counting algorithms applied to spatial rainfall data. The data used is a composite image from the NEXRAD WSR-88D radars covering the majority of the USA. We analyse a square area of sidelength 2048km on a grid of 512×512 boxes, see figure 1.16. The centre of the area covered is at 40.46°N , 91.86°W .



Figure 1.16: Spatial rainfall data taken on 22/12/1997 at 09:00, 11:00 and 13:00

The results of the standard and the enlarged box-counting algorithms on one spatial data set taken on 22/12/1997 at 11:00 are shown in figures 1.17 and 1.18.

The results of the two algorithms do not coincide, except for a small range of $0 < q < 2$. The much coarser data set than in the previous examples is likely to lead to large errors here, and this affects the enlarged box-counting algorithm even more. For negative q the standard box-counting algorithm leads to large errors with the multifractal auxiliary function being non-convex. We observe that the part of the multifractal function with $q < 0$ computed by the enlarged box-counting does not coincide well with the part of the multifractal function with $q > 0$ computed by the standard box-counting algorithm. Again, this is because of the small data set and large regression errors.

Figures 1.19 and 1.20 show the results of the multifractal analysis of the three consecutive radar images shown in figure 1.16. For $q < 0$ enlarged and for $q > 0$ standard

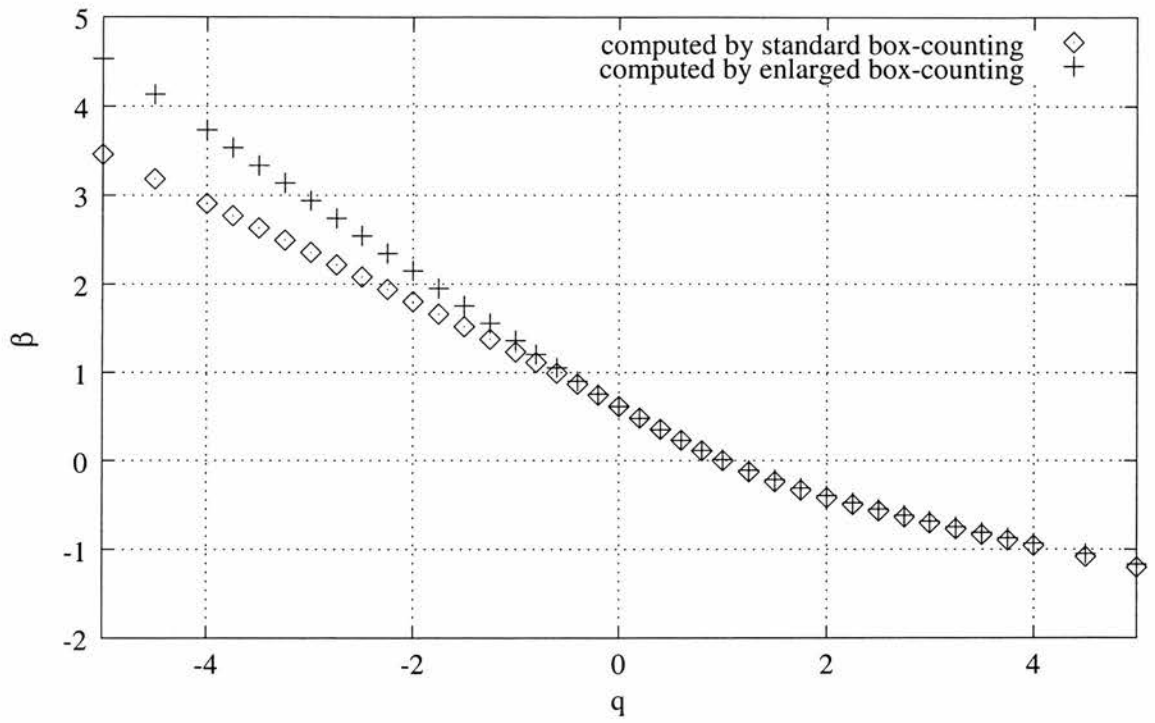


Figure 1.14: $\beta(q)$ of the Rosemount temporal rainfall data

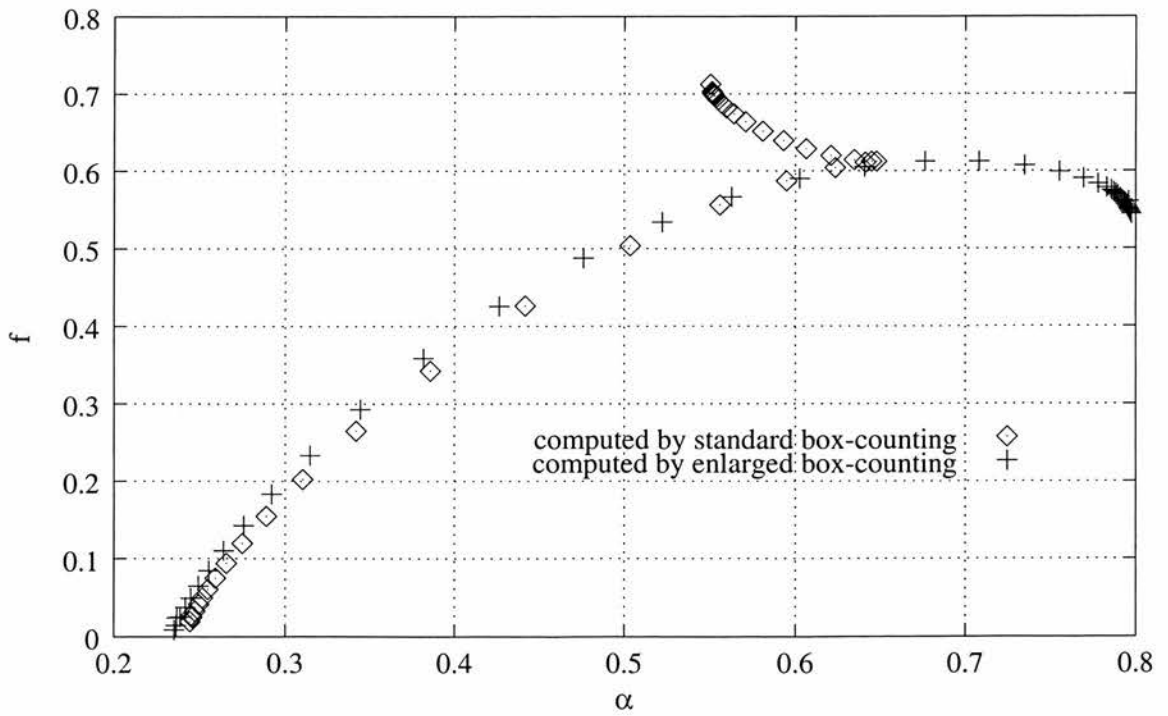


Figure 1.15: $f(\alpha)$ of the Rosemount temporal rainfall data

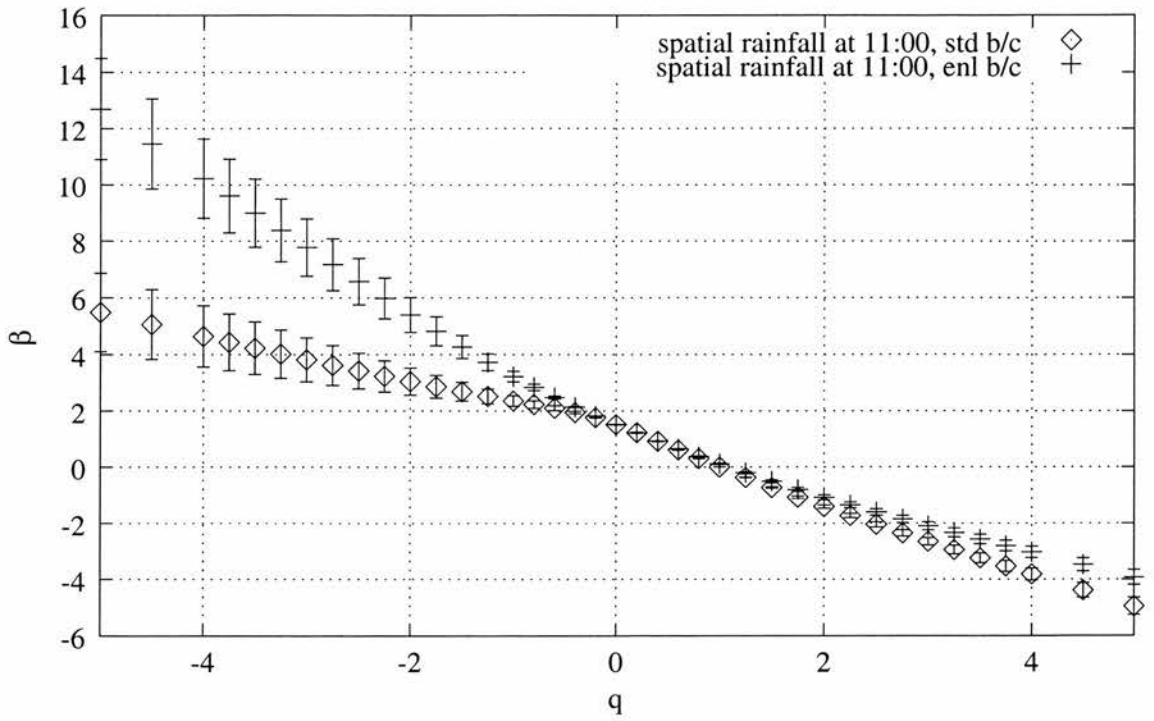


Figure 1.17: $\beta(q)$ of spatial rainfall data taken on 22/12/1997 at 11:00 with error bars indicating 95% certainty in regression

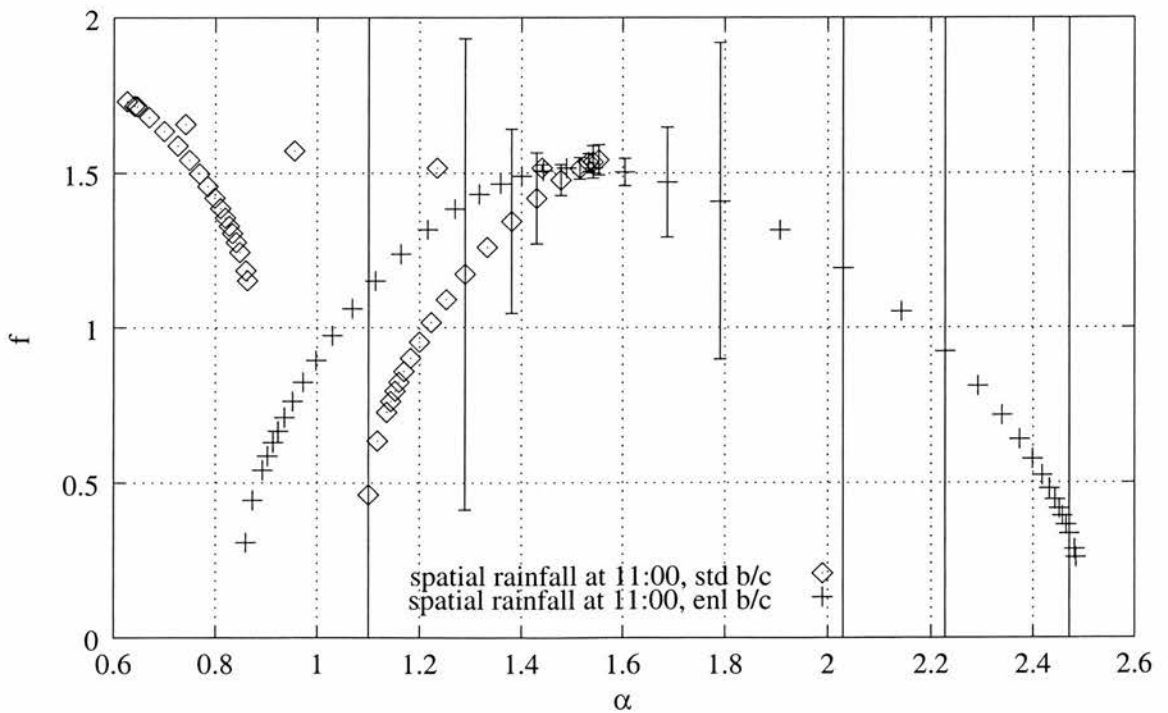


Figure 1.18: $f(\alpha)$ of spatial rainfall data taken on 22/12/1997 at 11:00 with error bars indicating 95% certainty in regression

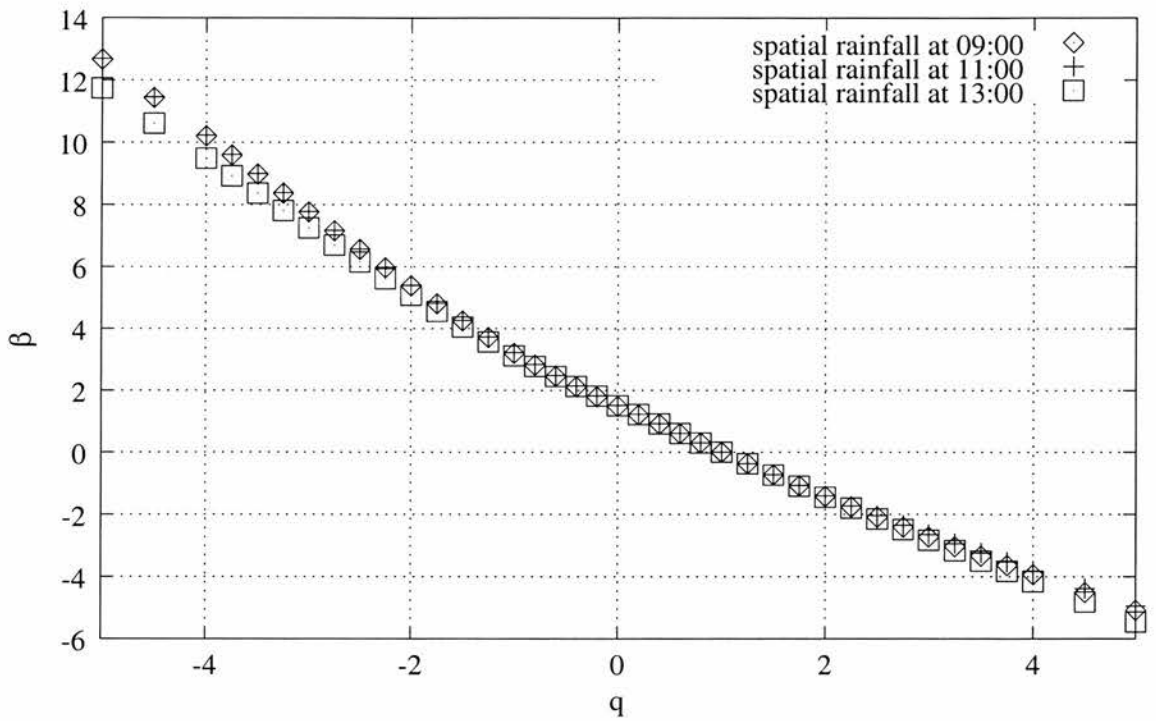


Figure 1.19: $\beta(q)$ of spatial rainfall data taken on 22/12/1997 at three different times, analysed with standard box-counting for $q > 0$ and enlarged box-counting for $q < 0$

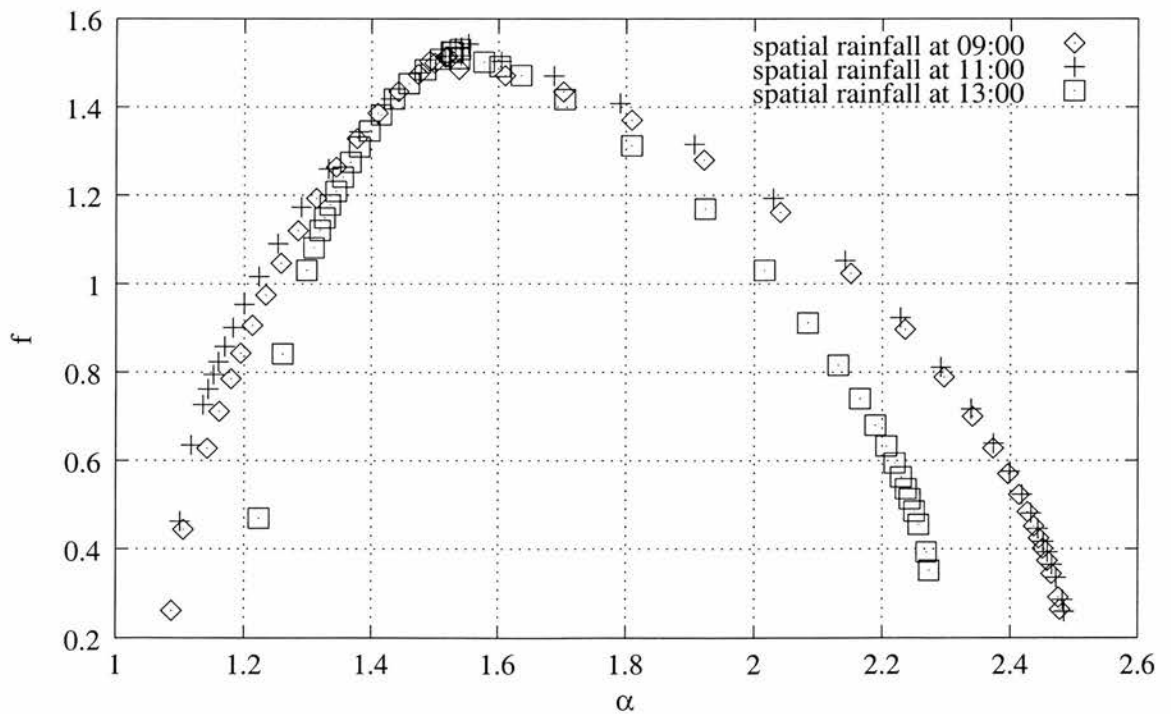


Figure 1.20: $f(\alpha)$ of spatial rainfall data taken on 22/12/1997 at three different times, analysed with standard box-counting for $q > 0$ and enlarged box-counting for $q < 0$

box-counting are applied. Although the radar images differ notably from each other, the multifractal functions are quite similar, especially for small $|q|$. This leads to the assumption that not only the multifractal properties of the rainfall are relatively stable over time, but also shows that the combination of the two algorithms gives reproducible results.

Conclusion

The experiments conducted on theoretical and “real life” data confirm the expectations for the standard and enlarged box-counting algorithms. The strategy of using standard box-counting for $q \geq 0$ and enlarged box-counting for $q < 0$ seems to be adequate for use with empirical data such as temporal and spatial rainfall data. Nevertheless, care is required to interpret computations using small data sets, especially for large $|q|$, and also for $q < 0$ where clipping and the cut-off effect may be present. However, for $q < 0$ the multifractal functions describe properties of regions of very sparse density. This information has little significance in rainfall analysis and is neglected in almost all of the literature on multifractal analysis of rainfall.

1.4 Hydrological background

This section discusses the motivation for using fractals, multifractals and, in particular, cascade processes in rainfall modelling, as well as the hydrological setting to which cascades are applied.

1.4.1 Theoretical basis for fractal and multifractal rainfall analysis

Atmospheric turbulence is a major factor in cloud formation, and therefore one might expect features that are observed in turbulence to be reflected in rainfall patterns. Turbulence remains far from understood, and the goal of explaining turbulent phenomena starting from the Navier-Stokes equations is still elusive. Nevertheless, cascade and fractal models for turbulence have attracted interest for many years in that they provide a good explanation of certain observed features.

The idea of scaling in turbulence, and that of regions being affected by neighbouring regions of comparable size, go back at least to Richardson (1926). It was Kolmogorov (1941) who expressed this notion in the form of what we now refer to as cascades. His idea was that kinetic energy is introduced into a system at a large scale, for instance by movement of the atmosphere at a global scale. But energy can only be dissipated as heat on a very small scale where the effects of viscosity are important. Thus, he postulated that energy is transferred from large scale to small by a sequence of circulating eddies of decreasing size until it reaches the small scale eddies at which dissipation occurs. The *eddies within eddies* form a type of cascade.

Kolmogorov assumed that the fluid region is filled by eddies at all scales, which would mean that heat is dissipated uniformly across the region. Such *homogeneous turbulence* is not supported by experiment, however, which shows that the dissipation rate varies greatly across the fluid – a phenomenon known as *intermittency*.

Mandelbrot (1974) proposed an inhomogeneous model where the cascade is *fractal* and the eddies do not fill the entire space occupied by the parent eddies, as in the construction of certain self-similar fractals (fig 1.21). In this case the heat dissipation is concentrated on the fractal, and a simple calculation, see Falconer (1990, chapter 18.3), shows that a fractal dimension of about 2.5 is consistent with experimental results for many three-dimensional fluids.

A variant of this leads to a multifractal model for turbulence, see Mandelbrot (1974). There is no reason why at each stage of the cascade of eddies that the energy should be distributed equally amongst the sub-eddies. If an unequal distribution is typical, then it leads to a multifractal cascade measure or random cascade measure. Again, this produces intermittency, and also different moment scaling with different exponents. Intermittency occurs even if the support of the cascade is space filling, but for dissipation to be concentrated on a fractal subset of the region, we require the measure transferred to some component of the cascade to be 0, that is $w_i = 0$ for some i in (1.26).

Schertzer and Lovejoy (1983, 1987) point out that the energy scaling that results from cascade models is consistent with the incompressible Navier-Stokes equations.

They suggest that rainfall variability might be modelled as a turbulent cascade process, with the multifractal effects of atmospheric turbulence reflected in multifractality of the rainfall field. This idea has been the basis for much subsequent work on rainfall modelling.

1.4.2 Experimental evidence for fractals and multifractals in rainfall

In this section we review some papers which give experimental evidence for the multifractality in rainfall fields, or which discuss this subject critically. For a more comprehensive review see Olsson (1996a).

Mono-fractals in hydrology

Hurst et al. (1965) researched the long-term storage of reservoirs, in particular the Nile. In his work he developed a statistical method, the *rescaled range analysis* (*R/S*-analysis). Let t be a discrete integer-valued time and ξ be the observed variable. Then $X(t, \tau)$, the *accumulated departure* of ξ from its mean $\langle \xi \rangle_\tau$ over time period τ , is defined for $1 \leq t \leq \tau$ as

$$X(t, \tau) = \sum_{u=1}^t \{\xi(u) - \langle \xi \rangle_\tau\} = \sum_{u=1}^t \xi(u) - t\langle \xi \rangle_\tau.$$

Let $R(\tau)$ be the *range* of X over the interval 0 to τ , that is

$$R(\tau) = \max_{1 \leq t \leq \tau} X(t, \tau) - \min_{1 \leq t \leq \tau} X(t, \tau).$$

Hurst defined the *rescaled range* as the range divided by its standard deviation S . He found that this rescaled range can be very well described by the relationship

$$R/S = (\tau/2)^H,$$

as $\tau \rightarrow \infty$, where H is known as the *Hurst exponent*.

This inspired many mathematicians and hydrologists in their work on scaling in hydrology. Mandelbrot and Wallis (1968) and Mandelbrot and Wallis (1969) described how

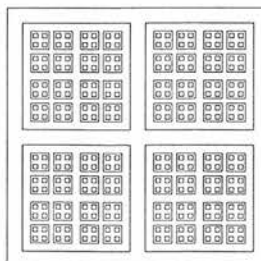


Figure 1.21: Example for a cascade that is not space filling.

the concept of self-similarity might be used to study a variety of natural phenomena, in particular precipitation. The aim of Mandelbrot's and Wallis's studies was to explain and then simulate two properties of rainfall that were not well explained by the contemporary theory and that could not be found in rainfall simulated using classical rainfall distributions: The *Noah-effect*, the fact that extreme events can be very extreme indeed, and the *Joseph-effect*, the fact that long periods of high or low precipitation can be very long indeed. Classical rainfall simulations typically used independent Gaussian distributions and yield in Hurst exponents of 0.5, whereas the observed value was at 0.7 – 0.85.

More recently Lovejoy (1981) and Lovejoy and Mandelbrot (1985) analysed the scaling, in particular they observed that, writing $P(t)$ for the rainfall rate at time t , the statistical distribution of $P(\lambda t)$ is very similar to that of $\lambda^H P(t)$, where H is a non-integer scaling exponent; typically $H \approx 0.7$. They also analysed spatial rainfall and cloud data obtained by satellite over the Indian Ocean. Lovejoy (1982) found scaling in the region between 1 km² and 1.2×10^6 km². Zawadzki (1987) analysed data from a 10-year record of data from a tipping-bucket rain gauge. Using the same analysis method as Lovejoy and Mandelbrot (1985), he could not find scaling in his data. He concludes, that noise and, particularly, poor sampling can affect the results one gets from such analysis. Kumar and Foufoula-Georgiou (1993a,b) developed a method for analysing the fractal dimension of small-scale and large-scale fluctuations of rainfall data by segregating it using wavelet transformations. In their analysis of radar data they found scaling in the small-scale but not in the large-scale fluctuations. Dwyer and Reed (1994) calculated the fractal dimension of rainfall, wind speed and air temperature data. They analysed hourly data over two years in order to predict correction factors for assessing the likelihood of extreme events. Motivated by the discrepancy between the resolution of general circulation models, see section 1.4.3 below, and the typical length scale of rainfall, Onof and Wheeler (1996) analysed spatial rainfall from areas of different types. They compared the fractal dimension of the spatial rainfall data to the coverage of the rainfall fields. They conclude their fractal analysis by remarking that the *variability of the fractal dimension primarily suggests the need for examining the rainfall field as a multifractal*.

Multifractals in hydrology

The empirical basis for departures from simple scaling in rainfall data has been examined independently by Schertzer and Lovejoy (1987) and Gupta and Waymire (1990). Both examined spatial rainfall data, and in addition Gupta and Waymire (1990) examined river flow data. They proposed that rainfall is multifractal, and can be represented by cascade processes. Lovejoy and Schertzer (1990b) used the multifractal techniques to aid the correction of rainfall radar data.

Gupta and Waymire (1993) further investigated the relationship between rainfall data and cascades, in particular they tested estimation methods for cascade parameters. Over and Gupta (1994) analysed the multi-scaling of temporal and spatial rainfall data and compared the outcome with that of random cascade simulations. They suggested that cascades might be used in a rainfall disaggregation in GCMs or in flood forecasting. Pinzón et al. (1995) estimated the multifractal spectrum of water vapour in the lower atmosphere.

Onof et al. (1996) analysed a series of rainfall radar images. They observed a break in the scaling of temporal rainfall data at 30 – 40 minutes, at which Taylor's frozen field hypothesis ceases to work as well. This hypothesis postulates the equivalence of the spatial autocorrelation at a fixed point in time and the temporal autocorrelation at a fixed position in space (Taylor, 1938). The only break in the scaling of spatial rainfall they observed was at scales larger than 50 km, due to sampling effects. The autocorrelation structure of both measured and modelled data were found to be similar. Olsson (1996a) analysed

spatial and temporal rainfall data obtained from a network of tipping-bucket gauges. He also modelled temporal rainfall with a random cascade and compared the multi-scaling of both, simulated and real rainfall data (Olsson, 1996b). Lovejoy and Schertzer (1995) and Schertzer and Lovejoy (1996) gave comprehensive summaries of their theories and methods about multifractal analysis of rainfall and simulation using cascades.

Marsan et al. (1996) proposed a method for introducing temporal development into random cascade models for simulating and forecasting rainfields. Veneziano et al. (1996) analysed short time rainfall data for several intense storms and rejected several simple-scaling and multi-scaling models. Instead they proposed their own non-fractal and non-multifractal stochastic model. Over and Gupta (1996) modelled spatial rainfall fields by using random cascades and also presented an extension to space-time.

Note that although in principle they stand for the same mathematical properties, the terms fractality/multifractality and scaling/multi-scaling respectively are usually used in the hydrological literature to express two different methods: the former terms imply dimension or dimension spectrum calculation by using box-counting, as in section 1.3.1, whereas the latter imply a calculation involving probabilities and statistical moments.

One should keep in mind that fractal analysis of real world data is extremely delicate, and convincing conclusions about multifractals requires large data sets. Some of the results presented in the literature are unconvincing and in particular give little information about the confidence limits from the regression.

1.4.3 Rainfall representation in circulation models

Chapter 3 presents a new application of cascades to hydrology, in the field of climate models, with the aim of providing a better rainfall representation for the land-surface-atmosphere interaction component of such models. The changes in the water balance are tested by observing canopy evaporation and canopy throughfall.

By referring to *general circulation of the atmosphere* climatologists usually think of the large scale air flow of the whole globe. The general circulation of the atmosphere is responsible, for example, for the winds and therefore horizontal movements of clouds. But it also causes redistribution of energy and moisture and is responsible for modifications of their latitudinal imbalances. General circulation is sometimes divided into two components: *primary circulation features*, that is persistent large-scale features, and the *secondary circulation features*, that is short-lived cyclones and anti-cyclones, which are responsible for weather changes over large portions of the Earth. A *General Circulation Model* (GCM) models the three dimensional general circulation of the Earth's atmosphere, and sometimes of the oceans. For this the Earth is covered by a grid on which conservation equations for momentum, mass and energy are solved. Hydrologists have long understood the physics of surface hydrological processes. They are able to model these processes very accurately provided that many climatological and geological parameters are known. Typically such understanding is focused at the catchment scale at the order of a few meters. As mentioned, climate simulations, such as GCMs, usually run on resolutions with typical length scales much greater than those of surface hydrological processes. Thomas and Henderson-Sellers (1991) performed a comparison of time and length scales of several climatic phenomena. They concluded that in order to take surface hydrological processes into account in GCMs, a method of incorporating subgrid processes must be developed. They argued that the variable of greatest importance is the fraction of the GCM grid cell on which precipitation occurs, because the hydrological effects resulting from non-uniform rainfall distribution across such a cell are important.

Chapter 3 concerns that component of the GCM which involves the hydrological interaction between soil, surface, vegetation, and the atmosphere. This component simulates

the water stores in several layers of the soil and the canopy that is covered by vegetation such as forest or grass. It calculates water fluxes between these layers and the atmosphere.

In the land-surface-atmosphere interaction component, changes to the water balance caused by changes of the rainfall distribution can be observed directly. Other components of the GCM will also be affected by these changes, but only as a result of feedback and secondary processes. Due to feedback processes even small changes in the water balance of the land-surface component can have a significant effect in the GCM simulation. Good land-surface-atmosphere schemes are also needed, for example, to simulate the global impact of changes in local ecological structure, such as deforestation, see Pitman et al. (1990) and the references therein.

The GCM and the land-surface-atmosphere interaction model run on a grid of squares of side lengths 50km, 250km or more. All the parameters, for example temperature, rainfall intensity and solar radiation, are taken to be constant across the grid square. This is a realistic assumption for temperature or solar radiation, for rainfall it is over-simplification, because the typical scale for rainfall variability is much smaller. Lovejoy and Schertzer (1990a) found scaling behaviour of rainfall down to scales of 4cm, by using blotting paper. A consequence of this scale discrepancy is that low and high rainfall intensities are smeared out over the grid squares. This would lead to an overestimation of evaporation and an underestimation of run-off. Thus, Pitman et al. (1990) identified the need for a better rainfall representation in such models.

Researchers have modelled temporal and spatial rainfall distributions using cascades and compared the results with empirical data (Olsson, 1996b, 1998; Onof et al., 1996; Over and Gupta, 1994). In chapter 3 we investigate disaggregation using random cascades and show that this can lead to improved estimates in the water balance equations. We also introduce a version with spatial memory in the water stores which gives further improvements. For this we make use of the land-surface scheme MOSES (Gregory and Smith, 1990) which is a part of the UK Meteorological Office Unified Model, used for climate simulations. It is also used in the latest Hadley Centre model for climate studies, HADCM 3. MOSES is fully interactive with the atmosphere component and as such will describe change in land-atmosphere fluxes of heat, water and CO₂ within a perturbed climate.

Chapter 2

Fractal and multifractal properties of generalised Sierpiński triangles

In this chapter we introduce a self-affine variant of the Sierpiński triangle and a self-affine measure supported by this set. We determine the box dimension of the self-affine Sierpiński triangle and in certain cases the auxiliary function β and the Legendre multifractal spectrum of the measure. We do this to provide a new class of examples for analysis and to provide non-self-similar and non-isotropic measures on which to test algorithms for experimental determination of multifractal spectra, see (1.54). We also use these examples in our work on sections in chapter 5. A version of this has been published (Falconer and Lammering, 1998).

The definition of an iterated function system is given in section 1.1.3. Here we discuss self-affine fractals in \mathbb{R}^2 . Such a *self-affine* fractal F is the attractor of an IFS consisting of a set of affine contractions $S_i : \mathbb{R}^2 \rightarrow \mathbb{R}^2$

$$S_i(x) = T_i(x) + a_i, \quad (2.1)$$

for $i = 1, 2, \dots, m$, where $a_i \in \mathbb{R}^2$ is a translation vector, and $T_i \in \mathcal{L}(\mathbb{R}^2, \mathbb{R}^2)$ is the linear part of the transformation. Dimension calculations of certain self-affine fractals are discussed in Falconer (1992), Falconer and Marsh (1988), Falconer (1997), King (1995) and Olsen (1998b).

The familiar Sierpiński triangle is the attractor of three similarity transformations with ratio $1/2$. Calculation of the dimension of such self-similar sets is routine, see (1.25).

A generalisation of the Sierpiński triangle can be made by using affine transformations that are not necessarily similarities. An example of such a fractal is shown in figure 2.1. Taking D as the triangle with vertices $(0,0)$, $(1,0)$ and $(0,1)$, we assume that each pair of triangles $S_i(D)$ intersects in a single point on the side of D , so that the IFS attractor is topologically the same as the Sierpiński triangle. The mappings $S_{i_1} \circ \dots \circ S_{i_k}$ become difficult to handle in this generality. Therefore we examine a less general version where one of the three transformations is a similarity. Typical examples of this generalisation are shown in figure 2.2.

We fix parameters $0 < a, b < 1$. The *generalised Sierpiński triangle* is constructed by mapping the initial triangle D onto the three sub-triangles as indicated by the template figure 2.3. The IFS is given by the following three affine transformations, of which S_1 is a

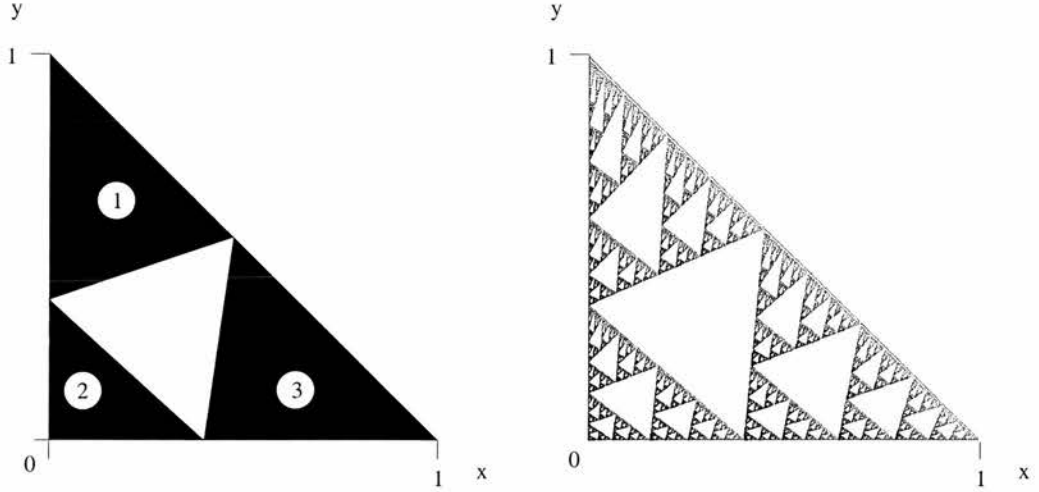


Figure 2.1: Template and realisation of a generalised Sierpiński triangle with three affine transformations

similarity:

$$\begin{aligned}
 S_1 \begin{bmatrix} x_1 \\ x_2 \end{bmatrix} &= \begin{bmatrix} 1-a & 0 \\ 0 & 1-a \end{bmatrix} \begin{bmatrix} x_1 \\ x_2 \end{bmatrix} + \begin{bmatrix} 0 \\ a \end{bmatrix} \\
 S_2 \begin{bmatrix} x_1 \\ x_2 \end{bmatrix} &= \begin{bmatrix} b & 0 \\ 0 & a \end{bmatrix} \begin{bmatrix} x_1 \\ x_2 \end{bmatrix} + \begin{bmatrix} 0 \\ 0 \end{bmatrix} \\
 S_3 \begin{bmatrix} x_1 \\ x_2 \end{bmatrix} &= \begin{bmatrix} 1-b & 1-a-b \\ 0 & a \end{bmatrix} \begin{bmatrix} x_1 \\ x_2 \end{bmatrix} + \begin{bmatrix} b \\ 0 \end{bmatrix},
 \end{aligned} \tag{2.2}$$

where $0 < a, b < 1$. An “art gallery” of generalised Sierpiński triangles with various values for a and b is shown in figure 2.4. The linear part of $S_{\mathbf{i}} = S_{i_1} \circ S_{i_2} \circ \dots \circ S_{i_k}$ is given by an upper triangular matrix

$$T_{\mathbf{i}} = \begin{bmatrix} t_{\mathbf{i}} & q_{\mathbf{i}} \\ 0 & s_{\mathbf{i}} \end{bmatrix}.$$

It is easy to calculate $t_{\mathbf{i}}$ and $s_{\mathbf{i}}$. In the next section we shall show that in certain cases we can estimate $q_{\mathbf{i}}$.

2.1 Matrix estimates

For $i = 1, 2, 3$, let n_i denote the number of occurrences of i in the sequence $\mathbf{i} = (i_1, \dots, i_k)$. Write $T_{\mathbf{i}}$ for the linear part of $S_{\mathbf{i}}$, so that in matrix terms,

$$\begin{aligned}
 T_1 &= \begin{bmatrix} 1-a & 0 \\ 0 & 1-a \end{bmatrix} \\
 T_2 &= \begin{bmatrix} b & 0 \\ 0 & a \end{bmatrix} \\
 T_3 &= \begin{bmatrix} 1-b & 1-a-b \\ 0 & a \end{bmatrix}.
 \end{aligned} \tag{2.3}$$

Then

$$T_{\mathbf{i}} = T_{i_1} \circ \dots \circ T_{i_k} = \begin{bmatrix} (1-a)^{n_1} b^{n_2} (1-b)^{n_3} & q_{\mathbf{i}} \\ 0 & (1-a)^{n_1} a^{n_2} a^{n_3} \end{bmatrix} \tag{2.4}$$

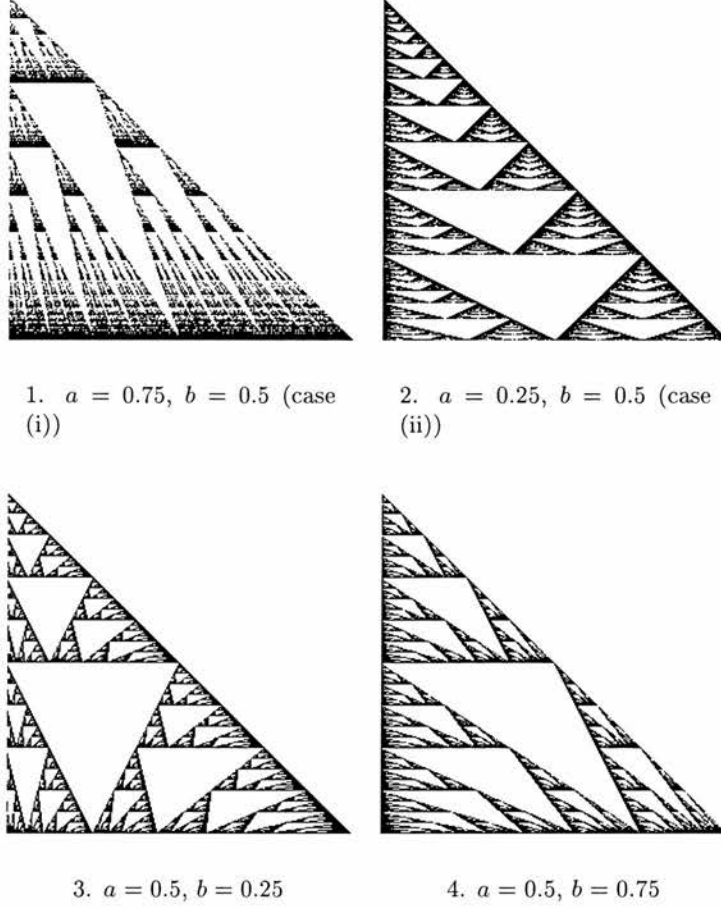


Figure 2.2: Typical generalised Sierpiński triangles with one similarity

for some q_i , which may be thought of as representing the shearing effect of T_i .

Lemma 2.1. *There exists a number c depending on a and b such that*

- (i) *If $a > 1 - b$ and $a \geq b$ then $|q_i| \leq cs_i$ for all i .*
- (ii) *If $a < 1 - b$ and $a \leq b$ then $|q_i| \leq ct_i$ for all i .*
- (iii) *If $a = 1 - b$ then $q_i = 0$ for all i .*

Proof. It is sufficient to show that the shearing term produced by multiplying combinations of T_2 and T_3 is bounded by a constant multiple of the other terms, as T_1 is just a scalar multiplication. For convenience we write

$$U_3 \equiv \frac{1}{1-b} T_3 = \begin{bmatrix} 1 & \lambda \\ 0 & \sigma \end{bmatrix},$$

where $\lambda = (1 - a - b)/(1 - b)$ and $\sigma = a/(1 - b)$. For $r \geq 0$

$$T_2^r U_3 = \begin{bmatrix} b^r & 0 \\ 0 & a^r \end{bmatrix} \begin{bmatrix} 1 & \lambda \\ 0 & \sigma \end{bmatrix} = \begin{bmatrix} b^r & \lambda b^r \\ 0 & \sigma a^r \end{bmatrix}.$$

Taking products of such matrices, we get

$$\begin{aligned} T_2^{r_1} T_3 T_2^{r_2} T_3 \dots T_2^{r_{m-1}} T_3 T_2^{r_m} &= (1-b)^{m-1} \cdot T_2^{r_1} U_3 T_2^{r_2} U_3 \dots T_2^{r_{m-1}} U_3 T_2^{r_m} \\ &= (1-b)^{m-1} \cdot \begin{bmatrix} b^{r_1+r_2+\dots+r_m} & q' \\ 0 & \sigma^{m-1} a^{r_1+r_2+\dots+r_m} \end{bmatrix}, \end{aligned}$$

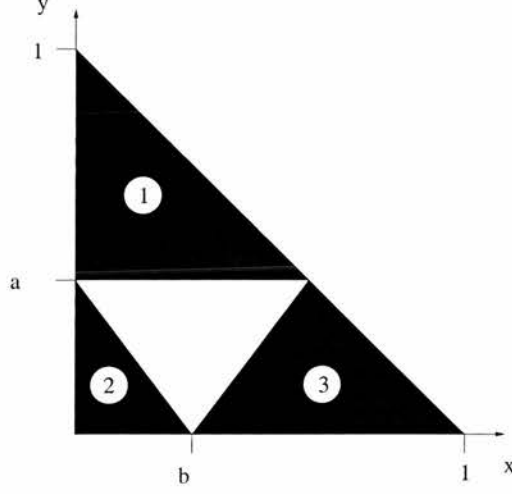


Figure 2.3: Template for a generalised Sierpiński triangle with one similarity

where by induction

$$q' = \lambda(b^{r_1+r_2+\dots+r_{m-1}}a^{r_m} + \sigma b^{r_1+r_2+\dots+r_{m-2}}a^{r_{m-1}+r_m} + \dots + \sigma^{m-2}b^{r_1}a^{r_2+\dots+r_m}).$$

Since all of the compositions (2.4) are of this form combined with scalar multiples contributed by the terms T_1 , the Lemma will follow if we show that q' is comparable to either $b^{r_1+r_2+\dots+r_m}$ or $\sigma^{m-1}a^{r_1+r_2+\dots+r_m}$

We estimate q' in each case:

(i) If $a > 1 - b$ and $b \leq a$ then $\sigma = a/(1 - b) > 1$, so

$$\begin{aligned} |q'| &= |\lambda|(b^{r_1+r_2+\dots+r_{m-1}}a^{r_m} + \dots + \sigma^{m-2}b^{r_1}a^{r_2+\dots+r_m}) \\ &\leq |\lambda|a^{r_1+\dots+r_m}(1 + \sigma + \dots + \sigma^{m-2}) \\ &\leq |\lambda|a^{r_1+\dots+r_m} \frac{\sigma^{m-2}}{1 - 1/\sigma} = \frac{\sigma^{-1}|\lambda|}{1 - 1/\sigma} (\sigma^{m-1}a^{r_1+\dots+r_m}) \end{aligned}$$

(ii) If $a < 1 - b$ and $b \geq a$ then $\sigma = a/(1 - b) < 1$, so

$$\begin{aligned} |q'| &= |\lambda|(b^{r_1+r_2+\dots+r_{m-1}}a^{r_m} + \dots + \sigma^{m-2}b^{r_1}a^{r_2+\dots+r_m}) \\ &\leq |\lambda|b^{r_1+\dots+r_m}(1 + \sigma + \dots + \sigma^{m-2}) \\ &\leq |\lambda|b^{r_1+\dots+r_m} \frac{1}{1 - \sigma} = \frac{|\lambda|}{1 - \sigma} b^{r_1+\dots+r_m}. \end{aligned}$$

(iii) If $a = 1 - b$ then $\lambda = 0$, so $q' = 0$.

□

2.2 Calculation of box-counting dimensions

A method for calculating the Hausdorff and box-counting dimension of certain self-affine fractals is described in Falconer (1992); Falconer and Marsh (1988). The *singular values*, $\alpha_1(T) \geq \alpha_2(T) \geq \dots \geq \alpha_n(T)$, of the linear transformation T on \mathbb{R}^n are the lengths of the principal semi-axes of the image $T(B)$ of the unit ball B , that is the eigenvalues of TT^* , where T^* is the adjoint of T . The *singular value function* $\phi^s(T)$ of T is defined for $0 \leq s \leq n$ as

$$\phi^s(T) = \alpha_1 \alpha_2 \dots \alpha_{m-1} \alpha_m^{s-m+1},$$

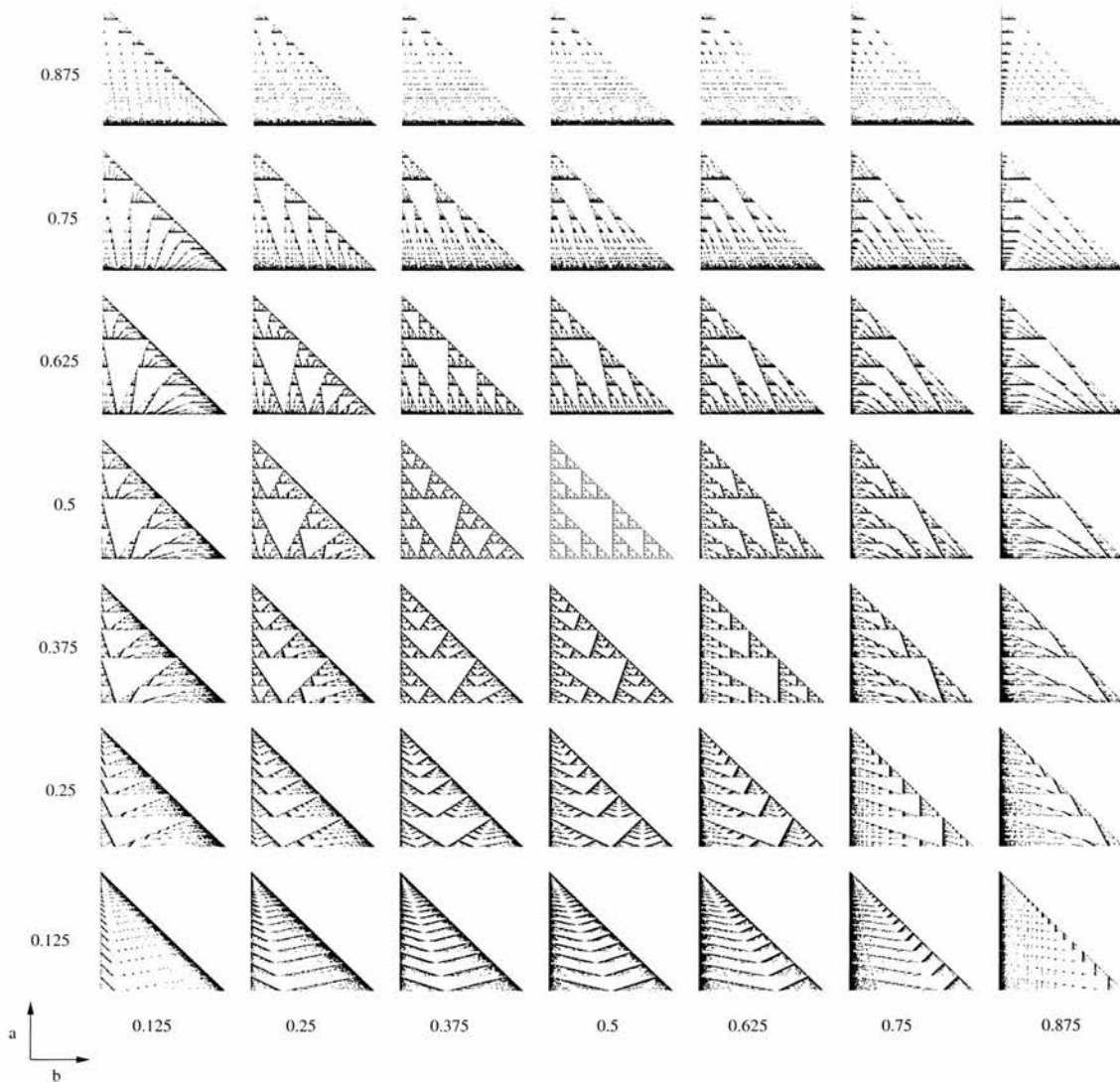


Figure 2.4: Generalised Sierpiński triangles for various values of a and b

where $m \in \mathbb{N}$ and $m - 1 \leq s < m$.

It can be shown that there is a unique positive s such that

$$\lim_{k \rightarrow \infty} \left[\sum_{|\mathbf{i}|=k} \phi^s(T_{\mathbf{i}}) \right]^{1/k} = 1. \quad (2.5)$$

Recall that the contractions S_1, \dots, S_k satisfy the open set condition if there exists a bounded non-empty open set U such that

$$U \supseteq \bigcup_{i=1}^k S_i(U).$$

This is satisfied by the generalised Sierpiński triangle taking U as the interior of the generating triangle D . According to Falconer and Marsh (1988) and Falconer (1992), the value of s given by (2.5) is the box-counting dimension of the set F provided that the contractions satisfy the open set condition and F has a connected component that is not contained in any straight line. Both of these conditions hold for generalised Sierpiński triangles, so in principle $\dim_B F$ is given by (2.5) for all generalised Sierpiński triangles.

In cases (i) and (ii) we can obtain an analytic expression for $\dim_B F$ by examining the singular values of the upper triangular matrices $T_{\mathbf{i}}$.

For a linear transformation T on \mathbb{R}^2 the singular values are $\alpha_1(T) = \|T\|_2$, where $\|\cdot\|_2$ is the norm induced by the Euclidean norm on \mathbb{R}^2 , and $\alpha_2(T) = (\det T)/\alpha_1(T)$. Thus the two singular values of $T_{\mathbf{i}}$ are comparable to the two diagonal elements $t_{\mathbf{i}}$ and $s_{\mathbf{i}}$ provided that $q_{\mathbf{i}}$ is small compared to $t_{\mathbf{i}}$ and $s_{\mathbf{i}}$, which is the case if (i) or (ii) of lemma 2.1 holds.

In this case there exist $c_1, c_2 > 0$ such that

$$\begin{aligned} c_1 \max(t_{\mathbf{i}}, s_{\mathbf{i}}) &\leq \alpha_1(T_{\mathbf{i}}) \leq c_2 \max(t_{\mathbf{i}}, s_{\mathbf{i}}) \\ c_1 \min(t_{\mathbf{i}}, s_{\mathbf{i}}) &\leq \alpha_2(T_{\mathbf{i}}) \leq c_2 \min(t_{\mathbf{i}}, s_{\mathbf{i}}) \end{aligned}$$

for all \mathbf{i} . Thus from (2.4) we obtain in case (i)

$$\begin{aligned} \alpha_1(T_{\mathbf{i}}) &\asymp (1-a)^{n_1(\mathbf{i})} a^{n_2(\mathbf{i})+n_3(\mathbf{i})} = s_{\mathbf{i}} \\ \alpha_2(T_{\mathbf{i}}) &\asymp (1-a)^{n_1(\mathbf{i})} b^{n_2(\mathbf{i})} (1-b)^{n_3(\mathbf{i})} = t_{\mathbf{i}}, \end{aligned}$$

and in case (ii)

$$\begin{aligned} \alpha_1(T_{\mathbf{i}}) &\asymp (1-a)^{n_1(\mathbf{i})} b^{n_2(\mathbf{i})} (1-b)^{n_3(\mathbf{i})} = t_{\mathbf{i}} \\ \alpha_2(T_{\mathbf{i}}) &\asymp (1-a)^{n_1(\mathbf{i})} a^{n_2(\mathbf{i})+n_3(\mathbf{i})} = s_{\mathbf{i}}, \end{aligned}$$

where \asymp means that the ratio of the terms on either side is bounded away from both 0 and ∞ for all \mathbf{i} .

Since the dimension of the generalised Sierpiński triangle is at least 1, the singular value function is given by

$$\phi^s(T_{\mathbf{i}}) = \alpha_1(T_{\mathbf{i}})\alpha_2(T_{\mathbf{i}})^{s-1},$$

where $\alpha_1(T_{\mathbf{i}}) \geq \alpha_2(T_{\mathbf{i}})$.

In case (i) the singular value function becomes

$$\begin{aligned} \phi^s(T_{\mathbf{i}}) &\asymp (1-a)^{n_1(\mathbf{i})} a^{n_2(\mathbf{i})+n_3(\mathbf{i})} ((1-a)^{n_1(\mathbf{i})} b^{n_2(\mathbf{i})} (1-b)^{n_3(\mathbf{i})})^{s-1} \\ &= (1-a)^{sn_1(\mathbf{i})} (ab^{s-1})^{n_2(\mathbf{i})} [a(1-b)^{s-1}]^{n_3(\mathbf{i})}. \end{aligned} \quad (2.6)$$

Summing over sequences of length k we get the partition sum

$$\begin{aligned} \sum_{|\mathbf{i}|=k} \phi^s(T_{\mathbf{i}}) &\asymp \sum_{|\mathbf{i}|=k} (1-a)^{sn_1(\mathbf{i})} (ab^{s-1})^{n_2(\mathbf{i})} [a(1-b)^{s-1}]^{n_3(\mathbf{i})} \\ &= [(1-a)^s + ab^{s-1} + a(1-b)^{s-1}]^k, \end{aligned} \quad (2.7)$$

using the multinomial theorem. In case (ii) the singular value function becomes

$$\begin{aligned} \phi^s(T_{\mathbf{i}}) &\asymp (1-a)^{n_1(\mathbf{i})} b^{n_2(\mathbf{i})} (1-b)^{n_3(\mathbf{i})} ((1-a)^{n_1(\mathbf{i})} a^{n_2(\mathbf{i})+n_3(\mathbf{i})})^{s-1} \\ &= (1-a)^{sn_1(\mathbf{i})} (a^{s-1}b)^{n_2(\mathbf{i})} [a^{s-1}(1-b)]^{n_3(\mathbf{i})}. \end{aligned} \quad (2.8)$$

Summing over sequences of length k we get the partition sum

$$\begin{aligned} \sum_{|\mathbf{i}|=k} \phi^s(T_{\mathbf{i}}) &\asymp \sum_{|\mathbf{i}|=k} (1-a)^{sn_1(\mathbf{i})} (a^{s-1}b)^{n_2(\mathbf{i})} [a^{s-1}(1-b)]^{n_3(\mathbf{i})} \\ &= [(1-a)^s + a^{s-1}]^k. \end{aligned} \quad (2.9)$$

Theorem 2.2. *The box-counting dimension of the generalised Sierpiński triangle is given by*

$$\dim_B F = \begin{cases} s : (1-a)^s + ab^{s-1} + a(1-b)^{s-1} = 1 & \text{if } a \geq 1-b \text{ and } b \leq a, \\ s : (1-a)^s + a^{s-1} = 1 & \text{if } a \leq 1-b \text{ and } b \geq a. \end{cases} \quad (2.10)$$

Proof. From the general theory of the dimensions of self-affine sets (2.5), using (2.7) and (2.9), the box-counting dimension takes the value of s given above. (The case of $a = 1 - b$, where two of the mappings are similarities follows easily from lemma 2.1 (iii).) \square

In general (2.10) cannot be explicitly solved in s . The results for some different values of a and b have been calculated numerically and figure 2.5 shows these values.

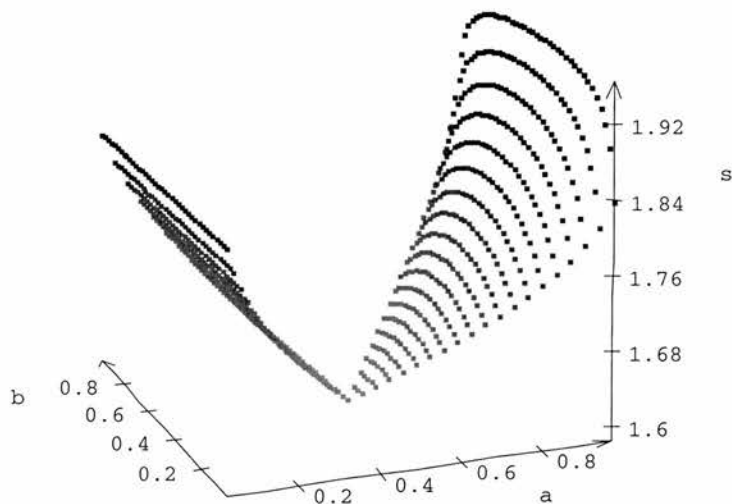


Figure 2.5: Dimension of Sierpiński triangle depending on a and b

We observe from figure 2.4 that the triangles in case (i) become long and thin in the direction of the y -axis. The triangles in case (ii) become long and thin in the direction along the x -axis. In the other cases the orientation of higher order component triangles varies from horizontal to vertical, which leads to difficulties in finding the box-counting dimension.

For the standard Sierpiński triangle ($a = b = 0.5$) we get the well-known result $s = \log 3 / \log 2$. The fractal dimension in the generalised cases studied is always higher. We also observe the surprising fact, that within case (ii) the box-counting dimension does not depend on b .

2.3 Multifractal calculations

It is natural to try to extend our analysis to a self-affine multifractal measure μ supported by a generalised Sierpiński triangle set F by associating weights w_i with the transformations S_i (fig 2.6). The analysis used in this section uses the coarse multifractal formalism, described in section 1.1.2

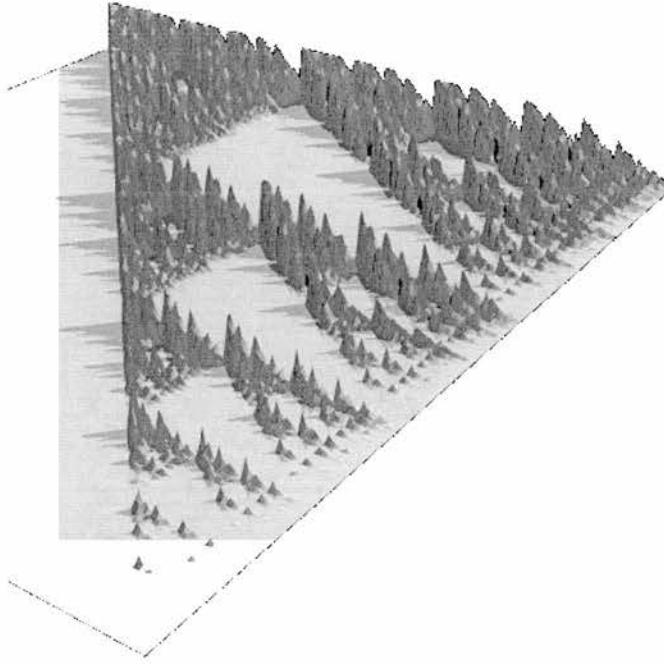


Figure 2.6: Multifractal measure on generalised Sierpiński triangle with $a = 0.4$, $b = 0.5$ and weights 0.3, 0.4 and 0.3.

We recall that given a WIFS consisting of a family of contractions $\{S_1, \dots, S_m\}$ and an associated set of weights, there exists a unique probability measure μ such that

$$\mu(B) = \sum_{i=1}^m w_i \mu(S_i^{-1}(B)) \quad (2.11)$$

for all sets $B \in \mathbb{R}^n$, see (1.26). Thus μ is obtained by repeated subdivision of mass in the ratios $w_1 : w_2 : w_3$ at each step of the construction of the generalised Sierpiński triangle. For a self-similar multifractal, where the similarities S_i have ratios $r_i (1 \leq i \leq m)$, $\beta(q)$ is given by

$$\sum_{i=1}^m w_i^q r_i^{\beta(q)} = 1, \quad (2.12)$$

provided the S_i satisfy a condition such as the strong separation condition or the open set condition, see (1.27). Thus for a self-similar measure on the standard Sierpiński triangle

$$\beta(q) = \frac{\log(w_1^q + w_2^q + w_3^q)}{\log 2},$$

as in (1.30).

We now find β for a self-affine measure supported by a generalised Sierpiński triangle in case (i). Thus S_1, S_2, S_3 are the affine transformations given by (2.2) with linear parts T_1, T_2, T_3 as given by (2.3), where $a \geq 1 - b$ and $a \geq b$. The self-affine measure supported by F is defined by (2.11), where $w_1, w_2, w_3 > 0$ and $w_1 + w_2 + w_3 = 1$.

We first consider the projection μ_V of the measure μ onto the vertical axis, so $\mu_V(B) = \mu(P^{-1}(B))$, where P denotes orthogonal projection from \mathbb{R}^2 to the y -axis. Clearly μ_V is

a self-similar measure supported by the unit interval, with similarity ratios $\{a, 1 - a\}$ and weights $\{w_2 + w_3, w_1\}$. Writing β_V for the β -function associated with μ_V , we have from (2.12) that

$$(1 - a)^{\beta_V(q)} w_1^q + a^{\beta_V(q)} (w_2 + w_3)^q = 1 \quad (2.13)$$

and in particular

$$\sum_{A \in \mathcal{I}_r} \mu_V(A)^q \asymp r^{-\beta_V(q)}, \quad (2.14)$$

where the sum is over the set \mathcal{I}_r of mesh intervals A of length r and $\mu(A) > 0$. (The validity of (2.13) and (2.14) follows from Arbeiter and Patzschke (1996) noting that the open set condition holds for the two similarities, or by routine direct estimation.)

We obtain $\beta(q)$ for μ by considering the projection of μ restricted to each triangle $S_i(D)$ onto the y -axis.

Theorem 2.3. *For a self-affine measure μ supported by a generalised Sierpiński triangle of case (i) (with $a \geq 1 - b$ and $a \geq b$), we have, for $q \geq 0$, that $\beta = \beta(q)$ is given by*

$$(1 - a)^\beta w_1^q + (a/b)^{\beta_V(q)} b^\beta w_2^q + \left(\frac{a}{1-b}\right)^{\beta_V(q)} (1-b)^\beta w_3^q = 1, \quad (2.15)$$

where $\beta_V(q)$ is given by

$$(1 - a)^{\beta_V(q)} w_1^q + a^{\beta_V(q)} (w_2 + w_3)^q = 1. \quad (2.16)$$

Proof. Fix ϵ such that $0 < \epsilon < (1 - a)/b$. Then we may use the trapezium K with vertices $(0, 0), (0, 1), (\epsilon, 1), (1, 0)$ as a template for the construction of F ; In fact the interior of K satisfies the open set condition for S_1, S_2, S_3 in case (i), see figure 2.7.

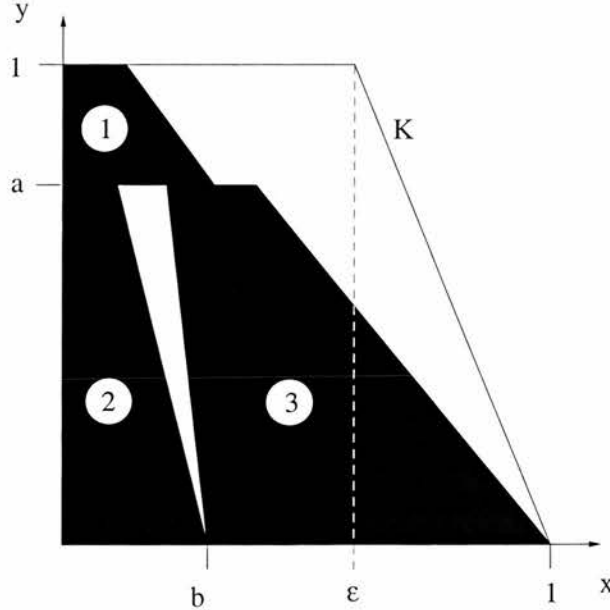


Figure 2.7: Template for case (i) based on the trapezium K

Fix $\mathbf{i} = i_1, \dots, i_k$ for the time being and consider the trapezium $K_{\mathbf{i}} = S_{\mathbf{i}}(K)$. Note that $K_{\mathbf{i}}$ has its base and the top sides parallel to x -axis, has height $h_{\mathbf{i}}$, base length $b_{\mathbf{i}}$ and top length $\epsilon b_{\mathbf{i}}$, where

$$h_{\mathbf{i}} = (1 - a)^{n_1} a^{n_2 + n_3}, \quad (2.17)$$

$$b_{\mathbf{i}} = (1 - a)^{n_1} b^{n_2} (1 - b)^{n_3}, \quad (2.18)$$

$$\mu(K_{\mathbf{i}}) = w_1^{n_1} w_2^{n_2} w_3^{n_3}, \quad (2.19)$$

where n_i is the number of occurrences of the digit i ($i = 1, 2, 3$) in $\mathbf{i} = i_1, \dots, i_k$. Divide $K_{\mathbf{i}}$ by cuts parallel to the x -axis into $\lceil h_{\mathbf{i}}/b_{\mathbf{i}} \rceil$ sub-trapeziums $K_{\mathbf{i}}^j$ of equal height, a height which will certainly be between $\frac{1}{2}b_{\mathbf{i}}$ and $b_{\mathbf{i}}$. The projection of μ restricted to $K_{\mathbf{i}}$ onto the y -axis is a similar image of μ_V under a length scaling of $h_{\mathbf{i}}$ and mass scaling of $\mu(K_{\mathbf{i}})$. Thus

$$\sum_j \mu(K_{\mathbf{i}}^j)^q = \mu(K_{\mathbf{i}})^q \sum_j \mu_V(I^j)^q, \quad (2.20)$$

where the intervals I^j are a division of the unit interval on the y -axis into $\lceil h_{\mathbf{i}}/b_{\mathbf{i}} \rceil$ equal sub-intervals. Using (2.14) writing $\beta_V = \beta_V(q)$, and (2.17) - (2.19)

$$\begin{aligned} b_{\mathbf{i}}^\beta \sum_j \mu(K_{\mathbf{i}}^j)^q &\asymp b_{\mathbf{i}}^\beta \mu(K_{\mathbf{i}})^q (b_{\mathbf{i}}/h_{\mathbf{i}})^{-\beta_V} \\ &\asymp [(1-a)^\beta w_1^q]^{n_1} [a^{\beta_V} b^{\beta-\beta_V} w_2^q]^{n_2} [a^{\beta_V} (1-b)^{\beta-\beta_V} w_3^q]^{n_3}, \end{aligned} \quad (2.21)$$

where $\mathbf{i} = i_1, \dots, i_k$ contains $n_j = n_j(\mathbf{i})$ digits j for $j = 1, 2, 3$.

Writing $z_{\mathbf{i}}$ for the right-hand side of (2.21), we have $z_{\mathbf{i}} = z_1^{n_1} z_2^{n_2} z_3^{n_3}$, where $z_1 = (1-a)^\beta w_1^q$, $z_2 = a^{\beta_V} b^{\beta-\beta_V} w_2^q$ and $z_3 = a^{\beta_V} (1-b)^{\beta-\beta_V} w_3^q$. Provided condition (2.15) is satisfied, $z_1 + z_2 + z_3 = 1$, so by a routine induction argument based on a multinomial expansion we get that $\sum_{\mathbf{i} \in \mathcal{S}} z_{\mathbf{i}} = 1$ for every stopping \mathcal{S} . (A *stopping* is a set \mathcal{S} of finite sequences with the property that for every infinite sequence i_1, i_2, \dots there is exactly one integer k with $i_1, \dots, i_k \in \mathcal{S}$.)

Given $0 < r < 1$, take \mathcal{S}_r to be the stopping

$$\mathcal{S}_r = \{\mathbf{i} = i_1, \dots, i_k : b_{i_1, \dots, i_{k-1}} > r > b_{i_1, \dots, i_k}\}$$

(so the base lengths of $K_{\mathbf{i}}$ are roughly equal to r if $\mathbf{i} \in \mathcal{S}_r$). With β satisfying (2.15), we have

$$\sum_{\mathbf{i} \in \mathcal{S}_r} b_{\mathbf{i}}^\beta \sum_j \mu(K_{\mathbf{i}}^j)^q \asymp \sum_{\mathbf{i} \in \mathcal{S}_r} z_{\mathbf{i}} = 1,$$

so

$$\sum_{\mathbf{i} \in \mathcal{S}_r} \sum_j \mu(K_{\mathbf{i}}^j)^q \asymp r^{-\beta}, \quad (2.22)$$

since $r \min\{b, 1-b\} < b_{\mathbf{i}} \leq r$ if $\mathbf{i} \in \mathcal{S}_r$.

Observe that there are numbers $0 < a, b < \infty$ and $0 < \theta \leq \pi/2$ such that for all $\mathbf{i} \in \mathcal{S}_r$ the base lengths, top lengths and heights of $K_{\mathbf{i}}^j$ lie between ar and br , and also the angles between the sides of $K_{\mathbf{i}}^j$ and the x -axis are at least θ . The $K_{\mathbf{i}}^j$ have disjoint interiors, so a routine argument, comparing the sums in (2.22) with the sums over mesh squares of sides λr (for suitably small and large values of λ) gives

$$\sum_{A \in \mathcal{M}_r} \mu(A)^q \asymp r^{-\beta} \quad (2.23)$$

for $0 < r < 1$, provided $q \geq 0$, where \mathcal{M}_r are mesh squares of side r . \square

Note that, for $0 < t < 1$, the generalised Sierpiński triangle for $a = t, b = 1-t$ is a reflection of that with $a = 1-t, b = t$. Thus we can find $\beta(q)$ in all cases with $a = 1-b$ as above.

Another way of describing multifractal properties of a measure is by the *generalised dimensions* D_q , related to β by

$$D_q = \frac{\beta(q)}{1 - q} \tag{2.24}$$

for $q \neq 1$ (Evertsz and Mandelbrot, 1992; McCauley, 1993). Thus in the cases covered by Theorem 2.3, we can read off D_q for $q \geq 0$ (using continuity at $q = 1$). Figures 2.8, 2.9 and 2.10 show numerical calculations of (2.15), (2.16) and (2.24) for a measure of case (i). The multifractal spectrum in figure 2.10 was calculated using the Legendre transform, (1.19), (1.20). Note that the intersection of $D(q)$ with the D -axis and the maximum of $f(\alpha)$ give the dimension of the support $D_0 = f(\alpha(0)) = 1.719$.

One of the main aims of studying these generalised Sierpiński triangle constructions is to provide non-isotropic and non-homogeneous multifractal measures where the multifractal spectrum has been calculated analytically, for testing algorithms, see section 1.3.4 and chapter 5. Nevertheless, the constructions of this chapter leave many open problems. Clearly one would like to calculate the box dimension for generalised Sierpiński triangles that do not fall into cases (i) and (ii). Hausdorff dimension calculations would also be of interest. Again, one would like to extend the multifractal calculations to further instances. One would hope that $f(\alpha) = \dim_H \{x : \lim_{r \rightarrow 0} \ln \mu(B(x, r)) / \ln r = \alpha\}$ is the Legendre transform of $\beta(q)$, where \dim_H denotes Hausdorff dimension. However, such calculations can be difficult in non self-similar situations; the lack of strong separation between the components presents difficulties akin to those encountered in work on multifractals on Sierpiński carpets (King, 1995; Olsen, 1998b).

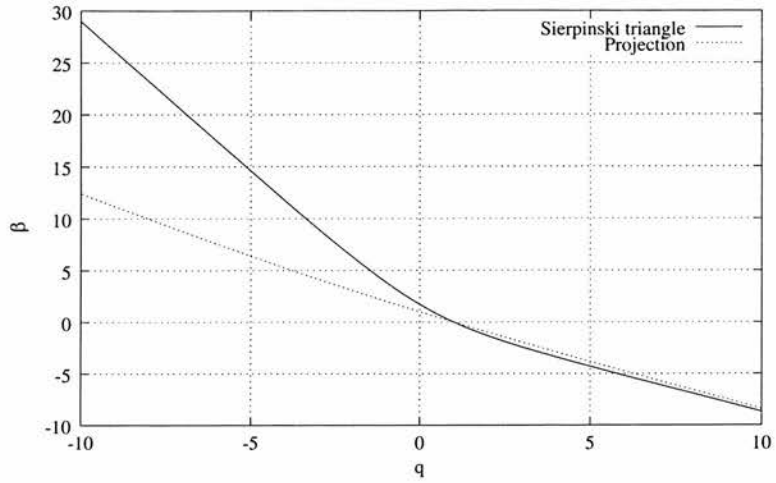


Figure 2.8: $\beta(q)$ for the self-affine measure with weights $w_1 = 0.3, w_2 = 0.4, w_3 = 0.3$ and $a = 0.75, b = 0.4$

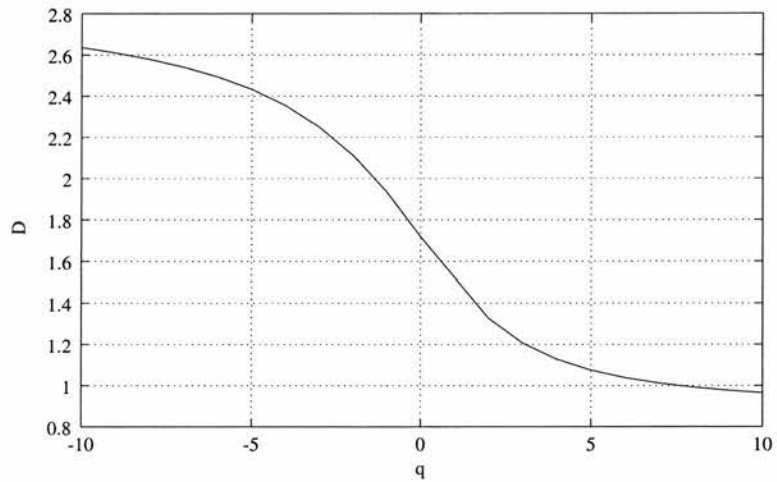


Figure 2.9: Generalised dimensions of the same measure as in figure 2.8

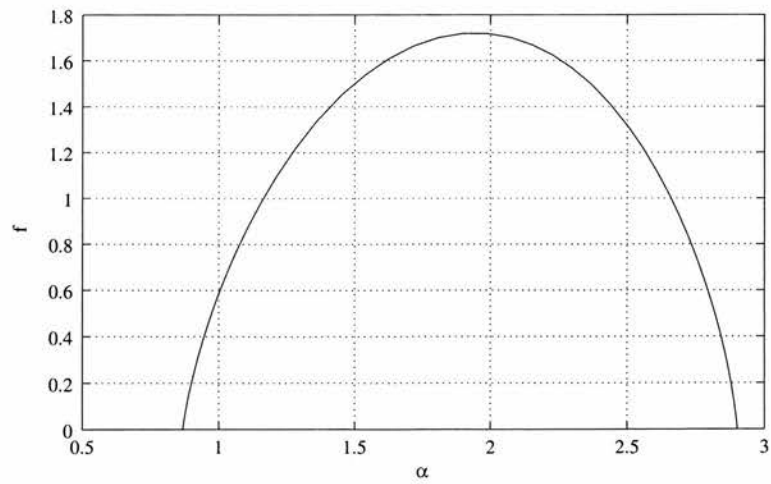


Figure 2.10: Multifractal spectrum of the same measure as in figure 2.8

Chapter 3

Improvement of water balance in climate simulation by random cascade disaggregation of rainfall

In this chapter a random cascade disaggregation of spatial rainfall is incorporated into the one-dimensional hydrological component of the UK Meteorological Office Surface Exchange Scheme (MOSES) used in their General Circulation Model (GCM). The results of several simulations using exponentially distributed, disaggregated and evenly distributed rainfall are compared. The changes in the water balance, in particular the throughfall and the evaporation from the canopy are assessed. It is shown that a disaggregation using random cascades gives closer values to the reference simulation of canopy evaporation and throughfall variables than the conventional approach. Material from this chapter has been published (Lammering and Dwyer, 2000).

3.1 Overview

General Circulation Models (GCMs) operate on spatial scales of the order of tens of thousands of square kilometres. Rainfall, however, exhibits variability at much smaller scales. This spatial variability must be accounted for in GCMs if a realistic water balance is to be achieved as the water balance is generally governed by nonlinear point process equations which will give erroneous results if applied to the spatially averaged rainfall. As pointed out by Pitman et al. (1990), for example, averaging the rainfall evenly over the domain and applying nonlinear interception evaporation equations to the average will generally result in more evaporation than calculating evaporation at each point and integrating over the grid.

One method of incorporating the spatial variability of rainfall into GCMs is explained by Shuttleworth (1988). This and related methods are discussed in section 3.2, but essentially a negative-exponential probability distribution is used to describe the variability in rainfall intensity over a fraction of the GCM grid. The distribution can be worked through the water balance equations parametrically as detailed in section 3.4. The principal advantage of this and other parametric methods is computational simplicity - not requiring disaggregation of the rainfall field or multiple water balance calculations. The principal drawbacks are lack of physical realism and the absence of spatial memory of where rain falls from one GCM time step to the next.

Another approach would be to disaggregate the grid-average rainfall given by the GCM to simulate rainfall on a set of subgrids. Water balance equations could be performed for each subgrid and the results summed to give the grid-total evaporation, canopy throughfall

etc. This has the disadvantage of greatly increased computational effort, but the advantage of spatial memory of rainfall between time steps.

The focus of this chapter is to compare the water balance calculations (principally canopy evaporation and throughfall) resulting from these two approaches. Accordingly, the one-dimensional hydrological component of the UK Meteorological Office Surface Exchange Scheme (MOSES) was operated off-line. Several rainfall schemes are compared, as described below, to assess differences between parametrisation and disaggregation, and the effect of spatial memory.

3.2 Background

Shuttleworth (1988) acknowledges the work of others in proposing a model whereby rain falls on a fraction u of the grid, over which the local rainfall intensities P_l have a probability density function $f(P_l)$. Assuming a negative exponential distribution and normalising gives

$$f(P_l) = (u/P) \exp(-uP_l/P), \quad (3.1)$$

where P is the grid-average rainfall rate given by the GCM for a given time step and u is the wet fraction of the grid. If an aspect of the water balance (e.g. evaporation) at a point is given by $G_l = g(P_l)$, then the mean of that process, G , over the whole grid for the time step is given by

$$G = \int_0^\infty g(P_l) f(P_l) dP_l. \quad (3.2)$$

Thus, provided the complete water balance at a point is described by closed form expressions, the complete water balance averaged over the grid can be calculated as integrals in the above form. These area-averaged values can then be propagated to the next time step of the GCM. If the function g is linear in P_l then $G = g(P)$ - that is the point process equation applied directly to the grid-average rainfall.

The performance of this scheme was investigated by Dolman and Gregory (1992) using a one-dimensional, off-line version of the UK MO Surface Scheme configured for a area covered by a grass canopy. Testing values for u of 0.1 and 0.3 for convective rainfall, and 0.3 and 1.0 for frontal rainfall, they report that this parametrisation significantly improves the estimation of interception losses when compared to field data. Performance was slightly better when the canopy scheme allowed throughfall to occur prior to canopy saturation. Good performance of this distribution is also reported by Henderson-Sellers and Pitman (1991) when used in a hydrological model of a 196km² river basin in Australia.

The main advantage of this parametrical distribution is that it accounts for some spatial variability while avoiding computationally expensive calculations at a finer grid scale. It is also simple to apply. A drawback is that the fractional coverage u and the density $f(P_l)$ are poorly defined. They may vary geographically, seasonally, temporally and with storm type, although such variation can in principle be investigated and described. Recent descriptions of rainfall in terms of multifractal geometry, see Lovejoy and Schertzer (1995) suggest that descriptors that relate better to the mechanism that generates the rainfield can be found by investigating cascades. Another fundamental drawback is that, having accounted for spatial variability, the moisture stores (e.g. canopy wetness) are effectively averaged out over the grid at the end of each time step. That is, no memory is retained of where rain falls and how the resulting moisture stores are distributed in space. If

memory did exist it would undoubtedly affect the water balance in the next time step (e.g. by increased throughfall from the saturated areas of the canopy). Rowntree and Lean (1994) conclude that this is the reason for unsatisfactory results of this scheme in their comparative study.

Various ways of overcoming these problems have been tried. Entekhabi and Eagleson (1989) address the problem of averaged-out soil moisture stores by introducing a probability density function for soil saturation. Runoff equations are therefore integrated first over a distribution of rainfall intensities and then over a distribution of functional soil saturations. Johnson et al. (1993) tested the Entekhabi and Eagleson scheme using a GCM of the NASA Goddard Institute for Space Studies with promising results over the tropics using $u = 0.15$ for convective rainfall. Similarly Eltahir and Bras (1993b) investigated refinements to the canopy scheme including a negative exponential distribution for canopy storage. Using the Biosphere-Atmosphere Transfer Scheme (BATS) they report that the refinements reduce interception losses by half. Neither of these experiments, however, isolates the effect of introducing moisture storage distributions, nor considers the situation of dependency between the rainfall and storage distributions.

Eltahir and Bras (1993a) tackled the problem of the variation of u with time and location by proposing that u should be proportional to the GCM rain rate in a way depending on location. Experimentation by Dolman and Gregory (1992) however, found that this caused serious underestimation of interception losses.

Comparative studies (Pitman et al., 1990; Polcher et al., 1996; Xu et al., 1996) of parametric hydrological schemes operating at the GCM spatial scale all conclude that the choice of scheme is less important than the choice of parameter values when fitting model simulations to observed data.

3.3 The model

The Meteorological Office Surface Exchange Scheme (MOSES) (Gregory and Smith, 1990) is a part of the UK Meteorological Office Unified Model, used for climate simulations. It is also used in the latest Hadley Centre model for climate studies, HadCM 3. Moses is fully interactive with the atmosphere component and as such will describe change in land-atmosphere fluxes of heat, water and CO₂ within a perturbed climate.

In this study MOSES was operated off line. Here, we are concerned with the effect of different ways of representing rainfall upon throughfall and evaporation from the vegetation canopy. This is the first and most direct partition of the rainfall between infiltration to the ground and interception losses to the atmosphere. The parametrisations of the hydrological processes in these layers used in MOSES are explained in Gregory and Smith (1990). The canopy is assumed to be spatially uniform and to have a maximum water capacity of C_m [kg/m²] and actual water content of C [kg/m²]. Local throughfall T_l [kg/m²/s] for any one GCM time step t [s] is related to local rainfall P_l [kg/m²/s] in a way that depends on whether the canopy becomes saturated during the GCM time step:

$$T_l = \begin{cases} P_l - (C_m - C)/t & \text{if } P_l > C_m/t \\ P_l(C/C_m) & \text{if } P_l \leq C_m/t. \end{cases} \quad (3.3)$$

The upper expression represents a canopy that saturates during the time step, whereas the lower expression is the case where the local canopy is not saturated (content stays less than capacity) during the time step.

The derivation of (3.3) is based upon a canopy which allows a proportion C/C_m of any rainfall to fall through while the remainder is stored in the canopy, see Dolman and Gregory

Canopy storage	0.0 kg/m ² /s
Soil moisture concentration - layer 1	22.53 kg/m ²
Soil moisture concentration - layer 2	54.03 kg/m ²
Soil moisture concentration - layer 3	128.88 kg/m ²
Soil moisture concentration - layer 4	526.04 kg/m ²
Deep soil temperature - layer 1	286.28 K
Deep soil temperature - layer 2	286.01 K
Deep soil temperature - layer 3	282.50 K
Deep soil temperature - layer 4	280.94 K
Total water flux from surface	4.95 · 10 ⁻⁷ kg/m ² /s

Table 3.1: Initial conditions

(1992) for a comparison of this with an alternative canopy description. Evaporation from the canopy E_C [kg/m²/s] is removed from the canopy prior to any throughfall calculations according to

$$C^* = C - E_C t, \quad (3.4)$$

where C^* is the updated canopy content and E_C is given by

$$E_C = (C/C_m) \frac{(q_{sat}(T_0) - q_1) \rho}{r_a}, \quad (3.5)$$

with ρ the surface air density, q_1 the atmospheric surface humidity, $q_{sat}(T_0)$ the saturated specific humidity at surface temperature T_0 and r_a is the aerodynamic resistance.

The MOSES also contains a multi-layered soil hydrology scheme which calculates runoff, drainage, bare soil evaporation and vegetation transpiration. The details are not relevant to the analysis reported here.

3.4 Model runs

The MOSES was run using input forcing data from a meteorological station at Wallingford, UK. This consists of wind speed, temperature, surface short-wave radiation, surface net radiation and specific humidity. Rainfall data were prescribed using calibrated radar data from a weather radar located at Chemies, London. This data covers a base square of 128km × 128km (in the form of 64 × 64 grid squares of side 2km each) which includes Wallingford. For reference, table 3.1 gives some examples of the initial conditions for the beginning of the simulation on 1 May 1997. They were obtained by running the simulation from 1 January until 30 April 1997 with an exponential rainfall distribution. In table 3.2 a summary of some of the important vegetation and soil parameters used are given. Because much of the area is agricultural, a grass canopy was adopted. The differences between the schemes would be more obvious if the canopy was more substantial. That is, a canopy such as rainforest increases the effect of the disaggregation on the water balance. Although this would result in unrealistic values for the region (South England), such results would be valuable since not the region itself is under investigation but the new approach of representing rainfall in land-surface models. The model run covered the two months of May and June, 1997, during which two large rain storms occurred.

3.4.1 Rainfall representations

Several schemes for calculating the water balance equations and in particular the throughfall and the canopy evaporation were investigated - these are described below. In all of

Snow free albedo of vegetation	0.194
Canopy water capacity	0.63 kg/m ²
Stomatal resistance to evaporation	70.0 s/m
Root depth	1.0 m
Vegetative roughness length	0.038 m
Vegetation fraction used in calculation of infiltration rate	0.95
Infiltration enhancement factor used in calculation of infiltration rate	1.68
Clay fraction	0.23
Sand fraction	0.27
Soil thermal conductivity	0.23 W/m/K
Soil heat capacity	1.19 · 10 ⁶ J/K/m ³

Table 3.2: Vegetation and soil parameters

these the MOSES model with a time step of 15 minutes is used. For each step the input data comprises canopy content C and mean rain rate P for the base square, and the output C' is the canopy content after the time step with throughfall and evaporation calculated from (3.3) and (3.5) respectively. Thus, each C is obtained from the previous time step calculation and P is from the external forcing data provided by the radar.

Some schemes involve local spatial memory. Here the values of C_l and other water store content parameters for each grid square are also carried to the next time step. In these cases the MOSES model runs on each grid square independently taking as input the forcing data and the rainfall data disaggregated according to the scheme used. The output is the mean value of the respective water store contents. The rainfall schemes are as follows.

Flat The water balance equations (3.3) are applied directly to the mean rain rate P . That is, rain is assumed to fall evenly over the entire GCM square (also resulting in an even canopy storage).

Exponential This is the commonly practised approach as described by (3.1) and (3.2). That is, rain is assumed to fall over a fraction u of the GCM grid with rainfall intensities varying according to a negative exponential distribution. Substituting (3.1) and (3.3) into (3.2) by equating the process function G in (3.2) to the throughfall function in (3.3) we obtain

$$T = \frac{uC}{PC_m} \int_0^{\frac{C_m}{t}} P_l \exp(-u\frac{P_l}{P}) dP_l + \frac{u}{P} \int_{\frac{C_m}{t}}^{\infty} (P_l - \frac{C_m - C}{t}) \exp(-\frac{uP_l}{P}) dP_l, \quad (3.6)$$

where T is throughfall averaged over the wet fraction u of the grid. Integrating by parts and multiplying by u gives the grid averaged throughfall for each time step, namely

$$T^* = P(1 - \frac{C}{C_m}) \exp(-\frac{uC_m}{Pt}) + P\frac{C}{C_m}. \quad (3.7)$$

A similar expression can be found for grid-averaged evaporation, E_C , over each time step using (3.5). The grid-averaged canopy content is updated accordingly. Thus the rainfall distribution equation is carried through the water balance equations parametrically without the need for a finer subgrid. Note that the scheme effectively assumes that canopy moisture is always evenly distributed over the grid. Here $u = 0.2$ is used and P prescribed

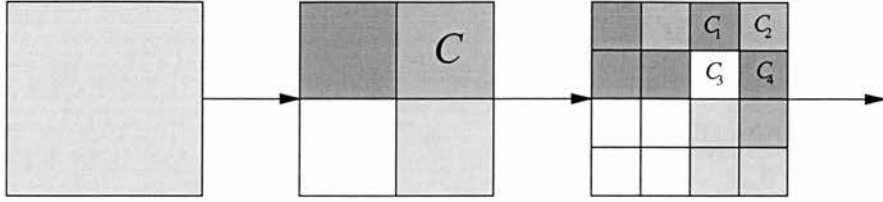


Figure 3.1: Cascade construction - shading indicates rainfall intensity

j	a_j	p_j
0	0	0.235
1	0.48	0.255
2	0.125	0.255
3	0.375	0.255

Table 3.3: Parameters used by random cascade disaggregation

by the average rainfall rate over the 64×64 grid points of the radar image. For a description of the surface hydrology processes used in the UK Meteorological Office Unified Model system see Gregory and Smith (1990).

Cascade process without memory An approach to disaggregating spatial rainfall is to use realisations of random cascades. In section 1.4 evidence was given that random cascade processes are more appropriate than “ad hoc subgrid parametrisations” for simulating the distribution of rainfall.

In the notation of chapter 1, $\mu(A)$ denotes the total rainfall rate over the region A , in m^3/s . Thus the average rainfall rate over A is $\mu(A)/\text{area}(A)$. A binary random cascade process replaces uniform rainfall distribution on the base square by a more realistic and irregular distribution across the grid squares. This is achieved by utilising a random cascade process with discrete weights as introduced in section 1.2.4.

The random cascade can be thought of as repeated random subdivision of the rainfall data corresponding to repeated subdivision of squares into 2×2 subsquares. At each step $\mu(C)$, representing the overall rainfall rate on the square C , is replaced by values on each subsquare according to a random distribution which on average conserves the overall rain rate (fig 3.1). The random ratios used for each square after each subdivision are independent and identical. In this case a cascade of six such steps to disaggregate the rainfall on the base square into 64×64 grid squares is used.

Thus, if C is a l -th level square with assigned overall rain rate P_C , the subsquares C_1, C_2, C_3, C_4 are independently assigned rain rates WP_C where in our case $\mathbb{P}(W = a_j) = p_j$ for $j = 0, 1, 2, 3$ (fig 3.1), where \mathbb{P} denotes probability. In the notation of section 1.2.4, W_1, W_2, W_3, W_4 are independent identically distributed random vectors with the distribution of W .

The variability in the random cascade is determined by the parameters p_j and a_j . For instance, by choosing all a_j to be close to $1/4$ one could generate cascades with an even distribution, or by choosing one a_j to be very large and the correspondent p_j to be small, a cascade is generated with few areas of very high intensity.

For our disaggregation model the parameters a_j and p_j are given in table 3.3. The probability of zero rainfall, p_0 , is set to reflect the typical wet fraction $u = 0.2$ observed in the radar images during the rainy periods. A branching process argument for the expected

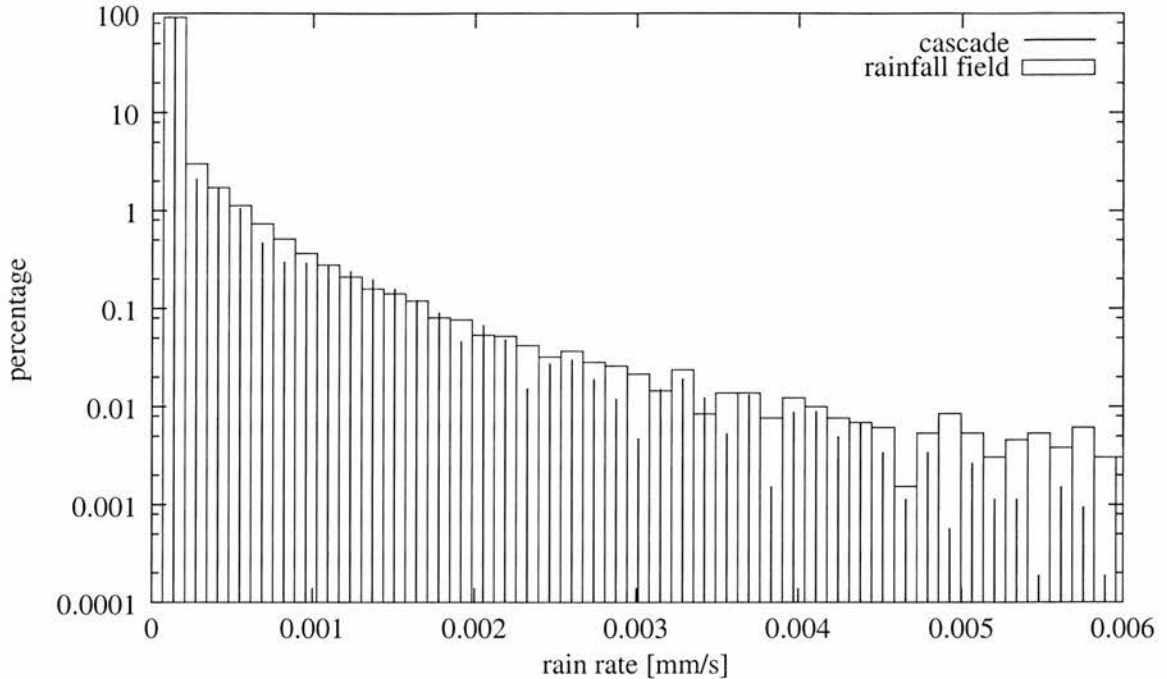


Figure 3.2: Histogram of the 32 random cascades and rainfall fields from figure 3.4.1

number of l -th level squares with no rainfall gives

$$p_0 = 1 - u^{1/l}, \quad (3.8)$$

where u is the proportion of the l -th level squares with positive rain rate, see (1.46). The other parameters are arbitrarily chosen such that the resulting cascades have a widely varying intensity distribution and $4 \sum a_j p_j = 1$, given by (1.43), is fulfilled so that the rainfall is conserved on average at each stage of the cascade construction. Therefore a_1 and was chosen to be substantial greater than $1/4$ and a_2 much smaller than $1/4$. The probabilities p_1 , p_2 and p_3 are chosen to be identical.

For a visual comparison of random cascades and actual rainfall radar data see figure 3.4.1. The radar images were taken at 15min intervals. on the 10th of May 1997. Note that the goal was not to simulate the exact shape of the rainfield, but to create a distribution with the same intensity variation. The histogram in figure 3.2 shows that the intensity distributions of the cascades and the rainfall fields coincide.

The rainfall forcing data is radar data averaged over the domain. Before every time step a random cascade is generated and normalised to give an overall mean rain rate P . The simulation runs with these values on each grid square for one time step. The canopy content and other moisture stores are averaged over the domain at the end of each time step.

The realisations of the random cascade for each time step are independent. Therefore the results of this experiment should be comparable with the results of the *radar without memory simulation* (see below).

This cascade process conserves the overall rainfall on average but nevertheless the generated distribution is normalised such that the overall rainfall matches the overall rainfall in the radar image. Since $p_0 > 0$ there is a small positive probability of total extinction. In that case a new cascade is generated for the particular time step.

Cascade process with memory In this simulation the rainfall is disaggregated using the same cascade process as before. However the canopy and other water stores of the

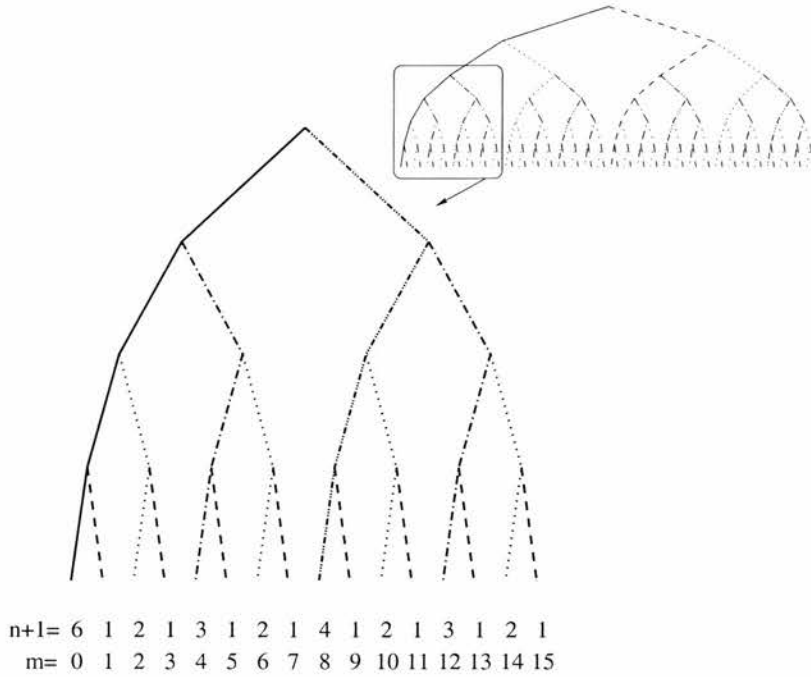


Figure 3.3: Scheme for the reuse of previous disaggregation steps for dependent random cascades: The initial step is the 0-th time step. For the m -th time step let n be the largest integer ≤ 5 such that 2^n divides m . Then we modify the cascade process from the $(6 - n)$ -th level downwards of the hierarchy by resampling the multipliers of the $n + 1$ deepest levels, whilst retaining the multipliers of the other levels from the previous time step.

model are not averaged after each time step. This is achieved by running the MOSES for each grid square separately using as input the radar data averaged over the domain. In this way spatial memory of water stores is introduced into the model.

In contrast to the *cascade without memory* approach no independent cascades are generated for every time step. Instead, a dependence between the cascades of different time steps is chosen such that an evolving rainfall field is mimicked. That means the short term change in the distribution must be small but after a certain number of time steps the distribution must change completely.

During each cascade construction the ratios of the rainfall redistributions are memorised. In the following cascade construction the first redistributions of a certain number are repeated. The number of repeated disaggregations is estimated in the following way. At time $m = 0$ a complete cascade is generated with 6 new disaggregation steps. At the next time step, $m = 1$, only the final (level 6) disaggregation is performed anew, the previous 5 disaggregations are taken over from time step $m = 0$. In time step $m = 2$ only the first 4 disaggregations are taken over from $m = 1$ and the final 2 (level 5 and 6) are performed anew. In the next time step the number of newly generated disaggregations is 1, then follow 3, 1, 2, 1, 4, ...

This process is continued until at $m = 32$ a whole new cascade with 6 new disaggregations is generated and the process starts over again. The binomial tree in figure 3.3 indicates the number $n + 1$ of disaggregations that are generated anew.

A completely new cascade is generated every 32 time steps. With a time step of 15 minutes this would correspond to a complete change of the rainfall pattern every 8 hours, which is not unrealistic. For a visual comparison of a series of dependent random cascades and rainfall radar images see figure 3.4.1. The developments of the rainfield and the

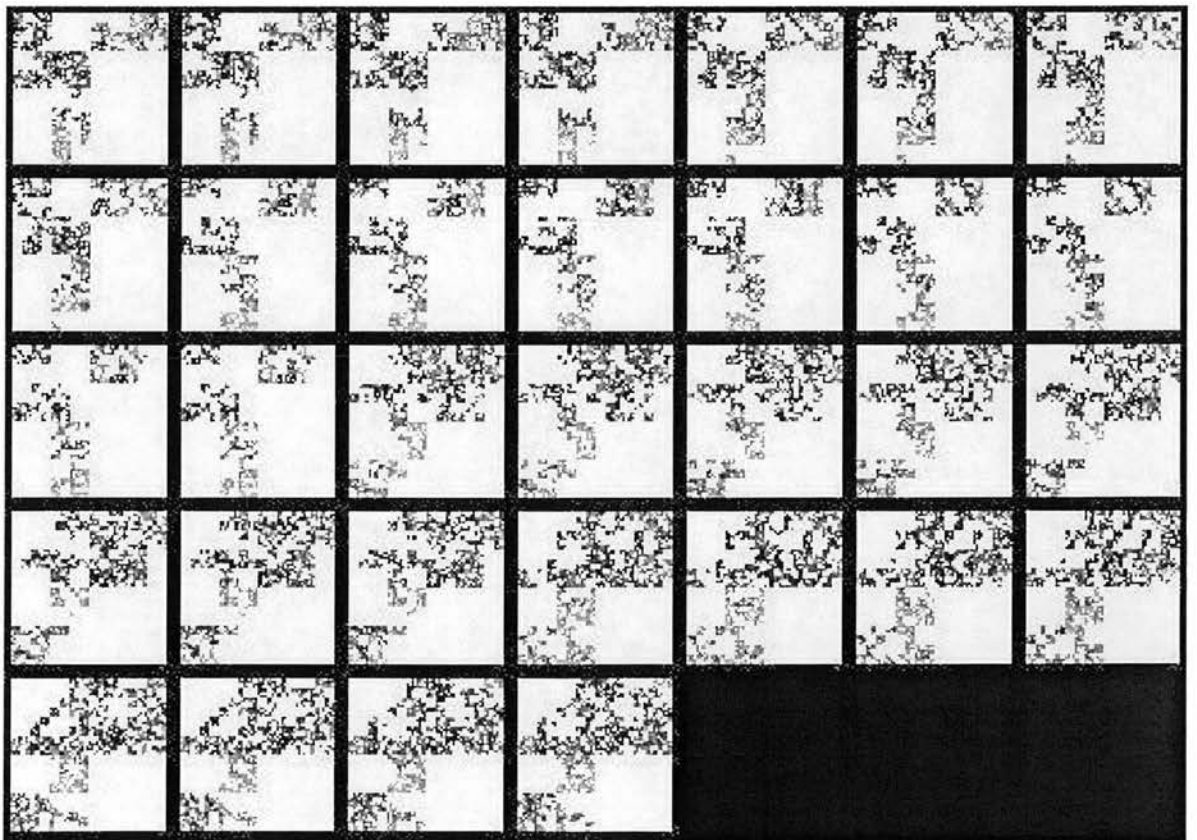
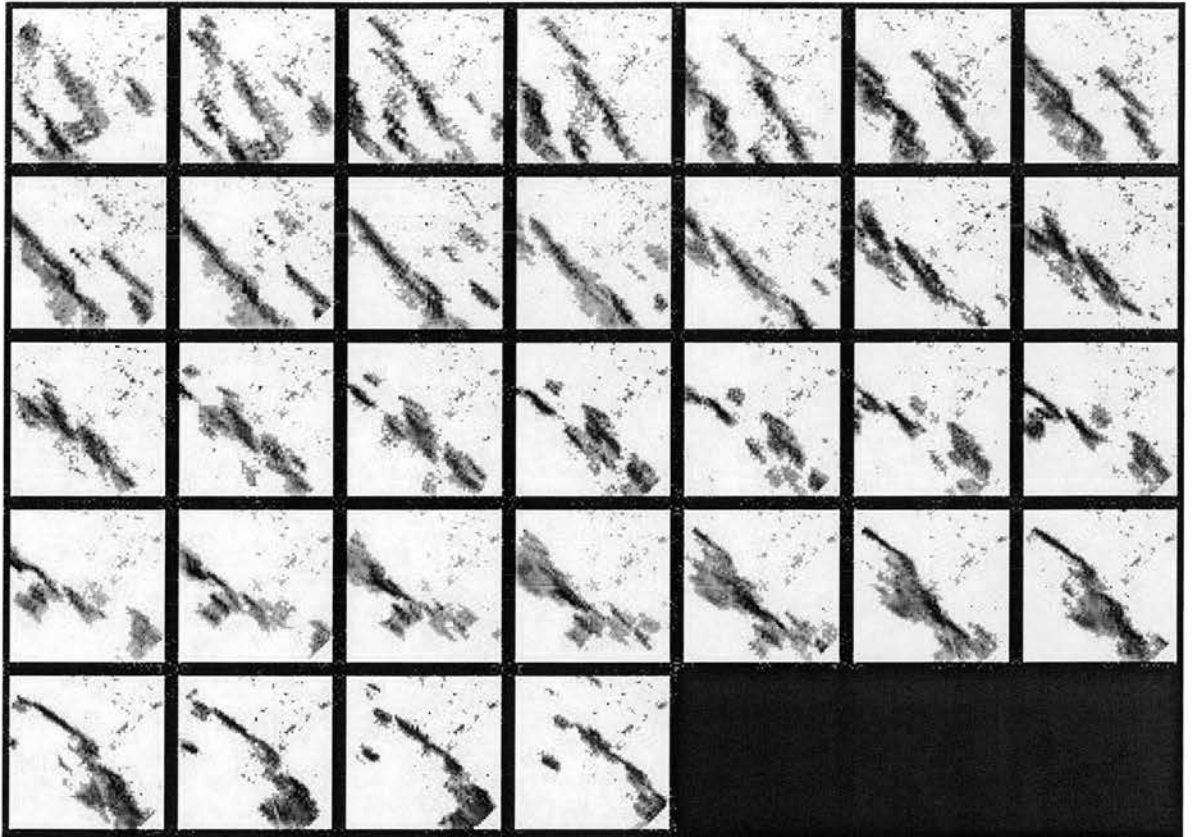


Figure 3.4: Series of 32 consecutive radar images (top) and 32 dependent random cascades (bottom)

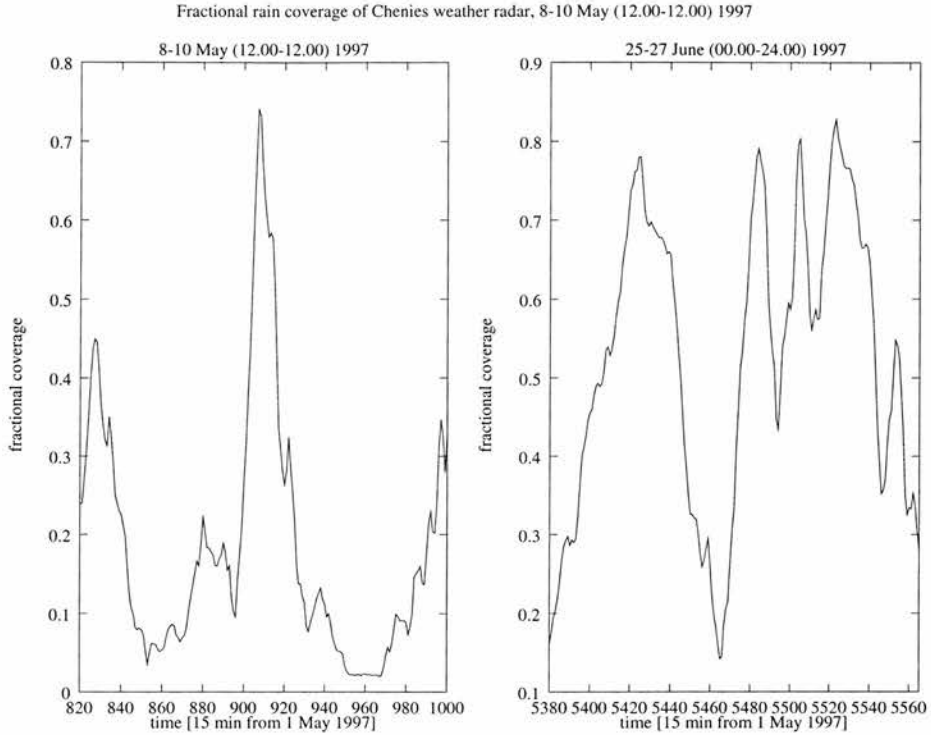


Figure 3.5: Fractional coverage, May and June storm

cascade are progressing at comparable rates.

Radar without memory Here the actual rain rates on the grid squares given by the radar provide the rainfall disaggregation. Instead of running independent simulations on each grid point, one time step is run on each pixel of the 64×64 under the same conditions apart from rainfall intensity, and then the canopy and other moisture stores are averaged out across the base square before the next time step begins. In this way memory is removed.

Radar with memory In this simulation the water store contents are calculated on each grid square independently. The rain rates are taken from the radar rate observed at that position. The resulting canopy and other moisture stores for each grid point are therefore remembered in the next time step. The average throughfall and canopy evaporation over the domain are calculated and recorded at each time step for the analysis later. Note that the fractional coverage, changes from one time step to another (fig 3.5).

3.4.2 Results

We observe the changes in the two water stores, canopy evaporation and throughfall, over the period 1 May - 30 June, using the rain representations described above. Particular attention was paid to two 48-hour rainy periods: 12:00 on 9 May to 12:00 on 11 May, and 24:00 on 26 June to 00:00 on 28 June.

Model outputs

In a) and b) of figures 3.6 and 3.7 the results of the simulations using the *radar with memory* and *radar without memory* distributions are presented for the two storms in May and June. In figures 3.6 and 3.7 c) and d) the throughfall and the canopy evaporation

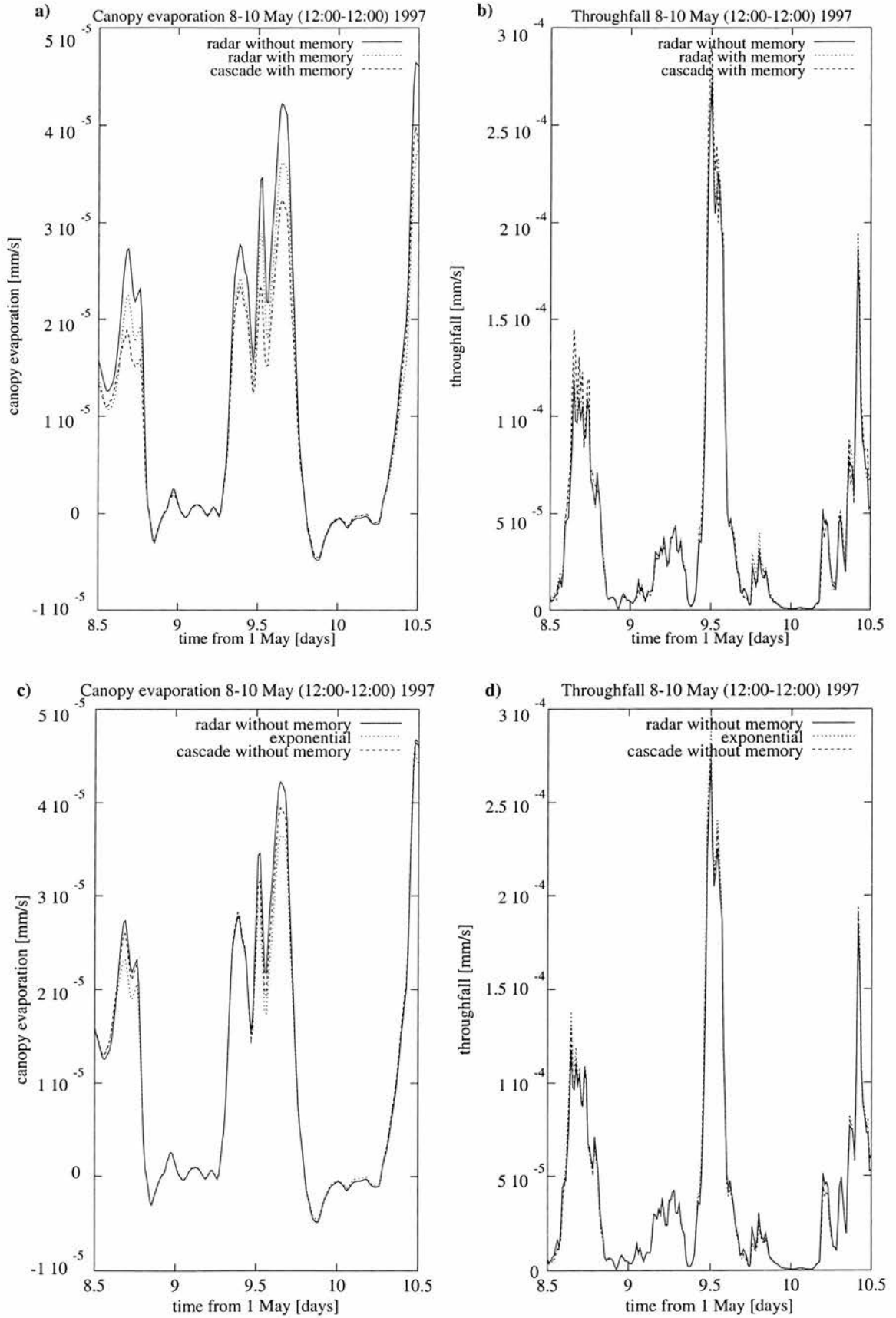


Figure 3.6: Throughfall and canopy evaporation results for the May storm

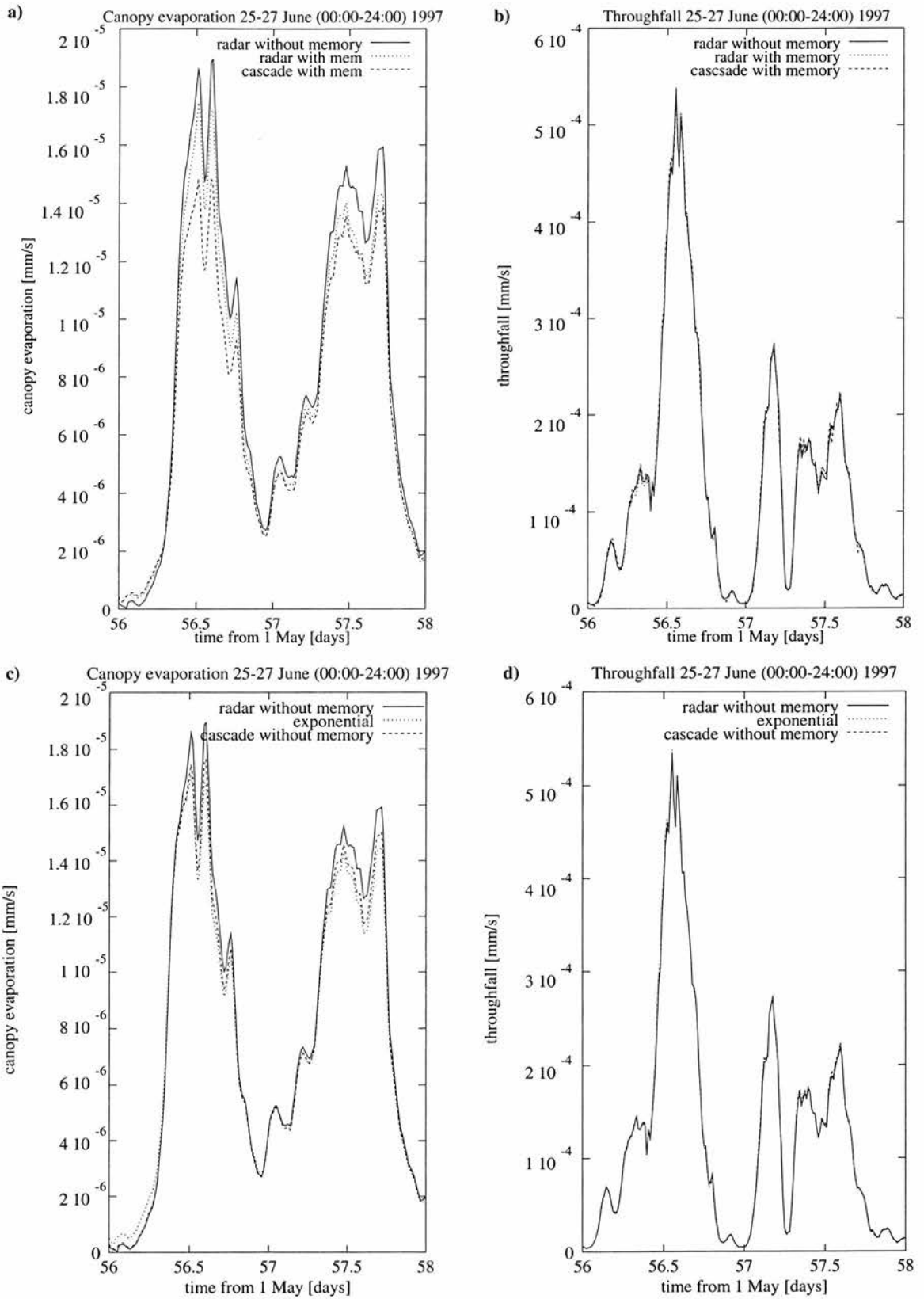


Figure 3.7: Throughfall and canopy evaporation results for the June storm

	Throughfall	Canopy evaporation
Flat	176.36	43.64
Exponential	178.73	41.26
Cascade without memory	181.51	38.51
Cascade with memory	188.98	31.15
Radar without memory	181.94	38.07
Radar with memory	190.26	29.94

Table 3.4: Total throughfall and total canopy evaporation over simulated period (all in kg/m²)

X_i, Y_i	$\sum X_i - \sum Y_i$	$\frac{\sum X_i - \sum Y_i}{\sum X_i} \cdot 100$
Radar no memory, Cascade no memory	0.44	0.24%
Radar no memory, Exponential	3.21	1.77%
Radar no memory, Flat	5.58	3.07%
Radar with memory, Radar no memory	8.31	4.37%
Radar with memory, Cascade with memory	1.28	0.67%
Radar with memory, Cascade no memory	8.75	4.60%
Radar with memory, Exponential	11.53	6.06%
Radar with memory, Flat	13.90	7.30%

Table 3.5: Comparison of throughfall results (in kg/m²)

resulting from a *cascade without memory* and an *exponential* distribution are compared. For the *cascade with* and *without memory* the results were found to vary little between different realisations; the values presented here are averages over 20 simulations.

Analysis

The total throughfall and the total canopy evaporation over the simulated period are shown in table 3.4. These values and the corresponding percentage differences are compared in tables 3.5 and 3.6. In these tables X_i and Y_i represent the throughfall / evaporation in each time step for the first and second representation named.

We postulate that the most realistic rainfall representation is the *radar with memory* simulation. As the *cascade without memory*, the *flat* and the *parametrical/exponential* approaches do not have any spatial memory, results from these simulations are not expected to be closer to *radar with memory* than the *radar without memory* simulation. Only the

X_i, Y_i	$\sum X_i - \sum Y_i$	$\frac{\sum X_i - \sum Y_i}{\sum X_i} \cdot 100$
Radar no memory, Cascade no memory	-0.44	-1.15%
Radar no memory, Exponential	-3.19	-8.38%
Radar no memory, Flat	-5.57	-14.62%
Radar with memory, Radar no memory	-8.13	-27.17%
Radar with memory, Cascade with memory	-1.21	-4.03%
Radar with memory, Cascade no memory	-8.57	-28.64%
Radar with memory, Exponential	-11.32	-37.82%
Radar with memory, Flat	-13.70	-45.76%

Table 3.6: Comparison of canopy evaporation results (all in kg/m²)

simulation using dependent cascades and memory could be expected to be comparable with the *radar with memory* simulation.

From tables 3.5 and 3.6 it can be seen that the differences between the consecutive simulations in total throughfall and total canopy evaporation are almost identical in value. The percentage changes are greater for the canopy evaporation because the absolute values of this variable are smaller.

Different components of the water balance equations may be affected to differing extents according to the rainfall distribution scheme selected, as seen in figures 3.6 and 3.7 comparing canopy evaporation and throughfall.

It can be seen from the graphs that the effect on the water balance of different rainfall distribution schemes is greatest when the rainfall intensity is high. Note that the scales on the ordinates in the evaporation and throughfall graphs differ by one order of magnitude.

Performance of cascade without memory The total throughfall and the total canopy evaporation of the *cascade without memory* simulation are almost identical with the values from the *radar without memory* simulation, which was chosen as the reference representation. The percentage difference for total throughfall and canopy evaporation when comparing *radar without memory* and *exponential* are roughly seven times those when comparing *radar without memory* and *cascade without memory*. This result is more significant for canopy evaporation as the percentage difference is reduced from -8.38% to -1.15% , whereas for throughfall the reduction is from 1.77% , which is already low, to 0.24% .

This indicates that the *cascade without memory* representation is more realistic than the exponential distribution.

Performance of cascade with memory By using dependent cascades and spatial memory, total throughfall and canopy evaporation results are close to the *radar with memory* simulations, when compared to *exponential*. For evaporation the percentage difference between *radar with memory* and *exponential* is seven times greater than between *radar with memory* and *cascade with memory*. That is a reduction from -37.82% to -4.03% . For throughfall the reduction in percentage differences is a factor of nine, from 6.06% to 0.67% .

Introducing dependent cascades and memory, results in long term water balance totals that are very close to the reference values.

Computational considerations By implementing any of these improvements of rainfall representations in GCM applications the computational effort will be significantly increased.

By disaggregating the rainfall information in a cascade the water balance equations have to be calculated for all subgrids in one time step and then all the water balance parameters have to be averaged. This results in a longer computation time, increased by a factor 64^2 in our case, and a slightly increased memory consumption.

By introducing spatial memory the simulation runs on every subgrid independently. If working with dependent cascades the memory consumption increases drastically, because the disaggregated data has to be generated and stored before the simulation can be started on each subgrid. The required computer memory by this disaggregation is increased by $timesteps \times 64^2$ elements, the increase of the computing time is a factor 64^2 again.

3.4.3 Conclusion

Using *cascade without memory* the water balance parameters are found to be much closer to the ones from *radar without memory* than the parameters calculated using the *exponential* scheme. This is particularly significant for the evaporation.

The same is true for the schemes using spatial memory. The differences here are more significant as the percentage changes are greater.

Further research could investigate the role of the cascade parameters in simulating rainfall. Ultimately it would be desirable to implement such an optimised land surface scheme online in an atmospheric model. This would show the effects of disaggregation on a system with a more realistic feedback between the different layers of the model and would enable comparison with field data.

Chapter 4

Selection of parameters for the random cascade process

4.1 Multifractal random cascades and rainfall distribution

Random cascade processes have been used very widely to simulate temporal and spatial rainfall distributions in both theoretical and practical work. The theoretical foundation for using random cascades to model rainfall was outlined in section 1.4.1, and experimental evidence, at least for the multifractality of rainfall fields, was indicated in section 1.4.2. In chapter 3 one particular novel application of this, the use of random cascades for rainfall disaggregation in the water balance component of a GCM, was described.

The usual approach in simulating the multifractality of rainfall is to use an appropriate random cascade model, in most cases a binary random cascade model, see section 1.4. There has been little discussion in the literature on the influence of the type of rainfall on multifractal features (such as auxiliary function or multifractal spectrum) or on the selection methods of cascade parameters to preserve these features.

A natural approach is to seek a random cascade with key multifractal features close to those of the distribution to be simulated. Thus, we need methods of finding parameters for random cascades with certain multifractal features prescribed. For practical purposes such methods need to be simple, with a small number of parameters to be determined, computationally convenient to implement and yet that give an auxiliary function or multifractal spectrum close to that of a given or observed distribution. As remarked in section 1.4.3, for hydrological purposes it is more important for simulations to replicate multifractal features for positive q than for negative q which corresponds to very sparse rainfall areas.

In section 4.2, we discuss the problem of utilising random cascades with discrete probability distributions for simulations. We present some simple schemes that give random cascades with specific multifractal features. We test these schemes in section 4.2.4.

In the literature, particularly that on rainfall distributions, there is often an implicit assumption that random cascades provide a good class of distributions for simulating observed multifractality. In section 4.3 we question this assumption. In particular we show that there are significant restrictions on the auxiliary function $\beta(q)$ or on the multifractal spectrum $f(\alpha)$ which may be approximated by binary random cascades. Thus, binary random cascades may be less appropriate than previously suggested as a canonical model for observed multifractals.

4.2 The choice of the cascade probability distribution

As in section 1.2.1 we generate a random cascade process by defining the subdivision number $N \geq 2$, the branching number $m = N^d$ and by repeatedly subdividing the d -dimensional unit cube $C_\emptyset = [0, 1]^d$ into m closed sub-cubes. We recall that the cubes are coded such that the k -th level cube C_{i_1, \dots, i_k} consists of the union of the $(k+1)$ -th level cubes $C_{i_1, \dots, i_k, 1}, \dots, C_{i_1, \dots, i_k, m}$. We construct a measure μ on C_0 by specifying a random variable vector $\{W_1, \dots, W_m\}$ which defines the ratios between the masses of the cubes and their sub-cubes in a statistically self-similar way, see section 1.2.2.

Recall that, conditional on the non-extinction of the random cascade, the multifractal auxiliary function is given by

$$\beta(q) = \frac{\log \mathbb{E}(\sum_{i=1}^m W_i^q)}{\log N}, \quad (4.1)$$

almost surely, see (1.39).

Ideally we would like to find probability distributions for the W_i that give a random measure with an almost sure multifractal spectrum that replicates a given (i.e. observed) spectrum.

For convenience we use independent identical probability distributions on each sub-square, that is W_1, \dots, W_m are identically and independently distributed, with the distribution of a random variable W , say. Thus from (4.1),

$$\beta(q) = \frac{\log(m\mathbb{E}(W^q))}{\log N} = \frac{\log(m \int h(t)t^q dt)}{\log N}, \quad (4.2)$$

if W has the probability distribution function $h(t)$. In principle $h(t)$ can be found from β using the Mellin transformation \mathcal{M} . Substituting $r = q + 1$ gives

$$\frac{1}{m} N^{\beta(r-1)} = \int_0^\infty h(t)t^{r-1} dt = (\mathcal{M}h)(r). \quad (4.3)$$

Thus inverting, we have formally

$$h(t) = (\mathcal{M}^{-1}(\frac{1}{m} N^{\beta(r-1)}))(t). \quad (4.4)$$

Unfortunately, there is no guarantee that the resulting $h(t) \geq 0$, corresponding to a probability distribution function. Instead we use an approach that is computationally simple, and which leads to a random measure with an almost sure multifractal spectrum that reflects some of the main features of the given spectrum.

For computational and mathematical convenience we adopt a random cascade with discrete weights, see section 1.2.4, so that W is a discrete random variable. Letting $0 = a_0 < a_1 < \dots < a_k$ be numbers and p_0, \dots, p_k be probabilities, so $p_0 \geq 0, p_1, p_2, \dots, p_k > 0$ and

$$\sum_{i=0}^k p_i = 1, \quad (4.5)$$

we define W by

$$\Pr(W = a_i) = p_i. \quad (4.6)$$

The expected number of sub-cubes at the k -th level of construction is given by (1.46). If $p_0 > 0$, there is positive probability of total extinction. In the practical realisation of

random cascades, the disaggregation step in which extinction occurs is repeated. This is valid because the cascade will have the predicted multifractal properties despite the intervention.

With W given by (4.6) we recall from section 1.2.4 that the multifractal auxiliary function is

$$\beta(q) = \frac{\log(m \sum_{i=0}^k p_i a_i^q)}{\log N}. \quad (4.7)$$

The multifractal spectrum is then given parametrically by (1.19) and (1.20):

$$\alpha(q) = -\frac{d\beta(q)}{dq} = \frac{-\sum_{i=0}^k p_i a_i^q \log a_i}{\log N \sum_{i=0}^k p_i a_i^q} \quad (4.8)$$

$$f(\alpha(q)) = \beta(q) + q\alpha(q). \quad (4.9)$$

We can identify some special points of the multifractal spectrum and the multifractal auxiliary function (sect 1.1.2), see figure 4.1. Amongst the key values of β are those when

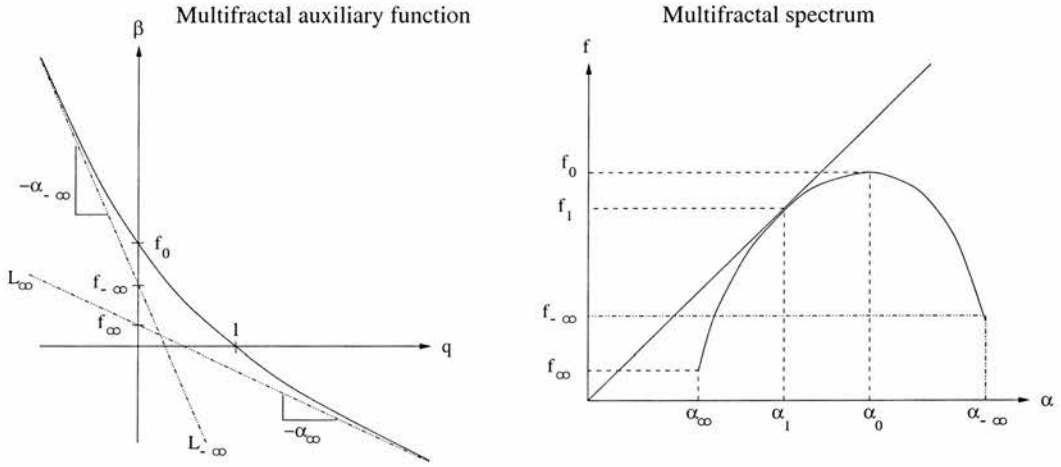


Figure 4.1: General form of $f(\alpha)$ and $\beta(q)$

$q = 0$, $q = 1$ and when q approaches $\pm\infty$. For convenience, regarding α and f as functions of q , we write

$$\alpha_0 = \alpha(0) \quad (4.10a)$$

$$\alpha_1 = \alpha(1) \quad (4.10b)$$

$$\alpha_{-\infty} = \lim_{q \rightarrow -\infty} \alpha(q) = -\lim_{q \rightarrow -\infty} \frac{\beta(q)}{q} \quad (4.10c)$$

$$\alpha_{\infty} = \lim_{q \rightarrow \infty} \alpha(q) = -\lim_{q \rightarrow \infty} \frac{\beta(q)}{q} \quad (4.10d)$$

$$f_0 = f(0) \quad (4.10e)$$

$$f_1 = f(1) \quad (4.10f)$$

$$f_{-\infty} = \lim_{q \rightarrow -\infty} f(q) = -\lim_{q \rightarrow -\infty} (\beta(q) - q \frac{d\beta}{dq}(q)) \quad (4.10g)$$

$$f_{\infty} = \lim_{q \rightarrow \infty} f(q) = -\lim_{q \rightarrow \infty} (\beta(q) - q \frac{d\beta}{dq}(q)), \quad (4.10h)$$

see (1.16).

We aim to find random cascade parameters resulting in a multifractal distribution similar to an observed one. Therefore we examine conditions on the a_i and p_i that ensure β (or equivalently f) satisfies key properties of the observed multifractal functions in the hope that such a random cascade provides a good approximation in general.

Condition at $q = 0$: For the almost sure multifractal spectrum of the random cascade to take prescribed values α_0 and f_0 we require

$$\alpha_0 = \alpha(0) = \frac{-\sum_{i=1}^k p_i \log a_i}{(1 - p_0) \log N} \quad (4.11)$$

$$f_0 = \beta(0) = \frac{\log(m(\sum_{i=1}^k p_i))}{\log N} \quad (4.12)$$

$$= \frac{\log(m(1 - p_0))}{\log N}. \quad (4.13)$$

Condition at $q = 1$: For the almost sure multifractal spectrum of the random cascade to take prescribed values α_1 and f_1 we require

$$\alpha_1 = \alpha(1) = f_1 = f(1) = -m \sum_{i=1}^k p_i a_i \log a_i. \quad (4.14)$$

Condition as $q \rightarrow \infty$: For the almost sure multifractal spectrum of the random cascade to have a prescribed asymptote as $q \rightarrow \infty$, we note from (4.7) that for large positive q ,

$$\beta(q) = \frac{\log(mp_k a_k^q (1 + o(1)))}{\log N} \quad (4.15)$$

$$= \frac{\log mp_k + q \log a_k + \log(1 + o(1))}{\log N}. \quad (4.16)$$

Letting $q \rightarrow \infty$ we get the asymptote

$$\beta(q) = \frac{q \log a_k + \log mp_k}{\log N} \quad (\text{as } q \rightarrow \infty). \quad (4.17)$$

Comparing with (4.10),

$$\alpha_\infty = -\frac{\log a_k}{\log N} \quad f_\infty = \frac{\log mp_k}{\log N}. \quad (4.18)$$

Condition as $q \rightarrow -\infty$: Similarly for $q \rightarrow -\infty$ we get the asymptote

$$\beta(q) = \frac{q \log a_1 + \log mp_1}{\log N} \quad (\text{as } q \rightarrow -\infty), \quad (4.19)$$

so that

$$\alpha_{-\infty} = -\frac{\log a_1}{\log N} \quad f_{-\infty} = \frac{\log mp_1}{\log N}. \quad (4.20)$$

Other conditions: Clearly the p_i must satisfy

$$p_0 \geq 0, \quad p_1, \dots, p_k > 0, \quad \sum_{i=0}^k p_i = 1. \quad (4.21)$$

A further restriction on the choice of the a_i and p_i is

$$m \sum_{i=0}^k a_i p_i = 1, \quad (4.22)$$

reflecting that mass is conserved on average, see (1.33).

The above conditions can be achieved very easily for $q = 0$ (at least for f_0), $q \rightarrow \infty$ and $q \rightarrow -\infty$ by appropriate selection of a_0, a_1, a_k and p_0, p_1, p_k . Thus with $a_0 = 0$ we choose p_0 so that (4.13) is satisfied and a_k, p_k, a_1 and p_1 to satisfy (4.18) and (4.20). We are then in principle free to choose non-negative p_2, \dots, p_{k-1} and a_2, \dots, a_{k-1} subject to the restrictions (4.21) and (4.22). Note that conditions $0 < a_1 < \dots < a_k < 1$ and $0 < p_0, \dots, p_k < 1$ result in the following constraints on the prescribed values

$$\begin{aligned} f_{-\infty}, f_{\infty} < f_0 \leq d \\ 0 < \alpha_{-\infty} < \alpha_{\infty}, \end{aligned} \quad (4.23)$$

and other restrictions will become apparent.

4.2.1 A scheme with $k = 3$

We first present a simple scheme to give a random cascade process with discrete weights of the form (4.6) with $k = 3$, that has certain required features.

i	a_i	p_i
0	0	$1 - \frac{N^{f_0}}{m}$
1	$N^{-\alpha_{-\infty}}$	$\frac{N^{f_{-\infty}}}{m}$
2	$\frac{m^{-1} - a_1 p_1 - a_3 p_3}{p_2}$	$1 - p_0 - p_1 - p_3$
3	$N^{-\alpha_{\infty}}$	$\frac{N^{f_{\infty}}}{m}$

Table 4.1: Choice of a_i and p_i for $k = 3$

This scheme, with values given in table 4.1, gives a random cascade with almost sure multifractal spectrum (subject to non-extinction) taking prescribed values of $f_0, \alpha_{-\infty}, f_{-\infty}, \alpha_{\infty}$ and f_{∞} . Here a_0, a_1, a_3 and p_0, p_1, p_3 are determined by (4.13), (4.18) and (4.20). We are then left with setting a_2 and p_2 to ensure (4.21) and (4.22) hold.

In addition to the conditions on the prescribed values given by (4.23) we need to ensure that $1 - p_0 - p_1 - p_3 > 0$, thus

$$N^{f_{-\infty}} + N^{f_{\infty}} \leq N^{f_0}. \quad (4.24)$$

This suggests that only multifractal spectra that are not too flat can be approximated in this way. Furthermore, we require that

$$N^{-\alpha_{-\infty}} < \frac{m^{-1} - a_1 p_1 - a_3 p_3}{p_2} < N^{-\alpha_{\infty}}, \quad (4.25)$$

hence

$$1 + N^{f_{-\infty}}(N^{-\alpha_{-\infty}} - N^{-\alpha_{\infty}}) < N^{-\alpha_{-\infty}} N^{f_0} < 1 + N^{f_{\infty}}(N^{-\alpha_{-\infty}} - N^{-\alpha_{\infty}}) \quad (4.26)$$

These conditions did not appear to impose major constrictions on examples of interest. This scheme has the considerable advantage of being computationally extremely easy, but has the particular disadvantage that α_0 is not prescribed.

4.2.2 A scheme with $k = 4$

Taking $k = 4$, and proceeding as in section 4.2.1, a_0, a_1, a_4 and p_0, p_1, p_4 are determined by $f_0, \alpha_{-\infty}, f_{-\infty}, \alpha_{\infty}$ and f_{∞} . There is in principle freedom of choice of a_2 and a_3 with

i	a_i	p_i
0	0	$1 - \frac{N^{f_0}}{m}$
1	$N^{-\alpha_{-\infty}}$	$\frac{N^{f_{-\infty}}}{m}$
2	a_2	$\frac{A_1 a_3 - A_2}{a_3 - a_2}$
3	a_3	$\frac{A_2 - A_1 a_2}{a_3 - a_2}$
4	$N^{-\alpha_{\infty}}$	$\frac{N^{f_{\infty}}}{m}$

Table 4.2: Choice of a_i and p_i for $k = 4$

$a_1 < a_2, a_3 < a_4$, but then p_2 and p_3 are determined as in (4.21) and (4.22), as indicated in table 4.2, where

$$\begin{aligned} A_1 &= p_2 + p_3 = 1 - (p_0 + p_1 + p_4) \\ A_2 &= a_2 p_2 + a_3 p_3 = \frac{1}{m} - (a_1 p_1 + a_4 p_4). \end{aligned} \quad (4.27)$$

Of course, we are restricted by the conditions $0 < p_2, p_3 < 1$, which require $a_1 < a_2 < A_2/A_1 < a_3 < a_4$. In principle, we can select a_2 and a_3 to capture two other multifractal features. It is natural to try to choose them to get desired values for α_0 given by (4.11) and α_1 given by (4.14). However, in particular cases examined, to achieve α_0 and α_1 simultaneously, the only solution of (4.11) and (4.14) required $a_2 = a_3$, which gives inadmissible values for p_2, p_3 .

When utilising this scheme it was found best to concentrate on achieving a prescribed value of α_0 by fixing a_2 with $a_1 < a_2 < A_2/A_1$ and calculating a_3 from (4.11).

4.2.3 A scheme with a general k

In principle, one might look for a generalisation of this method to schemes with arbitrary k . The most natural choice for $0 = a_0 < a_1 < \dots < a_k$ would be arithmetically or geometrically spaced. The values of a_1 and a_k are determined by $\alpha_{-\infty}$ and α_{∞} . As in the previous schemes, the values of p_0, p_1 and p_k are determined by $f_0, f_{-\infty}$ and f_{∞} . The values of the p_2, \dots, p_{k-1} have to be chosen to satisfy (4.21) and (4.22) and also so that $\beta(q)$ given by (4.7) approximates the desired function over a range of q . In practice this proved to be awkward, because fitting the parameters usually resulted in negative probabilities. In section 4.3 we see that such difficulties are unavoidable in many instances.

4.2.4 Results of trials

The schemes above were tested computationally to construct binomial random cascades ($N = 2, m = 4$) with multifractal features replicating those of specific and empirical measures.

Trinomial random cascade measure

For a first test, we use a binomial cascade to simulate the multifractal functions of a trinomial random cascade with discrete weights, constructed as in section 1.2.4 with $N = 3$ and $m = 9$ and the weights given by

$p_0 = 0.087$	$p_1 = 0.225$	$p_2 = 0.473$	$p_3 = 0.215$
$a_0 = 0.000$	$a_1 = 0.090$	$a_2 = 0.119$	$a_3 = 0.160$

The multifractal auxiliary function is given by (4.7) and in particular in this case

$f_{\infty} = 0.647$	$f_0 = 1.917$	$f_{-\infty} = 0.693$
$\alpha_{\infty} = 1.670$	$\alpha_0 = 1.938$	$\alpha_{-\infty} = 2.190$

Applying the “ $k = 3$ ” scheme gives the following parameters for a binomial random cascade process, which we expect to have similar multifractal properties, at least near $q = 0, q \rightarrow -\infty$ and $q \rightarrow \infty$:

$p_0 = 0.056$	$p_1 = 0.404$	$p_2 = 0.148$	$p_3 = 0.391$
$a_0 = 0.000$	$a_1 = 0.219$	$a_2 = 0.259$	$a_3 = 0.314$

and by applying the “ $k = 4$ ” scheme we obtain the following parameters:

$p_0 = 0.056$	$p_1 = 0.404$	$p_2 = 0.072$	$p_3 = 0.075$	$p_4 = 0.391$
$a_0 = 0.000$	$a_1 = 0.219$	$a_2 = 0.239$	$a_3 = 0.278$	$a_4 = 0.314$

In the “ $k = 4$ ” scheme the parameter a_2 was chosen to be the mean value of a_1 and $A_2/A_1 = 0.259$, see (4.27), in order to achieve α_0 . In figure 4.2 and 4.3 the theoretical multifractal functions of the trinomial random cascade given by (4.7) and the theoretical multifractal functions of the binomial random cascade process with parameters given by the two schemes are shown. Not only does the binomial random cascade simulation given by the “ $k = 3$ ” scheme fit to the desired spectrum at $f_0, \alpha_{-\infty}$ and α_{∞} , as it must, but it gives a very close approximation over the entire range of q . In this instance, the simulation gives a close fit at α_0 , so the “ $k = 4$ ” scheme would not be expected to give much improvement, as is indeed the case.

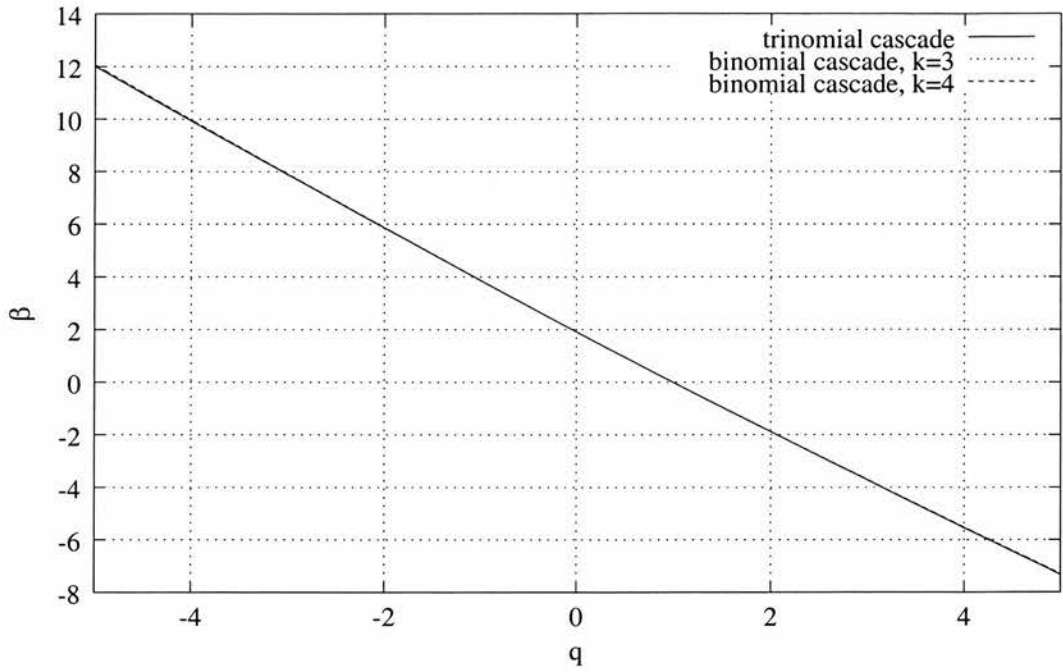


Figure 4.2: $\beta(q)$ of a trinomial cascade, and a binary cascade measure constructed by the “ $k = 3$ ” and the “ $k = 4$ ” schemes to replicate its multifractal properties

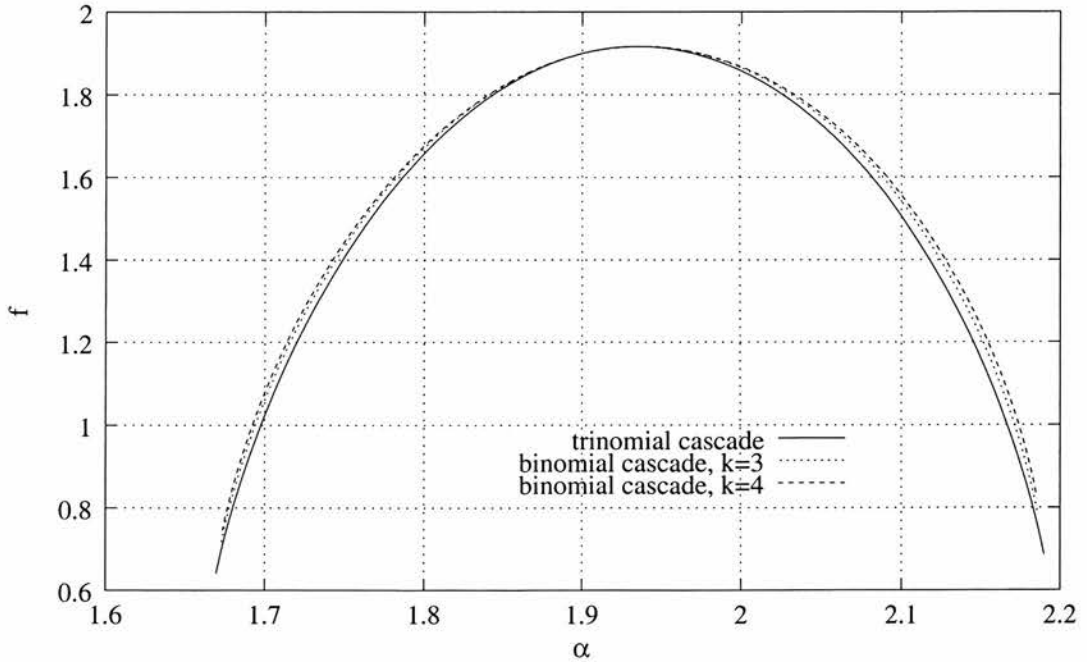


Figure 4.3: $f(\alpha)$ of a trinomial cascade, and a binary cascade measure constructed by the “ $k = 3$ ” and the “ $k = 4$ ” schemes to replicate its multifractal properties

Self-affine measures on generalised Sierpiński triangle

The second mathematical measures we considered were two (non-random) self-affine multinomial measures supported by a generalised Sierpiński triangle, see chapter 2. The multifractal auxiliary function of the measures is given by theorem 2.3. The parameters characterising the ratios of the side intersections, see (2.2), were in both cases $a = 0.75$, $b = 0.4$, see figure 2.3. The first measure was generated with the weights 0.3, 0.4, 0.3. It leads to a multifractal auxiliary function with

$f_\infty = 0.000$	$f_0 = 1.719$	$f_{-\infty} = 0.000$
$\alpha_\infty = 0.868$	$\alpha_0 = 1.988$	$\alpha_{-\infty} = 2.898$

By applying the “ $k = 3$ ” scheme we obtain the following parameters for a binomial random cascade process, which we expect to have similar multifractal properties for the measure on the Sierpiński triangle:

$p_0 = 0.177$	$p_1 = 0.250$	$p_2 = 0.323$	$p_3 = 0.250$
$a_0 = 0.000$	$a_1 = 0.134$	$a_2 = 0.246$	$a_3 = 0.548$

and by applying the “ $k = 4$ ” scheme we obtain the following parameters:

$p_0 = 0.177$	$p_1 = 0.250$	$p_2 = 0.040$	$p_3 = 0.283$	$p_4 = 0.250$
$a_0 = 0.000$	$a_1 = 0.134$	$a_2 = 0.190$	$a_3 = 0.254$	$a_4 = 0.548$

In the “ $k = 4$ ” scheme the parameter a_2 was chosen to be the mean value of a_1 and $A_2/A_1 = 0.246$, see (4.27), in order to achieve α_0 . It is not possible to get a fit both in α_0 and α_1 , unless $a_2 = a_3$, which is not allowable on consideration of p_2 and p_3 .

The other Sierpiński measure was created using the weights 0.25, 0.35, 0.4. This results in a multifractal auxiliary function with

$f_\infty = 0.000$	$f_0 = 1.719$	$f_{-\infty} = 0.452$
$\alpha_\infty = 1.000$	$\alpha_0 = 1.850$	$\alpha_{-\infty} = 2.230$

and by applying the “ $k = 3$ ” scheme we obtain these values for the random cascade process:

$p_0 = 0.177$	$p_1 = 0.342$	$p_2 = 0.231$	$p_3 = 0.250$
$a_0 = 0.000$	$a_1 = 0.213$	$a_2 = 0.226$	$a_3 = 0.500$

Applying the “ $k = 4$ ” scheme results in $a_2 = a_3$ as only solution, caused by $A_2/A_1 = 0.2256$ being close to a_1 .

In figure 4.4 the auxiliary functions of the two measures on the Sierpiński triangle and the simulated measures are displayed. In figure 4.5 the multifractal spectrum of these measures and the simulated cascade are displayed. In the case of the first measure on the Sierpiński triangle, with two identical weights, the random cascade simulation gives a remarkably close fit to the desired multifractal functions. In the case of the second measure, with three different weights, the parameters a_1 and a_2 turn out to be very close to each other. This leads to a slow convergence of $\beta(q)$ to its asymptote as $q \rightarrow -\infty$.

Spatial rainfall

We used a binomial random cascade to simulate an empirical multifractal spectrum given by spatial rainfall data from the GCIP/EOP project covering the Mississippi area in the USA, taken on the 28/04/1997. The multifractal spectrum was calculated using the enlarged box-counting method, see section 1.3.3. The multifractal auxiliary function is shown in figure 4.6 and the multifractal spectrum in figure 4.7. We can read the following values off the graphs:

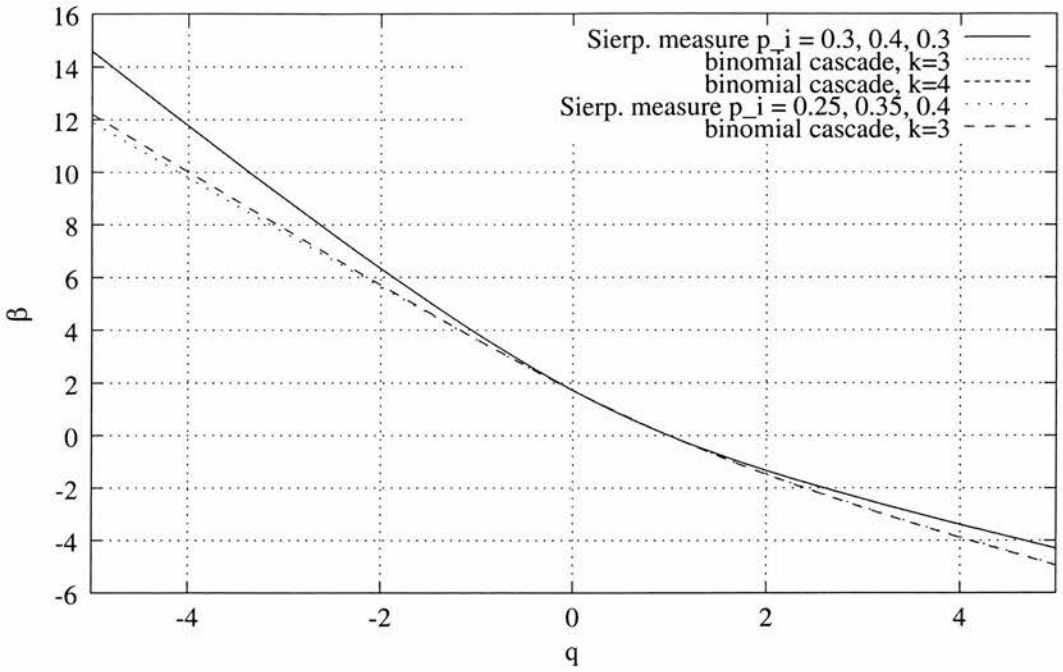


Figure 4.4: $\beta(q)$ of two multinomial measures on generalised Sierpiński triangles, and of the random cascade measures constructed by the “ $k = 3$ ” and the “ $k = 4$ ” schemes to replicate their multifractal properties

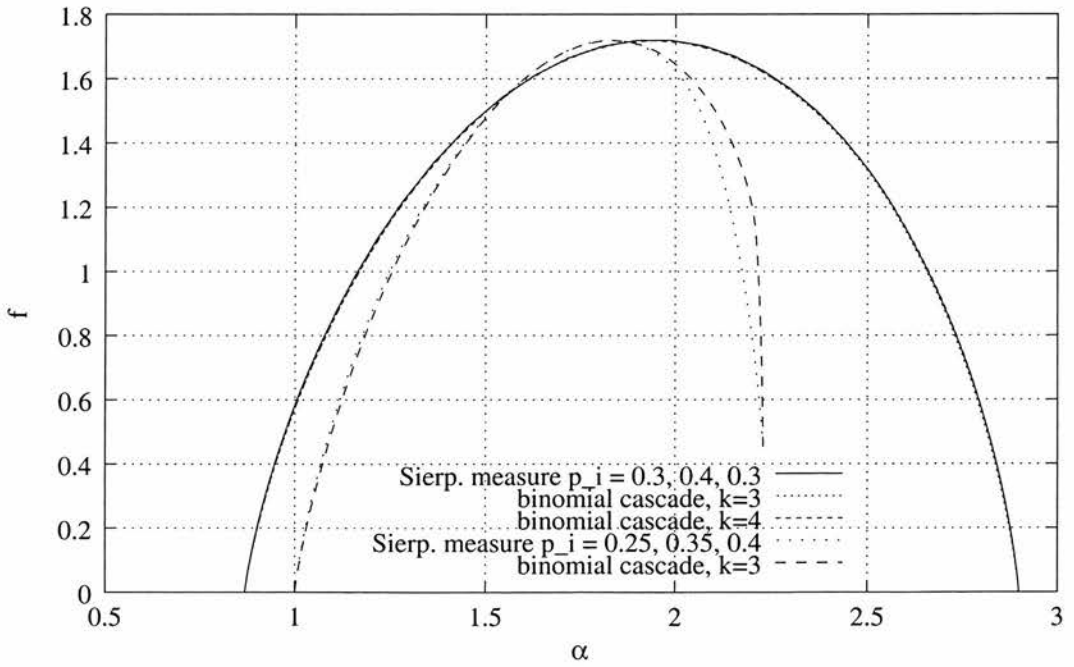


Figure 4.5: $f(\alpha)$ of two multinomial measures on generalised Sierpiński triangles, and of the random cascade measures constructed by the “ $k = 3$ ” and the “ $k = 4$ ” schemes to replicate their multifractal properties

$f_\infty = 0.209$	$f_0 = 1.513$	$f_{-\infty} = 0.204$
$\alpha_\infty = 1.097$	$\alpha_0 = 1.541$	$\alpha_{-\infty} = 2.346$

Applying the “ $k = 3$ ” scheme, gives the following parameters for a binomial random cascade, which we expect have similar multifractal properties:

$p_0 = 0.287$	$p_1 = 0.288$	$p_2 = 0.136$	$p_3 = 0.289$
$a_0 = 0.000$	$a_1 = 0.197$	$a_2 = 0.428$	$a_3 = 0.467$

Figure 4.7 shows:

- the empirical multifractal spectrum of the spatial rainfall distribution (using enlarged box-counting and Legendre transform formalism) and
- the theoretical multifractal spectrum of the random cascade process with parameters given by the “ $k = 3$ ” scheme.

In this case the random cascade simulation gives a reasonable fit to the desired spectrum, although there is a noticeable shift of α_0 , which is not retained by the “ $k = 3$ ” scheme. Attempts to use the $k = 4$ scheme gave common values for the a_i , and did not lead to a better fit.

Summary

These examples show that the schemes proposed are adequate to find random cascade parameters for replicating basic multifractal properties. The simple “ $k = 3$ ” scheme generally leads to positive p_i and enables us to generate random cascades achieving the multifractal spectrum at f_0 , $\alpha_{-\infty}$, $f_{-\infty}$, α_∞ and f_∞ . The “ $k = 4$ ” scheme additionally provides us with a method of achieving α_0 , but in practice is unsatisfactory, due to the lack of positivity of the p_i and the arbitrary choice of a_2 . Schemes with $k > 4$ have not been implemented.

4.3 Limitations of random cascades for representing multifractal processes

We have seen that in some cases it is possible to find a binary random cascade with auxiliary function β of multifractal spectrum $f(\alpha)$ close to given ones. Nevertheless, there are certain $\beta(q)$ or $f(\alpha)$ which are impossible to replicate by random cascades. In this section we give some inequalities that are necessary conditions for β to be the auxiliary function of a random cascade. Recall that we already have some restrictions (4.23) - (4.26) from section 4.2.1.

These restrictions bring into question the assumption that binary random cascades are appropriate for general modelling purposes. In section 1.4 we indicated the heuristic arguments for rainfall fields having the form of random cascades, but it follows from these conclusions that we cannot assume that we can find a binary random cascade with $\beta(q)$ or $f(\alpha)$ close to those observed.

First we obtain some inequalities satisfied by the β function (or more exactly by $N^{\beta(q)}$) of an N -ary random cascade. We then deduce that it is not possible for certain N -ary random cascades to have the same multifractal properties as certain N_1 -ary random cascades, where $N_1 > N$. In particular this concerns whether given $\alpha_\infty, \alpha_{-\infty}, f_0, f_\infty$ and $f_{-\infty}$ can be achieved.

We then develop further necessary conditions for a given $\beta(q)$ to be reproducible by an N -ary random cascade using moment considerations. These conditions can be applied to a

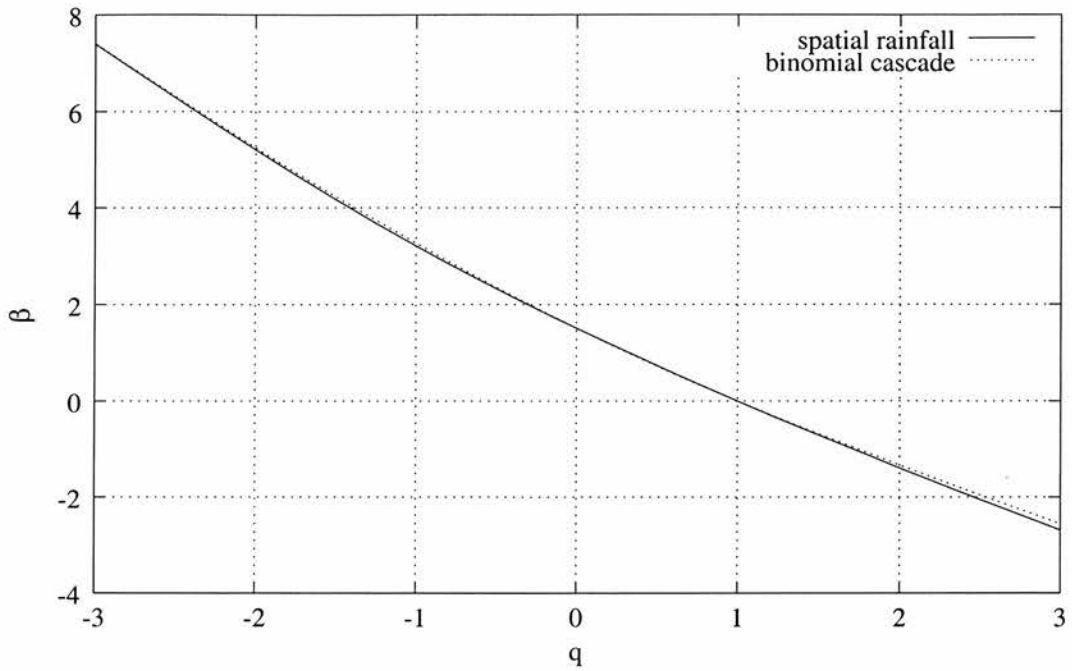


Figure 4.6: $\beta(q)$ of a spatial rainfall distribution, and a random cascade measure constructed by the “ $k = 3$ ” scheme to replicate its multifractal properties

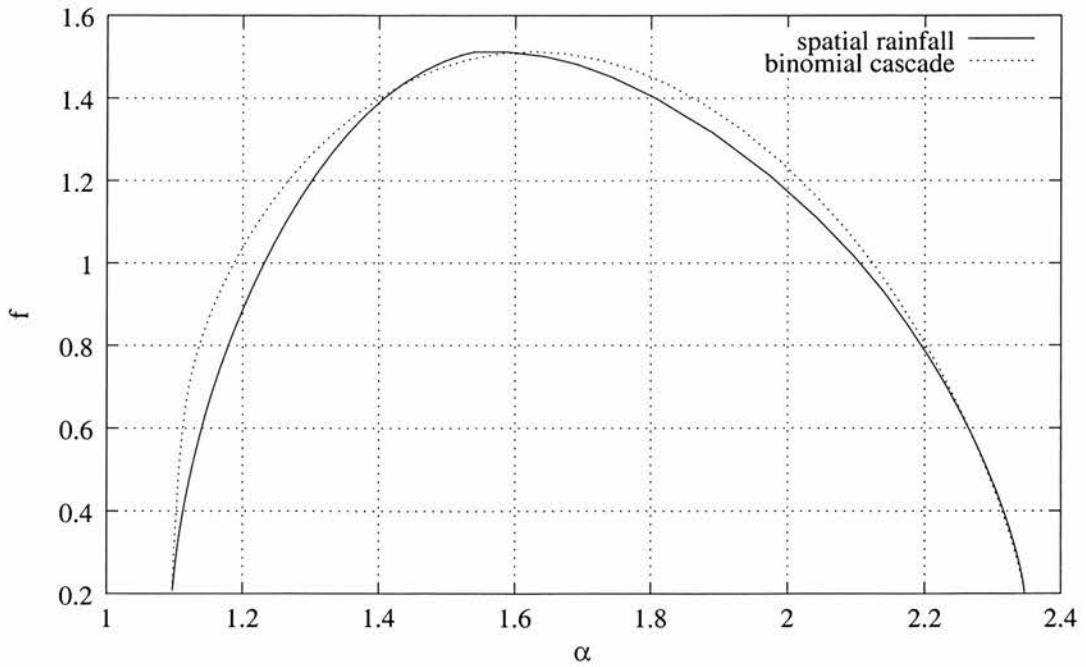


Figure 4.7: $f(\alpha)$ of a spatial rainfall distribution, and a random cascade measure constructed by the “ $k = 3$ ” scheme to replicate its multifractal properties

bounded range of q . We conclude that random cascade processes with a given subdivision number are not necessarily suitable for replicating certain observed multifractal spectra.

4.3.1 Inequalities satisfied by the auxiliary function of an N -ary random cascade

The following proposition gives restrictions on $\beta(q)$ attainable by an N -ary random cascade, in terms of the dimension of support and form of the asymptotes.

Proposition 4.1. *Let β be the almost sure auxiliary function (subject to non extinction) of a random cascade with subdivision number N , branching number $m = N^d$ on \mathbb{R}^d and discrete weights as in (4.6). Suppose that β has asymptotes of the form*

$$q \frac{\log a_\infty}{\log N} + \frac{\log p_\infty}{\log N} + d \text{ as } q \rightarrow \infty \quad (4.28)$$

and

$$q \frac{\log a_{-\infty}}{\log N} + \frac{\log p_{-\infty}}{\log N} + d \text{ as } q \rightarrow -\infty \quad (4.29)$$

for $0 < a_{-\infty} < a_\infty$ and $p_{-\infty}, p_\infty > 0$ and the almost sure dimension of the support, subject to non-extinction, is given by

$$\frac{\log(N^d(1 - p_s))}{\log N}. \quad (4.30)$$

Then $\beta(q)$ satisfies the inequality

$$p_\infty a_\infty^q + (1 - p_s - p_\infty) a_{-\infty}^q \leq N^{\beta(q)-d} \leq p_{-\infty} a_{-\infty}^q + (1 - p_s - p_{-\infty}) a_\infty^q \quad (4.31)$$

if $q > 0$ and

$$p_\infty a_\infty^q + (1 - p_s - p_\infty) a_{-\infty}^q \geq N^{\beta(q)-d} \geq p_{-\infty} a_{-\infty}^q + (1 - p_s - p_{-\infty}) a_\infty^q \quad (4.32)$$

if $q < 0$.

Proof. With the form of the random cascade process given by (4.7) we have $a_1 = a_{-\infty}$, $p_1 = p_{-\infty}$, $a_k = a_\infty$, $p_k = p_\infty$, $p_0 = p_s$, by comparison with (4.13), (4.17) and (4.19). Thus

$$N^{\beta(q)-d} = p_{-\infty} a_{-\infty}^q + \sum_{i=2}^{k-1} p_i a_i^q + p_\infty a_\infty^q. \quad (4.33)$$

Since $a_1 < a_2 < \dots < a_k$,

$$\begin{aligned} (1 - p_s - p_{-\infty} - p_\infty) a_1^q &= (p_2 + \dots + p_{k-1}) a_1^q \\ &\leq \sum_{i=2}^{k-1} p_i a_i^q \leq (p_2 + \dots + p_{k-1}) a_k^q = (1 - p_s - p_{-\infty} - p_\infty) a_\infty^q, \end{aligned} \quad (4.34)$$

if $q \geq 0$, giving (4.31). If $q \leq 0$ the inequalities are reversed, and we get (4.32). \square

As a corollary to this, we deduce that, in many cases, the auxiliary function of an N_1 -ary random cascade cannot be approximated by an N -ary random cascade if $N_1 > N$.

Corollary 4.2. *Let μ be the random cascade on \mathbb{R}^d with subdivision number N_1 and branching number $m_1 = N_1^d$, and with mass ratios $0 = b_0 < b_1 < \dots < b_k$ having probabilities $\lambda_0, \lambda_1, \dots, \lambda_k$ with $\lambda_i > 0$ for $i \geq 1$, with $\sum_{i=0}^k \lambda_i = 1$ and $m_1 \sum_{i=1}^k \lambda_i b_i = 1$. Thus the almost sure multifractal auxiliary function, conditional on non-extinction, is given by*

$$N_1^{\beta(q)-d} = \sum_{i=0}^k \lambda_i b_i^q, \quad (4.35)$$

see (4.7). Then it is not possible to approximate $\beta(q)$ by the auxiliary function of an N -ary random cascade process in the following cases:

- a) If $N_1 > N$, $k = 2$ and $\lambda_1, \lambda_2 > 0$.
- b) If $N_1 > N$, $k > 2$ and $\lambda_1^\gamma + \lambda_k^\gamma > (1 - \lambda_0)^\gamma$, where $\gamma = \log N / \log N_1$.

Further to a), given a random cascade with $N_1 = N^2$ and $k = 2$, if an N -ary random cascade process has the same values of $\beta(0)$, $\lim_{q \rightarrow -\infty} \beta(q)$ and $\lim_{q \rightarrow \infty} \beta(q)$ as the given cascade, then $\beta(q)$ differs from the auxiliary function of the given cascade for all other q .

Proof. a) Here $N_1^{\beta(q)-d} = \lambda_1 b_1^q + \lambda_2 b_2^q$ and the asymptotes are given by

$$q \frac{\log b_1}{\log N_1} + \frac{\log \lambda_1}{\log N_1} + d \text{ as } q \rightarrow -\infty \quad (4.36)$$

and

$$q \frac{\log b_2}{\log N_1} + \frac{\log \lambda_2}{\log N_1} + d \text{ as } q \rightarrow \infty. \quad (4.37)$$

If the multifractal auxiliary function of the N -ary cascade process is to approximate this N_1 -ary cascade as $q \rightarrow -\infty$ and $q \rightarrow \infty$, we require $p_{-\infty} = \lambda_1^\gamma$, $a_{-\infty} = b_1^\gamma$, $p_\infty = \lambda_2^\gamma$ and $a_\infty = b_2^\gamma$, where $\gamma = \log N / \log N_1$. Similarly for correspondence at $q = 0$ we need

$$1 - p_s = (1 - \lambda_0)^\gamma = (\lambda_1 + \lambda_2)^\gamma. \quad (4.38)$$

By proposition 4.1, if β is the almost sure multifractal auxiliary function of a binary cascade, we must have that

$$p_\infty a_\infty^q + (1 - p_s - p_\infty) a_{-\infty}^q \leq (\lambda_1 b_1^q + \lambda_2 b_2^q)^\gamma \leq p_{-\infty} a_{-\infty}^q + (1 - p_s - p_{-\infty}) a_\infty^q, \quad (4.39)$$

for all $q \geq 0$, that is

$$\lambda_2^\gamma b_2^{\gamma q} + ((\lambda_1 + \lambda_2)^\gamma - \lambda_2^\gamma) b_1^{\gamma q} \leq (\lambda_1 b_1^q + \lambda_2 b_2^q)^\gamma \leq \lambda_1^\gamma b_1^{\gamma q} + ((\lambda_1 + \lambda_2)^\gamma - \lambda_1^\gamma) b_2^{\gamma q}. \quad (4.40)$$

To obtain the right hand inequality for large q , comparing coefficients of $b_2^{\gamma q}$, we require $\lambda_2^\gamma \leq (\lambda_1 + \lambda_2)^\gamma - \lambda_1^\gamma$, that is

$$\lambda_1^\gamma + \lambda_2^\gamma \leq (\lambda_1 + \lambda_2)^\gamma. \quad (4.41)$$

Since $\gamma < 1$, this inequality fails for all $\lambda_1, \lambda_2 > 0$.

b) In exactly the same way, with $N_1^{\beta(q)-d} = \lambda_1 b_1^q + \dots + \lambda_k b_k^q$, we get, in place of (4.40)

$$\lambda_k^\gamma b_k^{\gamma q} + ((1 - \lambda_0)^\gamma - \lambda_k^\gamma) b_1^{\gamma q} \leq (\lambda_1 b_1^q + \dots + \lambda_k b_k^q)^\gamma \leq \lambda_1^\gamma b_1^{\gamma q} + ((1 - \lambda_0)^\gamma - \lambda_1^\gamma) b_k^{\gamma q} \quad (4.42)$$

for $q \geq 0$. By inspecting the right hand inequality as $q \rightarrow \infty$ and considering the dominant term in $b_k^{\gamma q}$, this implies that

$$\lambda_k^\gamma \leq (1 - \lambda_0)^\gamma - \lambda_1^\gamma, \quad (4.43)$$

giving the result.

Using a) with $N_1 = N^2$, so $\gamma = 1/2$, (4.40) becomes

$$\begin{aligned} \lambda_2^{1/2} b_2^{q/2} + ((\lambda_1 + \lambda_2)^{1/2} - \lambda_2^{1/2}) b_1^{q/2} \\ \leq (\lambda_1 b_1^q + \lambda_2 b_2^q)^{1/2} \leq \lambda_1^{1/2} b_1^{q/2} + ((\lambda_1 + \lambda_2)^{1/2} - \lambda_1^{1/2}) b_2^{q/2}. \end{aligned} \quad (4.44)$$

Squaring the left-hand inequality gives

$$b_1^q (\lambda_1 + 2\lambda_2 - 2\lambda_2^{1/2} (\lambda_1 + \lambda_2)^{1/2}) + 2b_1^{q/2} b_2^{q/2} \lambda_2^{1/2} ((\lambda_1 + \lambda_2)^{1/2} - \lambda_2^{1/2}) \leq \lambda_1 b_1^q. \quad (4.45)$$

This simplifies to

$$b_1^{q/2} \lambda_2 - b_1^{q/2} \lambda_2^{1/2} (\lambda_1 + \lambda_2)^{1/2} - b_2^{q/2} \lambda_2 + b_2^{q/2} \lambda_2^{1/2} (\lambda_1 + \lambda_2)^{1/2} \leq 0 \quad (4.46)$$

or

$$\left(b_1^{q/2} - b_2^{q/2} \right) \left(\lambda_2^{1/2} (\lambda_1 + \lambda_2)^{1/2} - \lambda_2 \right) \geq 0 \quad (4.47)$$

giving $b_2 \leq b_1$ for all $q > 0$, which is not the case. The right-hand inequality of (4.44) can be reduced to $b_2 \leq b_1$ in the same way. Similarly, if $q < 0$, the inequalities are reversed and again we get $b_2 \leq b_1$ from both inequalities. Thus we cannot arrange for the multifractal auxiliary function of the N -ary cascade to take the values of $\beta(q)$ of the N_1 -ary cascade for any $q \neq 0$. \square

In practice (4.31) and (4.32) are fulfilled in all the examples of section 4.2.4 where the multifractal functions are given analytically. Nevertheless, attempts to find a binomial cascade replicating the multifractal functions of multinomial cascade with a subdivision number $N = 4$ and a branching number $m = 16$ lead to (4.31) and (4.32) being violated. This is in accordance with corollary 4.2.

In many cases (4.31) and (4.32) are not fulfilled by rainfall data for negative q , and in some not even for positive q , so the auxiliary and multifractal functions of rainfall distributions cannot always be simulated by a random cascade process with fixed weights. In such cases, although the “ $k = 3$ ” scheme provides a random cascade with auxiliary function that corresponds at a few key values, see figure 4.7, no random cascade can give a good approximation for all q .

4.3.2 Moment conditions for an auxiliary function to be reproducible by a random cascade process

We derive some further restrictions on the auxiliary function of a random cascade process which may be applied over any range of q . These conditions are closely related to the conditions for the *Hausdorff moment problem* to have a solution, see (Widder, 1946) for a detailed discussion.

Recall that the auxiliary function $\beta(q)$ for a random cascade with weights W_i ($1 \leq i \leq m$), where $m = N^d$, satisfies

$$N^{\beta(q)} = \mathbb{E} \left(\sum_{i=1}^m W_i^q \right) = \sum_{i=1}^m \mathbb{E}(W_i^q). \quad (4.48)$$

(We do not require the W_i to be discrete random variables here.) For each $i = 1, \dots, m$ let W_i have distribution function ν_i so that $\nu_i : \mathbb{R} \rightarrow \mathbb{R}$ is increasing and such that

$$\mathbb{P}(W_i \leq \lambda) = \int_{-\infty}^{\lambda} d\nu_i(t). \quad (4.49)$$

Clearly ν_i is supported by $[0, 1]$ and $\nu_i[0, 1] = 1$. In particular for all q ,

$$\mathbb{E}(W_i^q) = \int_0^1 t^q d\nu_i(t).$$

Define $\nu : \mathbb{R} \rightarrow \mathbb{R}$ by $\nu = \sum_{i=1}^m \nu_i$. Then ν is supported by $[0, 1]$ and $\nu[0, 1] = m$. From (4.48) we get

$$N^{\beta(q)} = \int_0^1 t^q d\nu(t). \quad (4.50)$$

Proposition 4.3. *A necessary condition for $\beta(q)$ to be the auxiliary function of a random cascade process with N -ary subdivision is that for all $n \in \mathbb{Z}^+$ and $p_1, \dots, p_n \in \mathbb{R}$ the matrix*

$$\begin{pmatrix} N^{\beta(p_1+p_1)} & N^{\beta(p_1+p_2)} & \dots & N^{\beta(p_1+p_n)} \\ N^{\beta(p_2+p_1)} & N^{\beta(p_2+p_2)} & \dots & N^{\beta(p_2+p_n)} \\ \vdots & \vdots & \ddots & \vdots \\ N^{\beta(p_n+p_1)} & N^{\beta(p_n+p_2)} & \dots & N^{\beta(p_n+p_n)} \end{pmatrix} \quad (4.51)$$

is positive definite.

Proof. Let a_1, \dots, a_n be arbitrary real numbers. Let ν_i and ν be the distribution functions associated with the W_i , as above. Then

$$\begin{aligned} 0 &\leq \int (a_1 t^{p_1} + a_2 t^{p_2} + \dots + a_n t^{p_n})^2 d\nu(t) \\ &= \sum_{i=1}^n \sum_{j=1}^n a_i a_j \int t^{p_i+p_j} d\nu(t) \\ &= \sum_{i=1}^n \sum_{j=1}^n a_i a_j N^{\beta(p_i+p_j)} \end{aligned}$$

by (4.50). The condition for this quadratic expression to be non-negative for all a_1, \dots, a_n is that the matrix (4.51) is positive definite. \square

It is most convenient to work with a finite set of equally spaced points. For $j \in \mathbb{Z}^+$ and $q_0 \in \mathbb{R}, h \in \mathbb{R} > 0$ set

$$q_i = q_0 + ih$$

for $i = 0, \dots, 2j$.

Corollary 4.4. *A necessary condition for $\beta(q_0), \dots, \beta(q_{2j})$ to be the values of the auxiliary function of a N -ary random cascade process is that the matrix*

$$\begin{pmatrix} N^{\beta(q_0)} & N^{\beta(q_1)} & \dots & N^{\beta(q_j)} \\ N^{\beta(q_1)} & N^{\beta(q_2)} & \dots & N^{\beta(q_{j+1})} \\ \vdots & \vdots & \ddots & \vdots \\ N^{\beta(q_j)} & N^{\beta(q_{j+1})} & \dots & N^{\beta(q_{2j})} \end{pmatrix} \quad (4.52)$$

is positive definite.

Proof. This result can be obtained from proposition 4.3 by setting $n = j + 1$ and $p_i = \frac{1}{2}q_0 + (i - 1)h$ for $i = 1, \dots, n$. \square

Recall that a necessary and sufficient condition for a matrix to be positive definite is for all square sub-matrices obtained by deleting the i -th row and i -th column for some set of i to have positive determinants.

In particular, for 2×2 sub-matrices, this requires that for all $q_0, q_2 \in \mathbb{R}$ and $q_1 = \frac{1}{2}(q_0 + q_2)$

$$\begin{vmatrix} N^{\beta(q_0)} & N^{\beta(\frac{1}{2}(q_0+q_2))} \\ N^{\beta(\frac{1}{2}(q_0+q_2))} & N^{\beta(q_2)} \end{vmatrix} \geq 0. \quad (4.53)$$

Thus

$$N^{\beta(q_0)+\beta(q_2)} \geq N^{2\beta(\frac{1}{2}(q_0+q_2))}$$

or equivalently

$$\beta\left(\frac{q_0 + q_2}{2}\right) \leq \frac{\beta(q_0) + \beta(q_2)}{2}, \quad (4.54)$$

for all $q_0, q_2 \in \mathbb{R}$, that is $\beta(q)$ is midpoint-concave. Since every continuous mid-point concave function is concave and β is continuous, this says that $\beta(q)$ is concave. But every reasonable auxiliary function $\beta(q)$ is continuous and concave, see section 1.1.2, so (4.53) will be automatically satisfied.

The 3×3 sub-matrices provide a more useful necessary condition for the representation of a multifractal auxiliary function by a random cascade process. Thus a necessary condition for $\beta(q_0), \dots, \beta(q_4)$ to be values of a auxiliary function by an N -ary random cascade process is that

$$\begin{vmatrix} N^{\beta(q_0)} & N^{\beta(q_1)} & N^{\beta(q_2)} \\ N^{\beta(q_1)} & N^{\beta(q_2)} & N^{\beta(q_3)} \\ N^{\beta(q_2)} & N^{\beta(q_3)} & N^{\beta(q_4)} \end{vmatrix} \geq 0. \quad (4.55)$$

Note that necessary conditions of the form (4.52) and (4.55) can be used to test for compatibility of a random cascade over a limited range of q , whereas the conditions of section 4.3.1, which depend on the asymptotes, entail an unbound range of q .

In practice (4.55) appears to be satisfied in all examples examined, and not a useful test in determining whether a $\beta(q)$ function is reproducible by a random cascade.

4.3.3 Conclusion

From the results of sections 4.3.1 and 4.3.2 it is clear that there are considerable limitations on the multifractal auxiliary functions and spectra that may be represented using binary random cascades with fixed weights. In particular corollary 4.2 shows that the assumption that this kind of random cascade is the appropriate choice to simulate an observed multifractal structure needs to be approached with caution.

Chapter 5

Slices of multifractal measures and applications to rainfall distributions

5.1 Introduction

In this chapter the relationship between the multifractal functions of a plane measure and those of slices or sections of the measure with a line is discussed.

Motivated by recent mathematical ideas about the relationship between measures and their slices we formulate the “slice hypothesis”. By examining an example we discuss theoretical limitations of this hypothesis.

We compute the multifractal functions of several standard self-similar and self-affine measures and their slices. By comparing them we examine the validity of the slice hypothesis.

We are particularly interested in using the slice hypothesis to estimate multifractal properties of spatial rainfall fields by analysing rainfall data representing slices of rainfall fields. We consider how rainfall time series at a fixed site and slices of composite radar images can be used for this purpose, testing this on field data from a radar composite in the USA and on appropriate time series.

A version of this chapter has been published (Lammering, 2000).

5.2 Theoretical background

5.2.1 Slices of measures

We first define what we mean by slices or sections of measures. Here we are only concerned with slices of plane sets by lines, but there are natural higher dimensional analogues.

We define the slice of a measure by a line as a normalised limit of the measure in small strips centred on the line. More precisely, let μ be a measure on \mathbb{R}^2 and let L_δ be the δ -neighbourhood of a line L . The *slice* of the measure μ with the line L , denoted by μ_L , is essentially defined by

$$\mu_L(E \cap L_\delta) = \lim_{\delta \rightarrow 0} \frac{\mu(E \cap L_\delta)}{2\delta}, \quad (5.1)$$

for Borel sets $E \subset \mathbb{R}^2$. More formally, μ_L is defined by the property that

$$\int f \, d\mu_L = \frac{1}{2\delta} \lim_{\delta \rightarrow 0} \int_{L_\delta} f \, d\mu, \quad (5.2)$$

for all continuous functions f on \mathbb{R}^2 with compact support. It turns out that the limits in (5.1) and (5.2) exist for almost all lines L parallel to a given line, see Mattila (1995, chapter 10) for measure theoretic detail of slices. Moreover, under certain circumstances, the sliced measure integrates up to give the original measure, i.e. if L_a is the line L under parallel displacement a , then $\mu(E) = \int \mu_{L_a}(E \cap L_a) da$. This is certainly the case for almost all directions of lines L if the measure is not too concentrated in the sense that

$$\int \frac{d\mu(x)d\mu(y)}{|x-y|} < \infty,$$

see Mattila (1995).

5.2.2 Fractal and multifractal properties of slices

It is reasonable to expect that the dimension or multifractal properties of a typical slice of a set E or a measure μ are related to those of E or μ themselves.

Results on the Hausdorff dimension of slices of sets are well-established, see Falconer (1990, chapter 8), Mattila (1995). In particular, if E is a Borel set in \mathbb{R}^2 , we have

$$\dim_H(E \cap L) \leq \max(0, \dim_H E - 1) \quad (5.3)$$

for almost all lines L in the plane and

$$\dim_H(E \cap L) = \max(0, \dim_H E - 1) \quad (5.4)$$

for a set of L of positive measure with respect to the natural measure on the set of all lines in the plane.

It is natural to expect corresponding results for auxiliary functions of multifractal measures. Let μ be a measure on \mathbb{R}^2 , and μ_L be its slice by the line L . As usual we write $\beta(q)$ for the auxiliary function of μ and $\beta_L(q)$ for the auxiliary function of μ_L . It is reasonable to hope that, for a “typical” line L , the auxiliary function $\beta_L(q)$ is a modification of $\beta(q)$ by a linear shift, representing the auxiliary function of the line, that is for almost all lines L in the plane

$$\begin{aligned} \beta_L(q) &\leq \max(\beta(q) - (1 - q), 0), \quad q \leq 1 \\ \beta_L(q) &\geq \min(\beta(q) - (1 - q), 0), \quad q \geq 1 \end{aligned} \quad (5.5)$$

and for a set of L of positive measure

$$\begin{aligned} \beta_L(q) &= \max(\beta(q) - (1 - q), 0), \quad q \leq 1 \\ \beta_L(q) &= \min(\beta(q) - (1 - q), 0), \quad q \geq 1. \end{aligned} \quad (5.6)$$

Hence the multifractal auxiliary function of a typical section is achieved by subtracting $(1 - q)$, which is the auxiliary function of the Lebesgue measure of a line segment, from the auxiliary function of the original measure. Note that the possibility of $\beta_L(q) = 0$ corresponds to L intersecting μ in a measure of trivial structure.

Note that if

$$\beta_L(q) = \beta(q) - (1 - q) \quad (5.7)$$

then with α and f for the variables in the Legendre transform of $\beta(q)$ and α_L and f_L for those in the Legendre transform of $\beta_L(q)$, we have in terms of the parameter q

$$\alpha_L(q) = -\frac{d\beta_L}{dq}(q) = -\frac{d\beta}{dq}(q) - 1 = \alpha(q) - 1 \quad (5.8)$$

and

$$f_L(q) = \beta_L(q) + q\alpha_L(q) = \beta(q) + q\alpha(q) - 1 = f(q) - 1. \quad (5.9)$$

Thus the Legendre multifractal spectrum satisfies

$$f_L(\alpha) = f(\alpha + 1) - 1, \quad (5.10)$$

provided we are in a range of q where (5.7) holds, that is the graph of the multifractal spectrum of μ_L is that of μ shifted unit distance to the left and unit distance downwards.

5.2.3 The slice hypothesis

We shall say that a measure μ on \mathbb{R}^2 satisfies the *slice hypothesis* if for a typical line L , that is a set of lines L of a positive measure with regard to the natural measure on the line, we have

$$f_L(\alpha) = f(\alpha + 1) - 1 \quad (5.11)$$

for values of α for which $f(\alpha + 1) - 1 \geq 0$. Equivalently this requires

$$\beta_L(q) = \beta(q) - (1 - q) \quad (5.12)$$

for values of q for which $\beta(q) - q \frac{d\beta(q)}{dq} \geq 0$.

It is believed that the slice hypothesis holds for a large class of measures in \mathbb{R}^2 , see Mandelbrot (1990). There are considerable technical difficulties in establishing such results rigorously. Olsen (1998a) has studied slices of measures with an alternative definition of β based on an analogue of Hausdorff rather than box counting dimension. Falconer and O'Neil (1999) prove that $\beta_L(q) \leq \beta(q) - (1 - q)$ for certain q . Nevertheless, much theoretical work still needs to be done in this area.

5.2.4 Negative dimensions

Since the multifractal spectrum of a measure μ on \mathbb{R}^2 may take values of $f(q) < 1$, the shift given by (5.10) may result in negative values for f_L . Of course, such negative values cannot be achieved by any direct calculation or computational estimate of the spectrum of μ_L for a given line L . Similarly, Schertzer et al. (1997) describe the paradox of negative/latent dimensions, originating from performing calculations on a number of samples.

Intuitively, negative dimensions might correspond to the possibility that there is a small set of points in \mathbb{R}^2 where μ has a very high local density. Such points will be missed by almost all lines L_a , and so will not be observed on typical slices of the measure. Nevertheless, the presence of high density points means that, exceptionally, a slice may pick up a high measure concentration.

Negative dimensions reflect that a highly localised measure density may occasionally be observed in a random slice, albeit with zero probability. Thus negative dimensions need to be thought of in the context of what might be observed in the class of all slices rather than what can be observed in a single slice.

Mandelbrot et al. (1990) and Mandelbrot (1991, 1995) have developed these ideas somewhat further. Certain random measures lead to an auxiliary function $\beta(q)$ with a Legendre transform $f(\alpha)$ that takes negative values, see Falconer (1995) and Olsen (1995). A random measure may be interpreted as a random sample, for example a random section, of a virtual deterministic measure on a higher dimensional space, with the Legendre spectrum $f(\alpha)$ being the result of an axis shift of that of the virtual measure.

5.2.5 An example

For sets that are inhomogeneous or non-isotropic, box dimension and auxiliary functions based on box counting methods are less well behaved with respect to sections than Hausdorff dimensions. The following highly inhomogeneous and non-isotropic example illustrates this.

Example. Let $F = \{(0, 0)\} \cup \bigcup_{k=1}^{\infty} [0, k^{-1/2}] \times \{k^{-1/2}\}$, see figure 5.1. We claim that

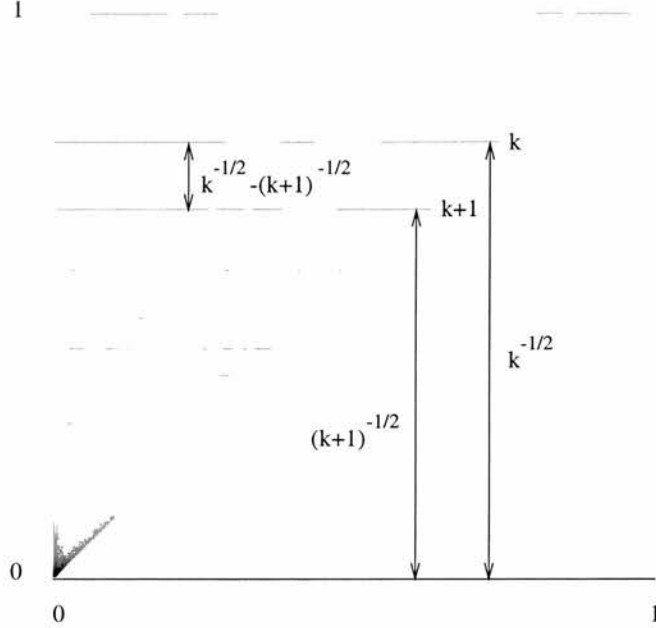


Figure 5.1: A set that violates the slice hypothesis

$\dim_H F = 1$ and $\dim_B F = 4/3$. For every line L that does not pass through $(0, 0)$, the slice $F \cap L$ is finite, so $\dim_B(F \cap L) = \dim_H(F \cap L) = 0$. Thus although (5.4) applies to Hausdorff dimension it does not apply to box dimension in this case.

Proof. Since F is a countable union of line segments, $\dim_H F = 1$.

For the box dimension, let $0 < r < 1/4$ and let k be the integer such that

$$(k+1)^{-1/2} - (k+2)^{-1/2} \leq r < k^{-1/2} - (k+1)^{-1/2}, \quad (5.13)$$

so

$$c_1 k^{-3/2} \leq r < c_2 k^{-3/2}, \quad (5.14)$$

where c_1, c_2 are independent of r . Writing $N_r(F)$ for the number of squares of the r -mesh intersected by F , we have, since all r -mesh squares in the triangle $(0, 0), (0, (k+1)^{-1/2}), ((k+1)^{-1/2}, (k+1)^{-1/2})$ intersect F ,

$$\frac{1}{2}(k+1)^{-1} r^{-2} \leq N_r(F) \leq (k+1)^{-1} r^{-2} + 2 \sum_{i=1}^k (i^{-1/2} r^{-1}). \quad (5.15)$$

Thus for small r or large k , since

$$\sum_{i=1}^k i^{-1/2} \leq c k^{1/2} \leq c' r^{-1/3}, \quad (5.16)$$

we get

$$c_3 r^{2/3} r^{-2} \leq N_r(F) \leq c_4 [r^{2/3} r^{-2} + r^{-1} k^{1/2}], \quad (5.17)$$

$$\text{so } c_3 r^{-4/3} \leq N_r(F) \leq c_5 r^{-4/3}. \quad (5.18)$$

It follows that $\dim_B F = 4/3$.

Clearly any line L that does not pass through $(0, 0)$ intersects F in finitely many points and so $\dim_B(F \cap L) = 0$. \square

By defining suitable measures on this set, similar arguments show that (5.12) may be far from true. Thus we cannot always expect the slice hypothesis, based on a box-counting argument, to apply in such cases where the measure has bad homogeneity or isotropy properties.

5.3 Computation of slices of measures

In this section we investigate computationally the relationships between the multifractal auxiliary function and the multifractal spectrum of measures and those of their slices by lines and in particular seek computational verification of the slice hypothesis. We need to approximate μ_L computationally, and since we cannot in practice take the limit as $\delta \rightarrow 0$ in (5.1) and (5.2), we have to approximate μ_L by the restriction of μ to a narrow strip L_δ , normalised in an appropriate way. Even if μ is defined by a very large data set, the size of the data set within L_δ will be small. Inevitably, this leads to computational difficulties. However, if μ is represented by the density of a sequence of points, one can regard μ_L as represented by the linear density of those points within the strip. For measures generated by iteration or by the chaos game, this can provide an adequate data set for μ_L , see figure 5.2. One can only hope to get reasonable approximations to the measure μ_L of a

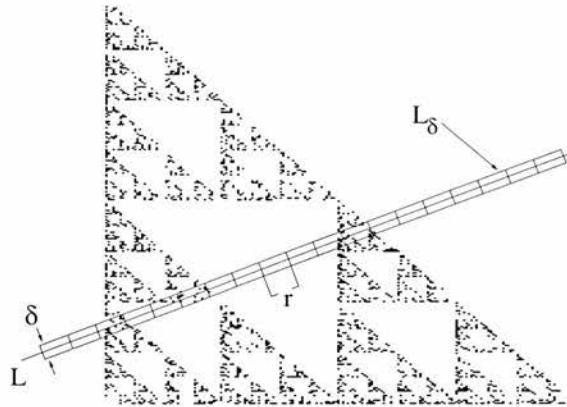


Figure 5.2: Approximation to a slice of a measure on a Sierpiński triangle by the line L

subinterval of L if the length of the interval is large compared with the width δ of the approximating strip L_δ . In particular, for the box-counting involved in estimating the auxiliary function of μ_L , the length of the boxes in L_δ must be large compared with δ . Thus to estimate the auxiliary function, L_δ is divided into long thin rectangles. In practice, for the examples below, calculations were performed using a strip of width $\delta = 2^{-16}$, and box side-lengths, i.e. interval lengths, down to $r = 2^{-11}$.

5.4 Examination of the slice hypothesis using standard examples

We examine the slice hypothesis by comparing the auxiliary function and Legendre spectrum of standard self-similar and self-affine measures with those computed for their slices.

We apply the standard and, where appropriate, enlarged box-counting algorithms, see section 1.3.3, to calculate $\beta_L(q)$, the auxiliary function of the slice of a plane measure by L , for a range of q from -5 to 5. We compare these results with the theoretically calculated values for the plane measures, assuming (5.12). We calculate the multifractal spectra $f_L(\alpha)$ by Legendre transformation and again compare with the values expected assuming (5.11).

5.4.1 Random cascade measure

The first example is a random cascade measure with discrete weights on the unit square, see section 1.2.4. The subdivision number is $N = 2$ and two different sets of weight probabilities are chosen. Measure *RC1* is characterised in the notation of (1.44) by

$$RC1: \begin{array}{|c|c|c|c|} \hline p_0 = 0.030 & p_1 = 0.200 & p_2 = 0.300 & p_3 = 0.470 \\ \hline a_0 = 0.000 & a_1 = 0.170 & a_2 = 0.380 & a_3 = 0.217 \\ \hline \end{array}$$

corresponding to a covering fraction of $u = 0.715$ at 11 iterations, see (1.46), and measure *RC2* by

$$RC2: \begin{array}{|c|c|c|c|} \hline p_0 = 0.136 & p_1 = 0.200 & p_2 = 0.300 & p_3 = 0.364 \\ \hline a_0 = 0.000 & a_1 = 0.170 & a_2 = 0.380 & a_3 = 0.280 \\ \hline \end{array}$$

corresponding to a covering fraction of $u = 0.2$ at 11 iterations. The multifractal auxiliary function is given by (1.48). The measures of the slices by lines L are approximated by subdividing a strip of width δ of order 2^{-16} into 2^{11} intervals of length r of order 2^{-11} . The lines are chosen to have an angle ϕ to the x -axis. Several slices with different ϕ are computed. The results presented are for $\phi = 0.541$ rad and $\phi = 0.366$ rad. The slice measure is fairly irregular so that clipping is likely. We use the standard box-counting algorithm for $q \geq 0$ and enlarged box-counting for $q < 0$. Figures 5.3 to 5.10 show the computed auxiliary functions and multifractal spectra of the μ_L and those found analytically for the μ and shifted according to the slice hypothesis. Three different realisations of the random measures μ_L are generated and in each case analysed. From the graphs we observe:

- 1) A good agreement between the computed multifractal functions of sections for different realisations of the cascade with the same parameters. This suggests the computational method is robust.
- 2) Little difference in multifractal properties of slices for different lines, that is for different ϕ .
- 3) In general good agreement of the shifted, theoretical auxiliary functions and multifractal spectra with the computed functions for slices, provided $f(\alpha) > 0$.
- 4) For measures with a large support and relatively small variation, as in *RC1*, the agreement with the slice hypothesis is better than for measures with a smaller support, as in *RC2*, where clipping may have a greater effect, especially for $q < 0$.

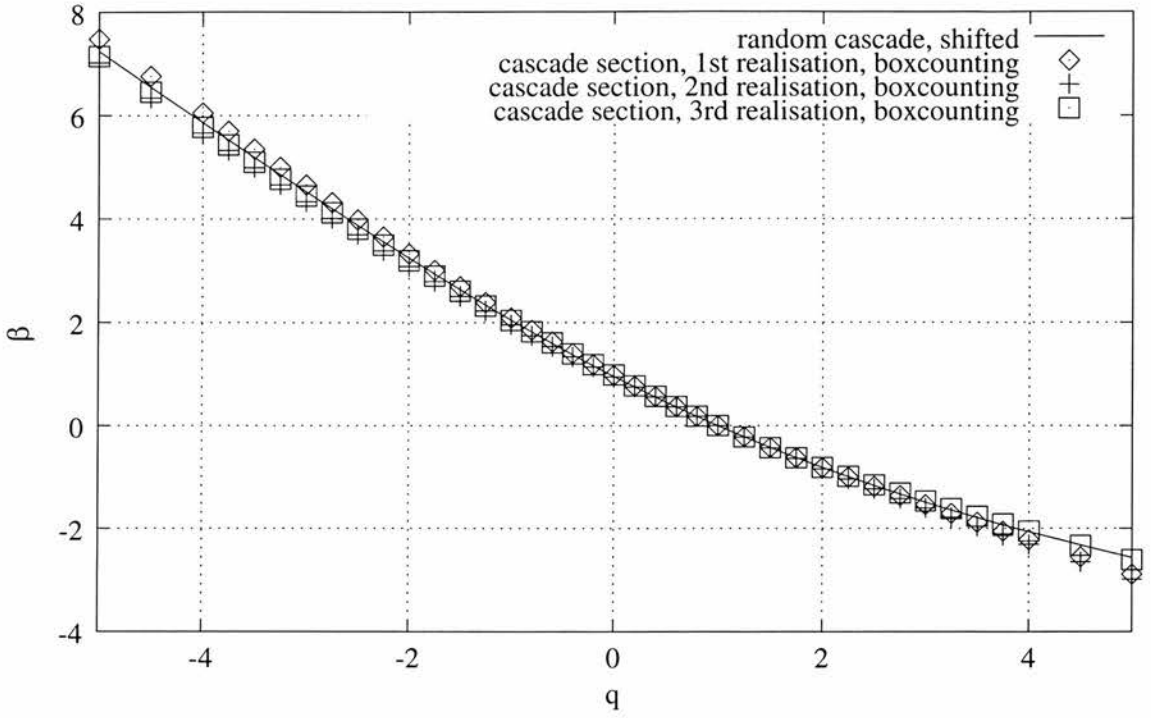


Figure 5.3: $\beta(q)$ of the random cascade *RC1* for a slice at angle $\phi = 0.541$ rad, according to the slice hypothesis and estimated by box-counting

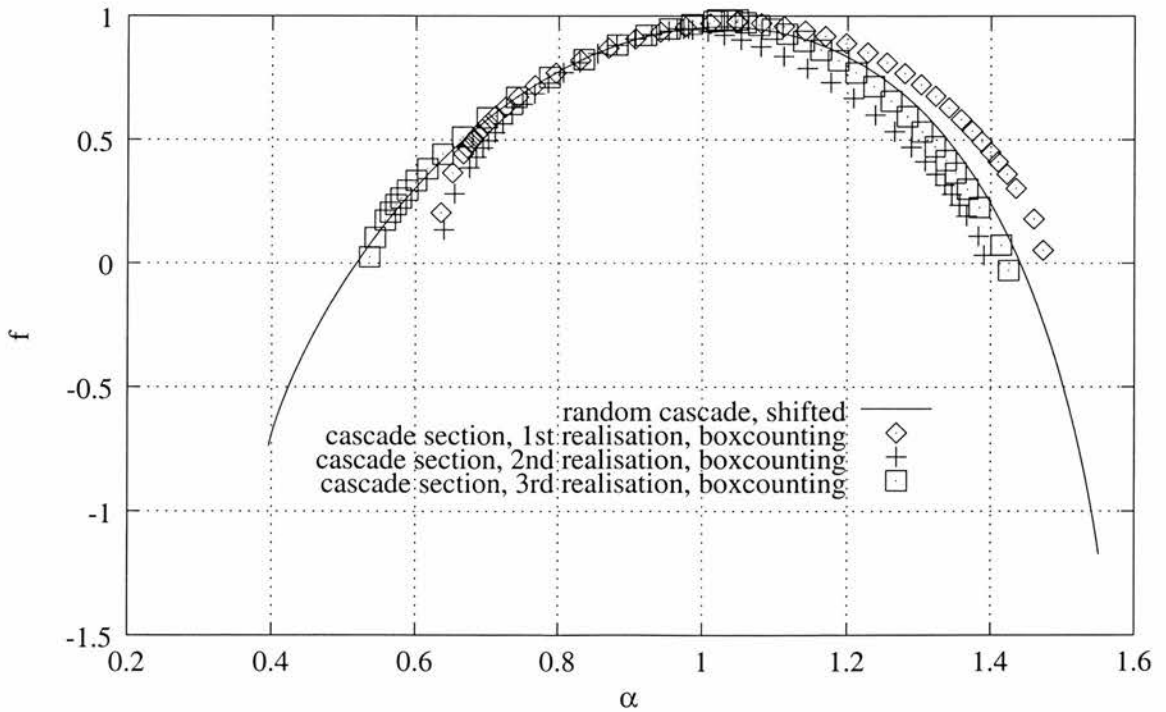


Figure 5.4: $f(\alpha)$ of the random cascade *RC1* for a slice at angle $\phi = 0.541$ rad, according to the slice hypothesis and estimated by box-counting

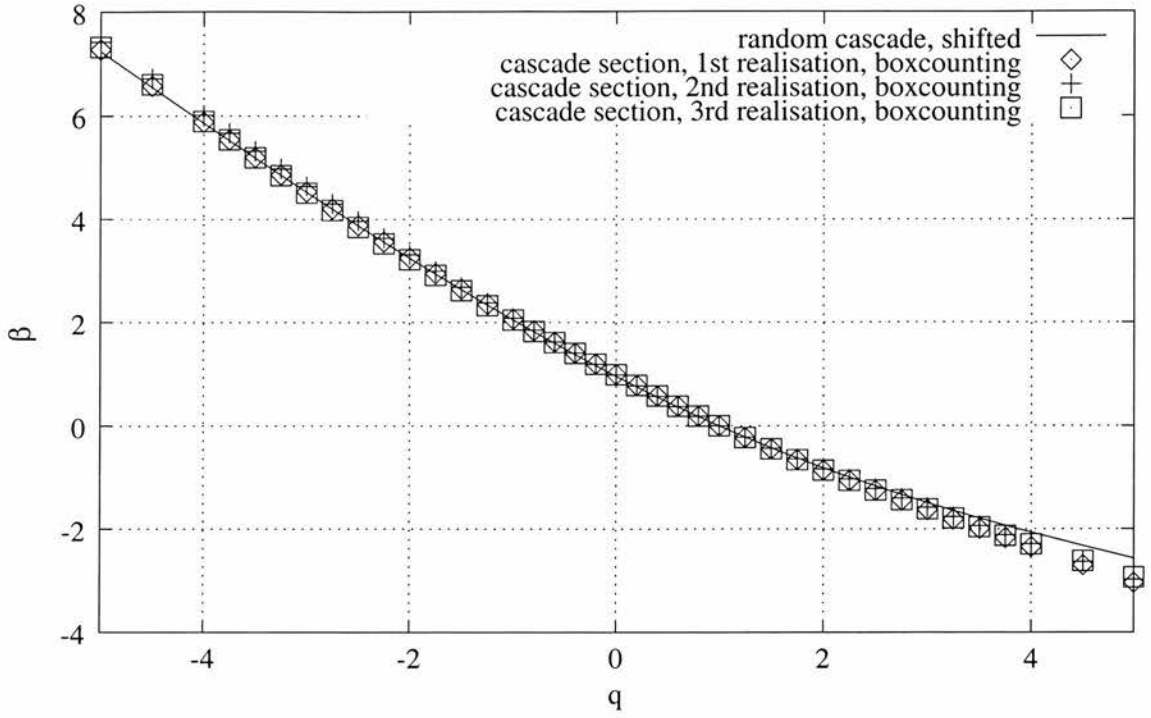


Figure 5.5: $\beta(q)$ of the random cascade *RC1* for a slice at angle $\phi = 0.366$ rad, according to the slice hypothesis and estimated by box-counting

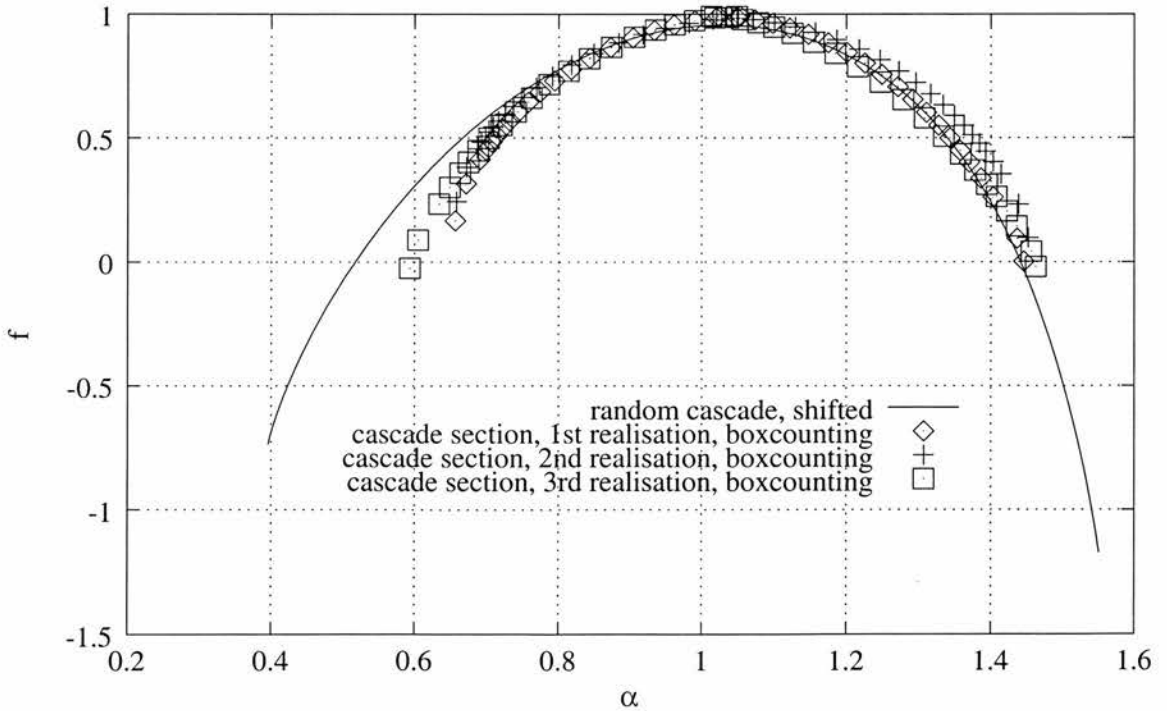


Figure 5.6: $f(\alpha)$ of the random cascade *RC1* for a slice at angle $\phi = 0.366$ rad, according to the slice hypothesis and estimated by box-counting

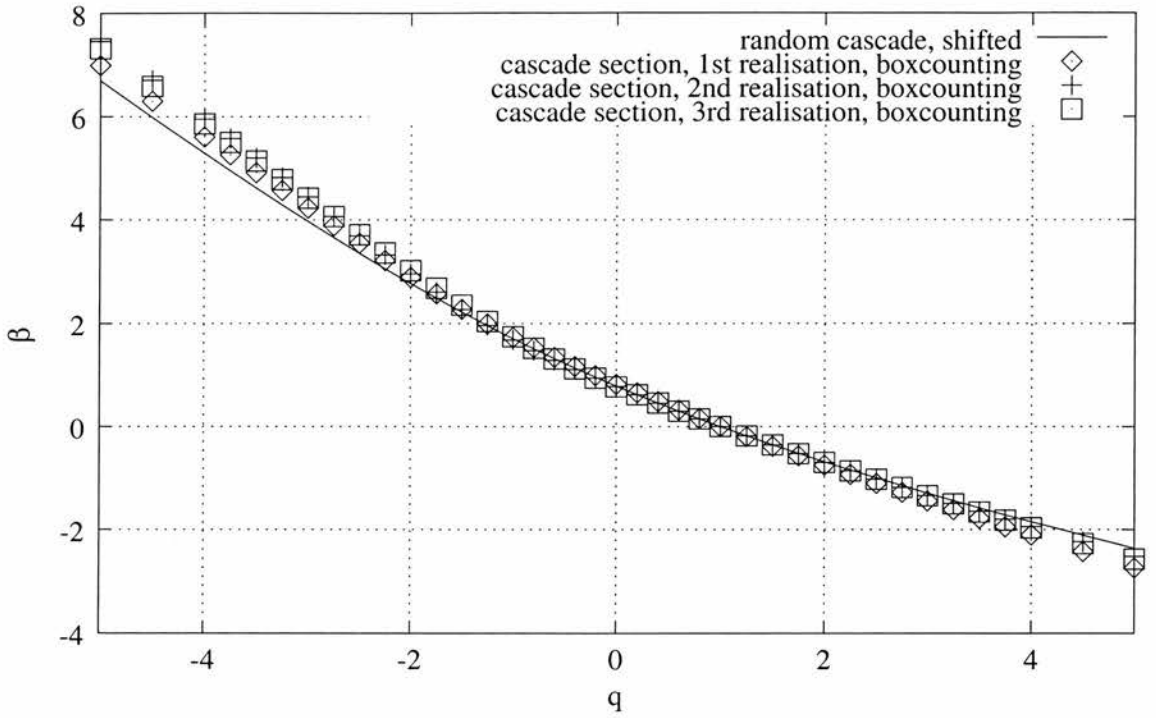


Figure 5.7: $\beta(q)$ of the random cascade $RC2$ for a slice at angle $\phi = 0.541$ rad, according to the slice hypothesis and estimated by box-counting

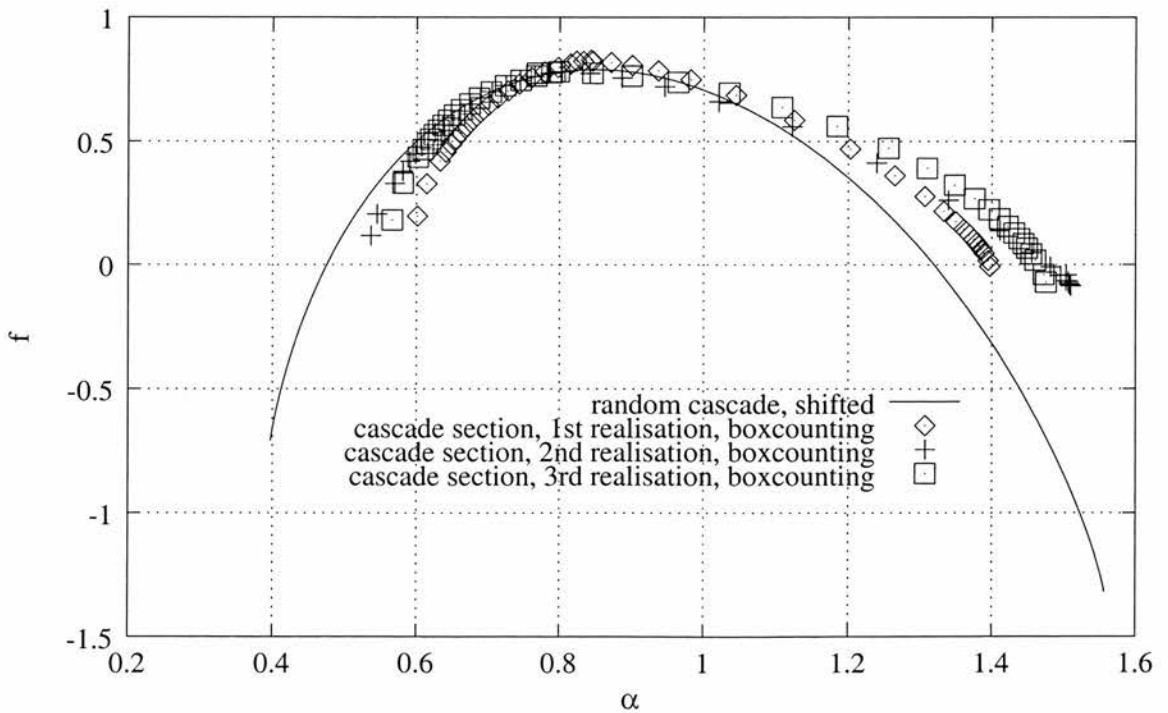


Figure 5.8: $f(\alpha)$ of the random cascade $RC2$ for a slice at angle $\phi = 0.541$ rad, according to the slice hypothesis and estimated by box-counting

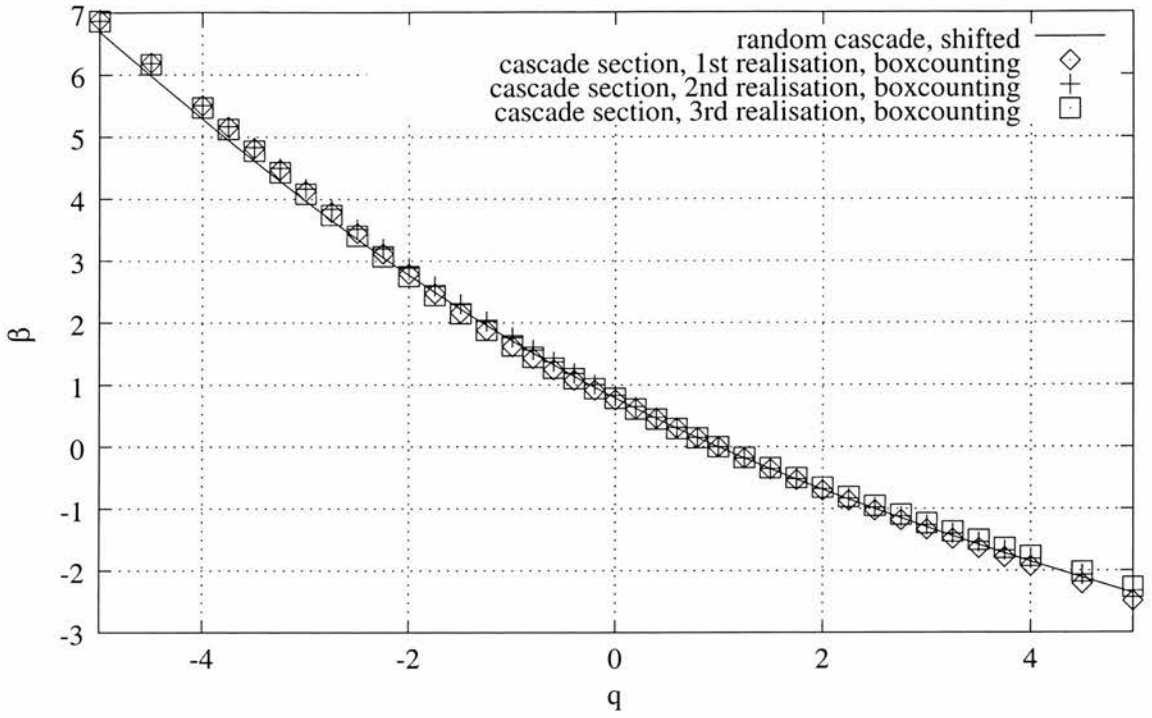


Figure 5.9: $\beta(q)$ of the random cascade *RC2* for a slice at angle $\phi = 0.366$ rad, according to the slice hypothesis and estimated by box-counting

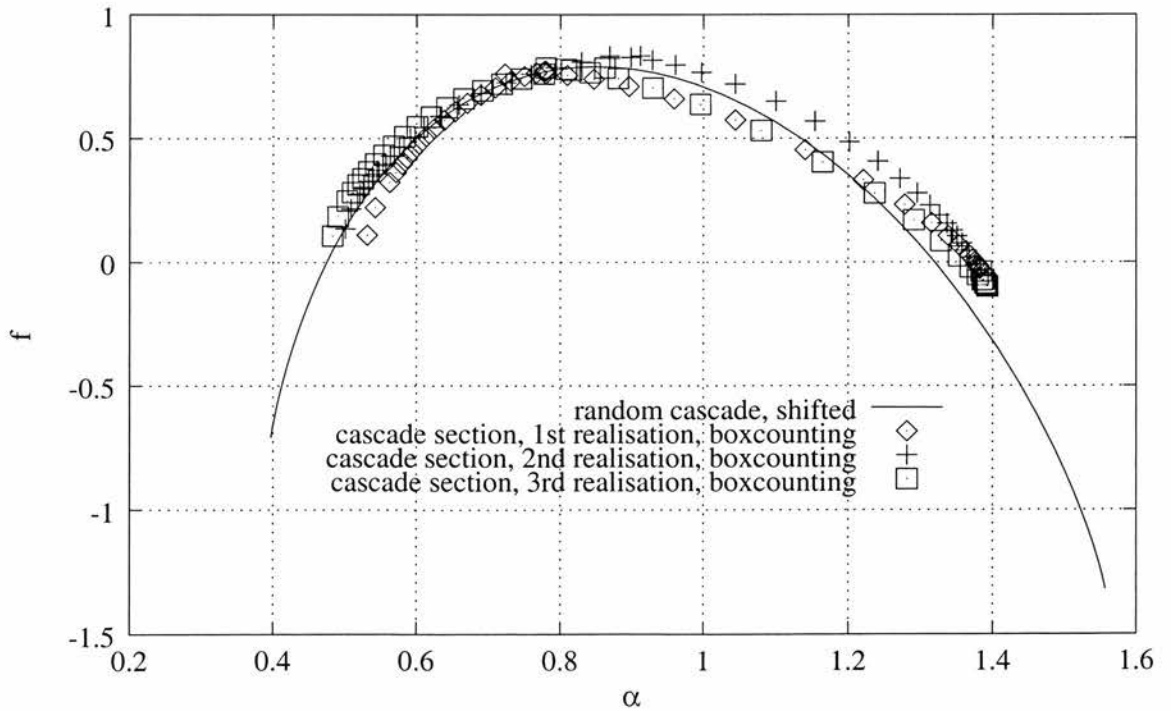


Figure 5.10: $f(\alpha)$ of the random cascade *RC2* for a slice at angle $\phi = 0.366$ rad, according to the slice hypothesis and estimated by box-counting

5.4.2 Self-similar measure on a Sierpiński triangle

The second class of measures we examine are deterministic self-similar measures supported by a Sierpiński triangle F , see section 1.1.3. The transformations S_1, S_2, S_3 , given by (1.25) define F and the probability measure μ is defined by weights $w_1, w_2, w_3 > 0$, where $w_1 + w_2 + w_3 = 1$.

For computational purposes we calculate μ_L using the chaos game, see section 1.1.3. The slice measure is determined by the first 300,000 points at distance less than $r = 0.00002$ from the line L . This gives a strip of width of order 2^{-14} , which is divided into 2^{11} boxes of length of order 2^{-11} . The first measure, $ST1$, has the weights

$$ST1: \quad \boxed{w_1 = 0.1 \quad w_2 = 0.3 \quad w_3 = 0.6}$$

and the second, $ST2$, has the weights

$$ST2: \quad \boxed{w_1 = 0.2 \quad w_2 = 0.3 \quad w_3 = 0.5}$$

The slices are characterised by the angle ϕ to the x -axis and the y -offset. We compute several slices with different ϕ and y -offset 0.01. The results presented are for $\phi = 0.506$ rad and $\phi = 0.646$ rad.

Since the support of μ is fractal, both μ and μ_L have wide and sudden variations in their density so that clipping occurs. To eliminate this effect we use enlarged box-counting for negative q . Figures 5.11 to 5.14 show the results of the multifractal analysis of the section compared with that expected by the slice hypothesis using the analytical form of $\beta(q)$ for a self similar measure, see (1.30). From the graphs we observe:

- 1) A small variation between the spectra for different slices, particularly for $q < 0$. This may be due to significant variations in the sparsity of the intersection of the Sierpiński triangle with the line at scales at which the computation is made.
- 2) Reasonable agreement with the predicted spectra of the slices on the assumption of the slice hypothesis, at least for $q > 0$.
- 3) A greater divergence from the predicted spectra than in the case of sections of random cascade slices. This may be due to the greater sparseness of the support, leading to fewer intervals in the slices with positive measure, so that the multifractal computation is effectively based on fewer boxes.

5.4.3 Self-affine measure on a generalised Sierpiński triangle

The third measures we examine are self-affine measures supported by a generalised Sierpiński triangle as described in section 2.3. The affine transformations S_1, S_2, S_3 , given by (2.2) define the generalised Sierpiński triangle. We choose parameters $a = 0.75, b = 0.4$ in the construction of the generalised Sierpiński triangle, see figure 2.3. The probability measure μ is constructed with weights $w_1, w_2, w_3 > 0$ with $w_1 + w_2 + w_3 = 1$. Multifractal analysis of this measure is addressed in section 2.3. The multifractal auxiliary function $\beta(q)$ is given by theorem 2.3.

We compute the intersection measures in exactly the same way as in 5.4.2, using the chaos game. The first measure, $GT1$, has the weights

$$GT1: \quad \boxed{w_1 = 0.1 \quad w_2 = 0.3 \quad w_3 = 0.6}$$

and the second, $GT2$, has the weights

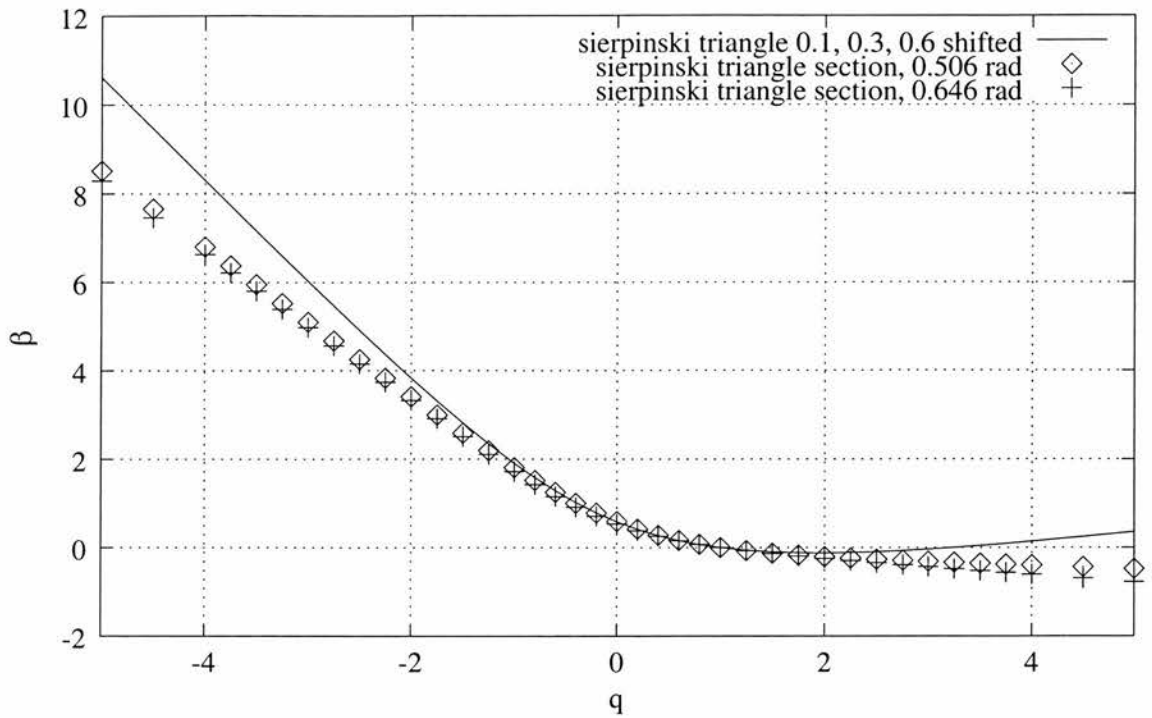


Figure 5.11: $\beta(q)$ of the Sierpiński triangle measure $ST1$ for slices at angles $\phi = 0.506$ rad and $\phi = 0.646$ rad, according to the slice hypothesis and estimated by box-counting

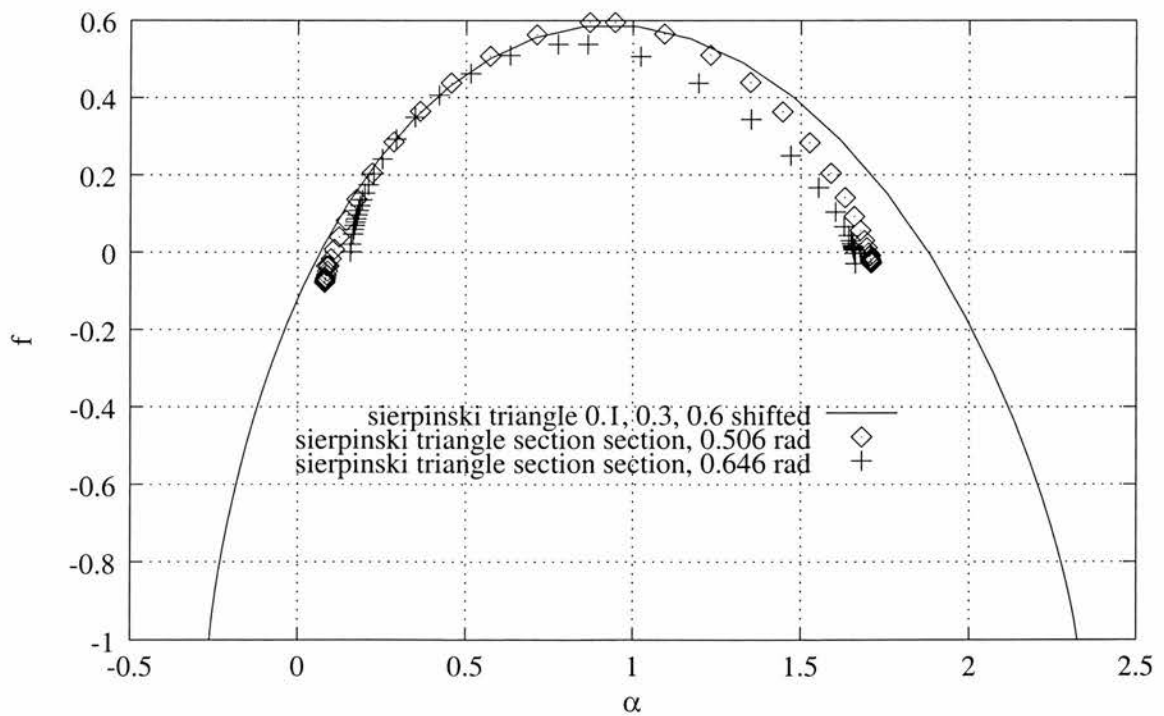


Figure 5.12: $f(\alpha)$ of the Sierpiński triangle measure $ST1$ for slices at angles $\phi = 0.506$ rad and $\phi = 0.646$ rad, according to the slice hypothesis and estimated by box-counting

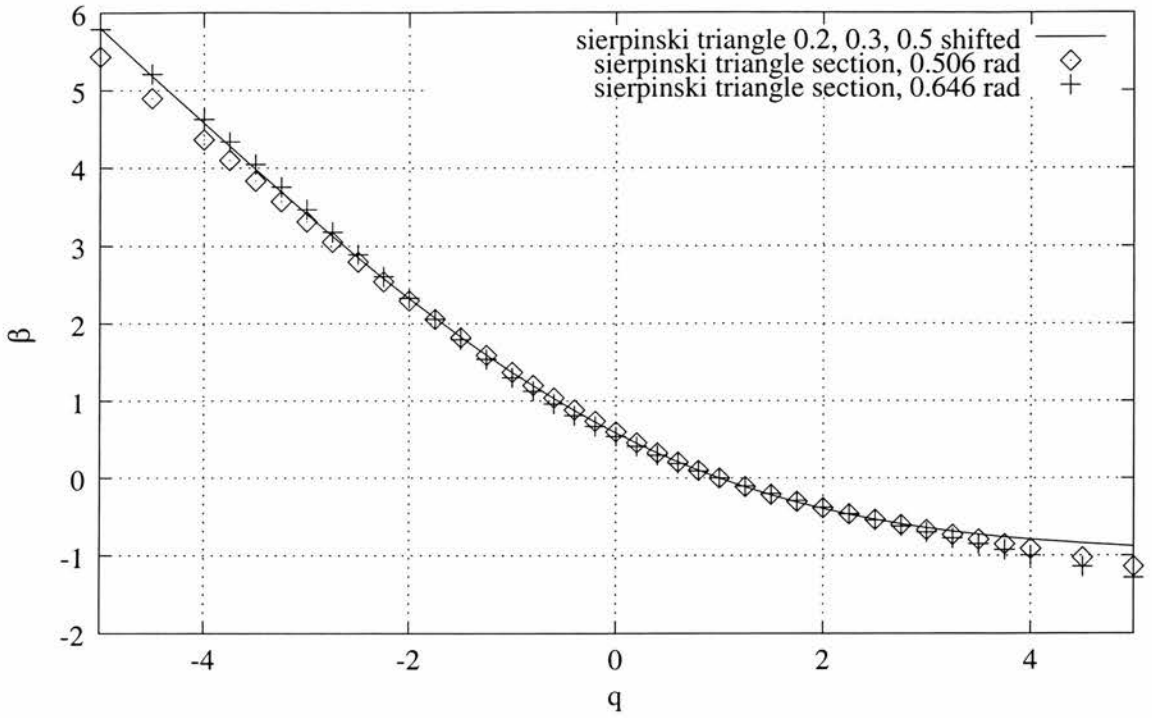


Figure 5.13: $\beta(q)$ of the Sierpiński triangle measure $ST2$ for slices at angles $\phi = 0.506$ rad and $\phi = 0.646$ rad, according to the slice hypothesis and estimated by box-counting

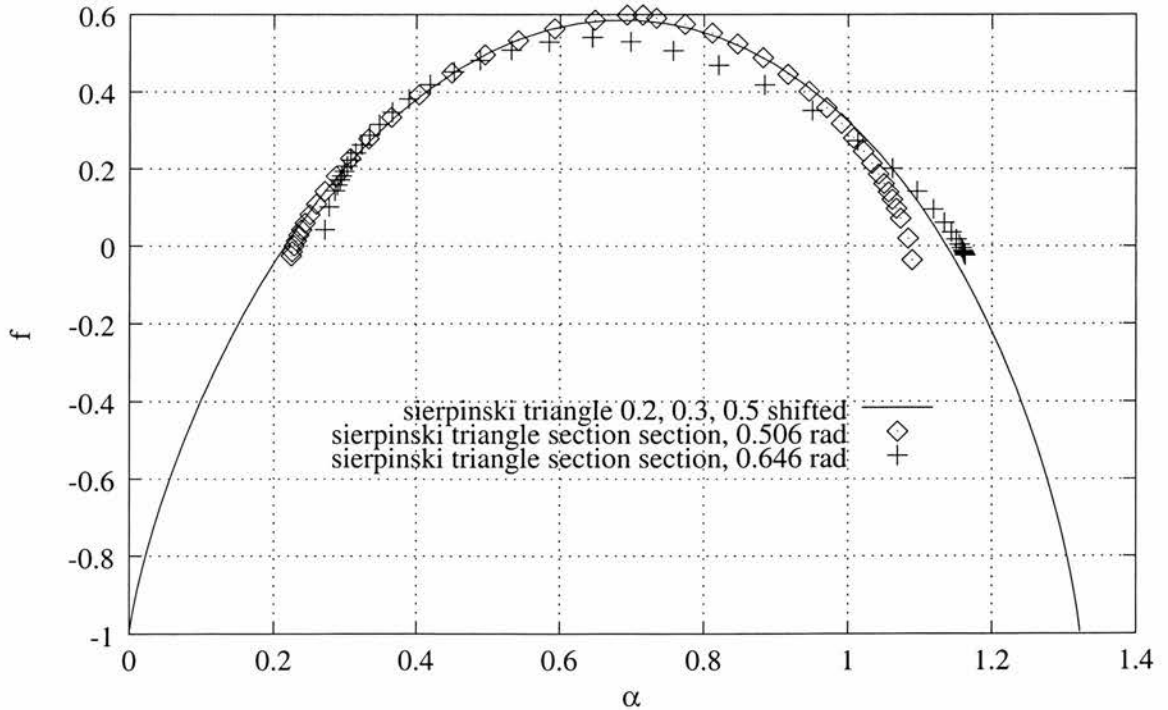


Figure 5.14: $f(\alpha)$ of the Sierpiński triangle measure $ST2$ for slices at angles $\phi = 0.506$ rad and $\phi = 0.646$ rad, according to the slice hypothesis and estimated by box-counting

$$GT2: \quad \boxed{w_1 = 0.2 \quad w_2 = 0.3 \quad w_3 = 0.5}$$

The lines of intersection are chosen to have an y -offset of 0.01 with angles to the x -axis $\phi = 0.506$ rad and $\phi = 0.646$ rad.

The figures 5.15 to 5.18 show the results of the multifractal analysis of the slice of the multinomial measure on the generalised Sierpiński triangle. From the graphs we observe

- 1) A considerable variation between the spectra computed for different sections, particularly for the more extreme values of weights.
- 2) A poor agreement of the computed spectra with those predicted by the slice hypothesis, even for the dimension of the support, when $q = 0$. The lack of isotropy here may produce an effect such as that in the example in section 5.2.5.

5.4.4 Discussion of computational results

From these computational investigations of slices of measures where the multifractal spectrum is known analytically, we may draw certain conclusions relating to the slice hypothesis.

- 1) The results tend to be better if the support of μ is large, i.e. has a large dimension. This may be largely a computational effect, since for a measure of sparse support, the slice will be covered by relatively few boxes that contribute to the moment sums, and clipping will be significant for $q < 0$.
- 2) The slice hypothesis is a reasonable assumption when μ is fairly homogeneous and isotropic, as in the case of the random cascades and self-similar measures. The self-affine sets contain certain preferred directions and this might be expected to lead to the slice properties varying significantly within the line chosen.
- 3) The box counting method is not able to pick up the negative dimensions corresponding to the negative $f(\alpha)$ that may result from a shift. Hence, where the intersection of the tangent to $\beta(q)$ and the β -axis is close to 0, the slice hypothesis cannot be expected to apply.

In conclusion, the computational evidence, using approximations to slices by narrow strips, suggests that the slice hypothesis may be a fair assumption to make if μ has a large support and is reasonably homogeneous and isotropic.

5.5 The slice hypothesis and rainfall analysis

5.5.1 Introduction

As pointed out in section 3.2, in order to improve GCMs (General circulation models) information about the sub-grid variability of precipitation is required. In section 1.4.1 we refer to evidence that self-similar random cascade measures provide adequate approximations of spatial and temporal rainfall distributions. In section 3.4.1 we test the rainfall disaggregation by random cascade processes against conventional parametric rainfall disaggregation and observed rainfall distributions. In chapter 4 the problem of determining random cascade parameters to match desired multifractal properties is considered. An outstanding problem is how to estimate these multifractal properties empirically. It would, for example, be useful to know the multifractal properties of different rainfall types to enable adjustment of the rainfall generating process in a climate model.

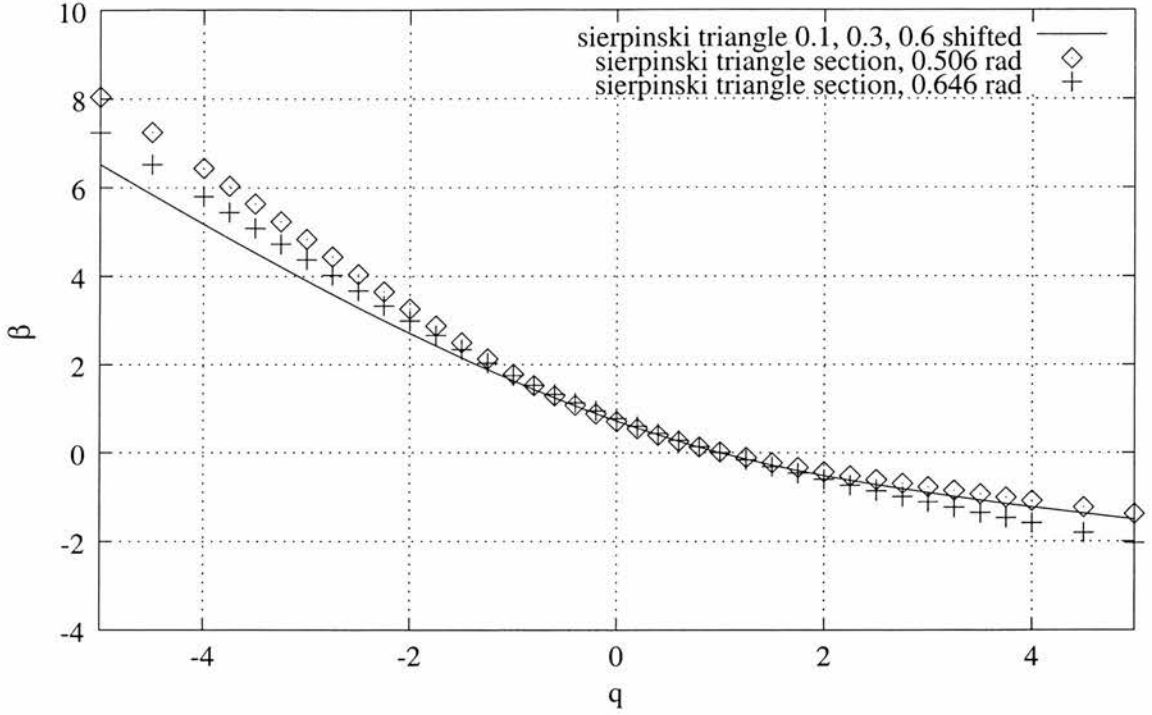


Figure 5.15: $\beta(q)$ of the generalised Sierpiński triangle measure *GT1* for slices at angles $\phi = 0.506$ rad and $\phi = 0.646$ rad, according to the slice hypothesis and estimated by box-counting

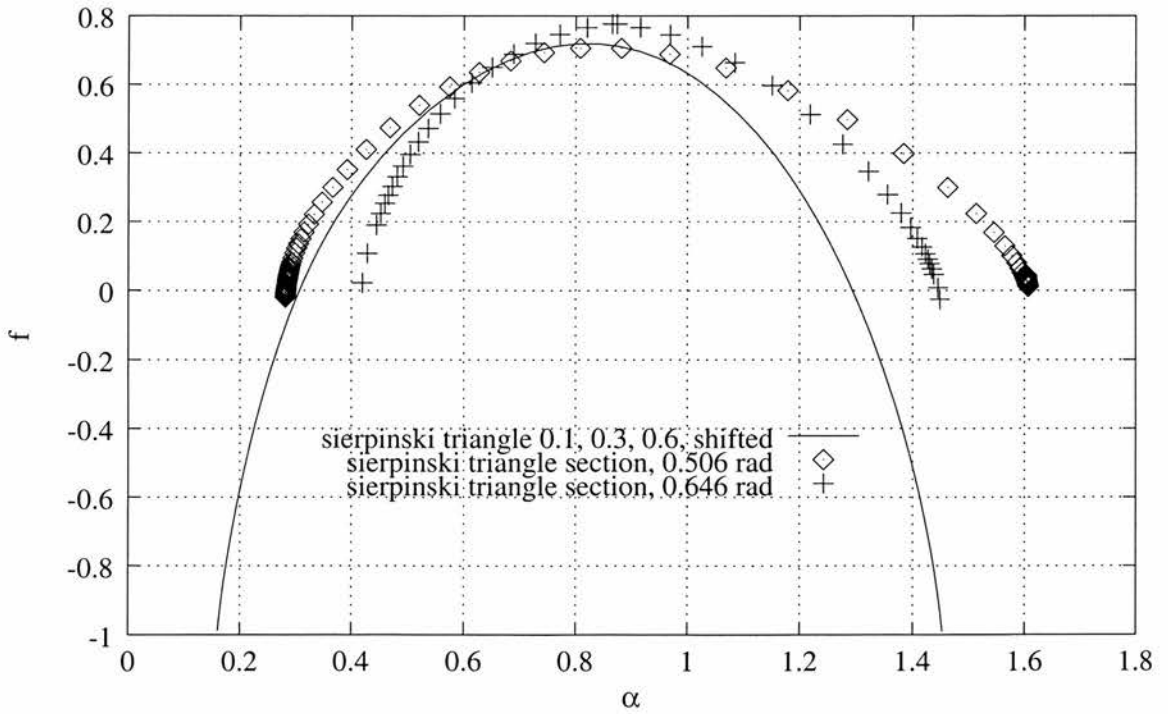


Figure 5.16: $f(\alpha)$ of the generalised Sierpiński triangle measure *GT1* for slices at angles $\phi = 0.506$ rad and $\phi = 0.646$ rad, according to the slice hypothesis and estimated by box-counting

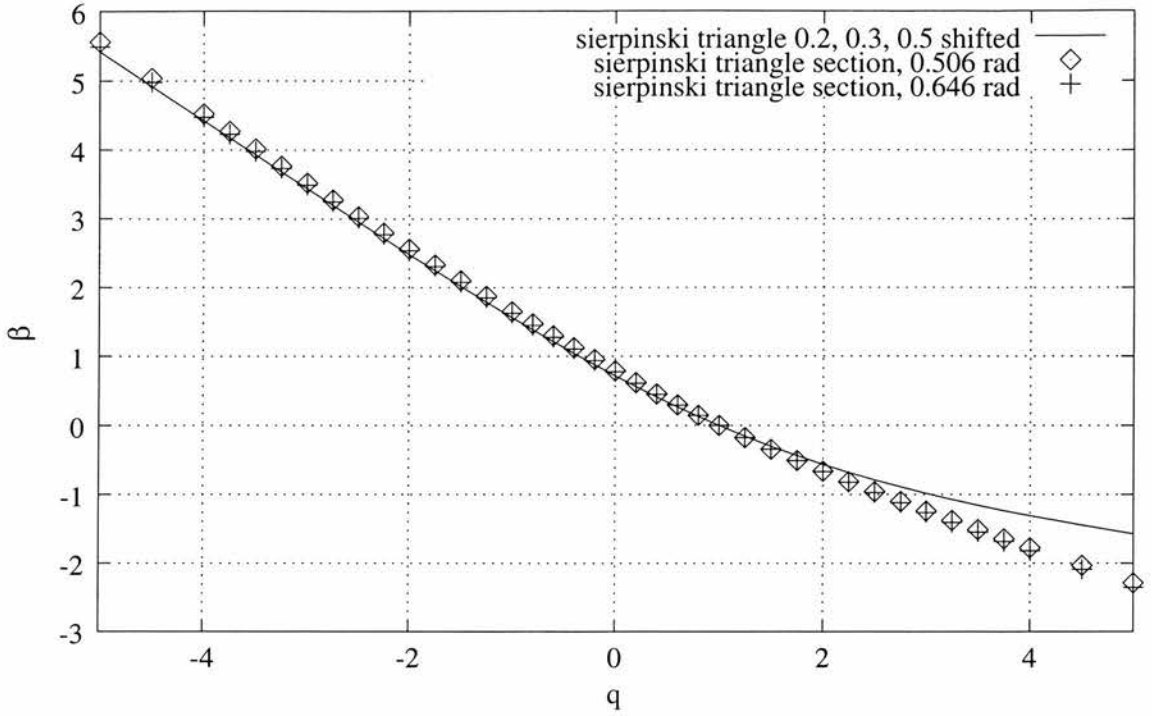


Figure 5.17: $\beta(q)$ of the generalised Sierpiński triangle measure $GT2$ for slices at angles $\phi = 0.506$ rad and $\phi = 0.646$ rad, according to the slice hypothesis and estimated by box-counting

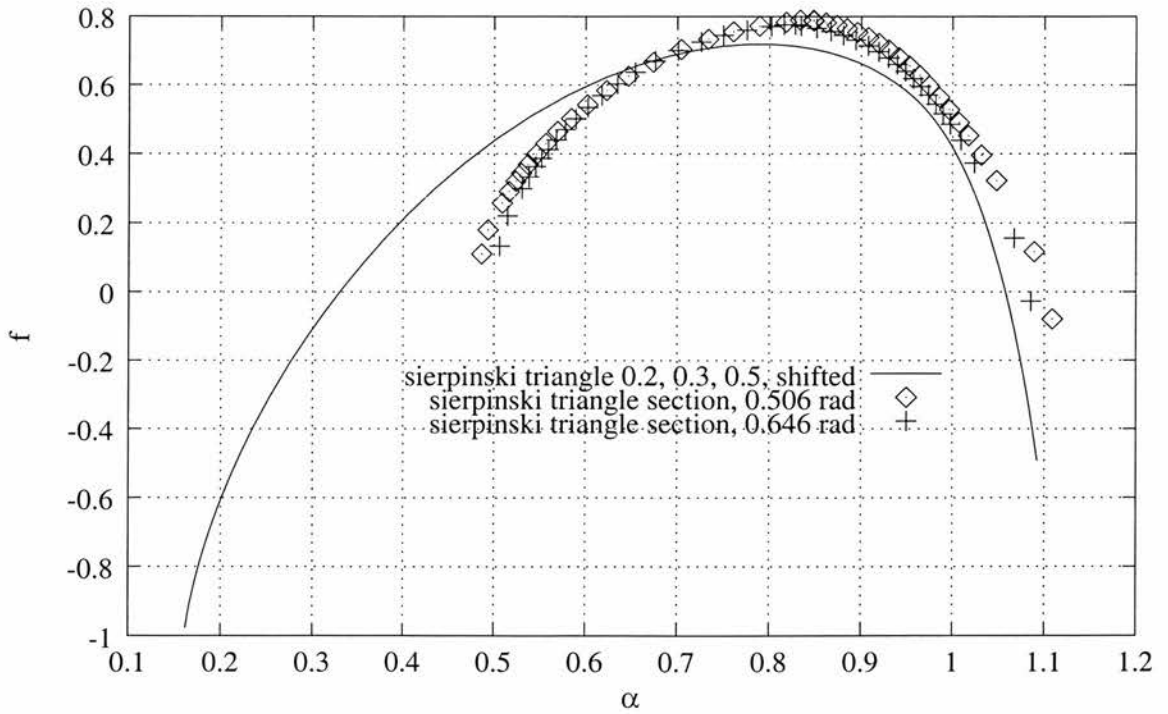


Figure 5.18: $f(\alpha)$ of the generalised Sierpiński triangle measure $GT2$ for slices at angles $\phi = 0.506$ rad and $\phi = 0.646$ rad, according to the slice hypothesis and estimated by box-counting

The most common method for recording spatial rainfall distributions is by weather radar. But even from a single high resolution radar image it is hard to obtain enough information to do reasonable multifractal analysis. Typical spatial rainfall distribution data, measured from rainfall radar, is awkward to analyse using box-counting, because of the low resolution, which is typically a 64x64 or 128x128 grid of 2km or 4km squares. This does not generally provide enough information to compute the multifractal spectrum reliably using box-counting.

A possible improvement might be obtained by using radar composites, such as the NEXRAD WSR-88D radars covering the majority of the USA, which report to the National Center for Environmental Prediction. These radar composite images consist of up to 100 individual radar images which are calibrated and combined on a 1160x880 polar stereographic grid of 4km squares, see figure 5.19. Some radar stations may not operate

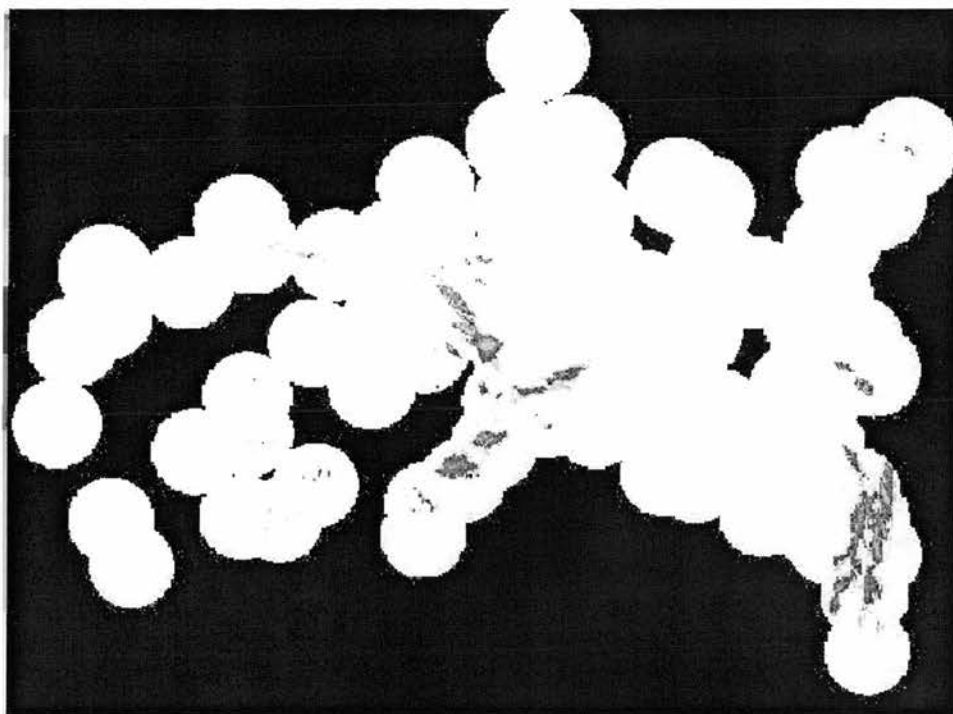


Figure 5.19: Typical spatial rainfall radar image composite, 02/05/1997, 01:00

at all times and the area covered is not rectangular. The most suitable composite radar images gained from NEXRAD WSR-88D radars give a 512x512 grid of 4km squares, see figure 5.20. A direct attempt to find the auxiliary function and the multifractal spectrum for this grid gives the graphs shown in figures 5.21 to 5.26. But even with data of this size, getting reliable information about the multifractal properties of the rainfall distribution is not easy. As we have seen in section 1.3.4 sample size is a crucial factor for the box-counting algorithms to work reliably. Since the size of the spatial rainfall data is several orders of magnitudes smaller than the size of the data used in the previous section, we expect the outcome of the box-counting algorithms to be less precise in this case.

A possible way of overcoming the problems that arise from the poor quality and limited availability of spatial rainfall data is to use the slice hypothesis. Under the assumption that rainfall distributions are results of atmospheric turbulences that can be modelled by self-similar random cascade measures, see section 1.4.1, and that the slice hypothesis

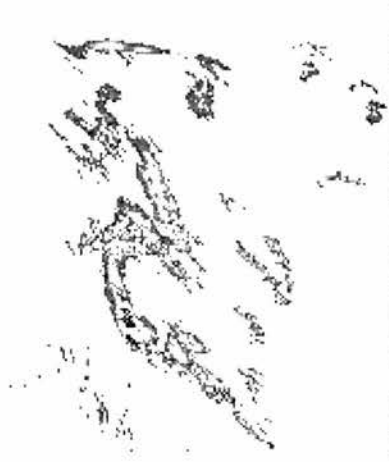


Figure 5.20: Spatial rainfall data, showing detail from the radar composite

holds for such measures, see section 5.4.4, it is plausible that the slice hypothesis holds for rainfall data.

We investigate applying the slice hypothesis in two different ways: firstly by taking a slice directly from the composite radar images, and secondly by assuming that a rainfall time series at a point of observation is a typical section of the spatial rainfall distribution sampled as it moves over the point of observation.

5.5.2 Slice of a radar composite

We compare the multifractal auxiliary function and the spectrum of a slice of a radar composite image and of a square area of the same image. Because of the shape of the composite, we can choose a slice of greater length than an individual radar image. The slice has a length of 1024 boxes and its width is of the same order of magnitude as its box-length.

The spatial data for the analysis presented here was taken on the 03/12/1997 at 13:00. Similar results were gained from the analysis of other spatial images. Figures 5.21 and 5.22 show the multifractal auxiliary function and spectrum of the spatial rainfall distribution indicated in figure 5.20 shifted according to the slice hypothesis, and those of a slice of this distribution. We observe that there is poor agreement between the graphs obtained by analysing the slice of the composite image and the shifted graphs, obtained by analysing the square area of the composite. Considering the conclusions of the standard examples, contributing factors are likely to include the small support of the distribution, the limited number of boxes used, and the lack of homogeneity and isotropy of the distributions.

5.5.3 Temporal observations at a fixed site

High frequency temporal data of a rain gauge at a given site can be of a much finer scale than the spatial data that is available from a rainfall radar. If one makes the simplistic assumption that a rainfall field is constant except that it is moving at a constant velocity, then the rainfall intensity at a fixed rain gauge represents the rainfall intensity along a slice of the system parallel to the direction of motion. Thus there might be a case for regarding temporal rainfall observations at a fixed site as a slice of the spatial distribution.

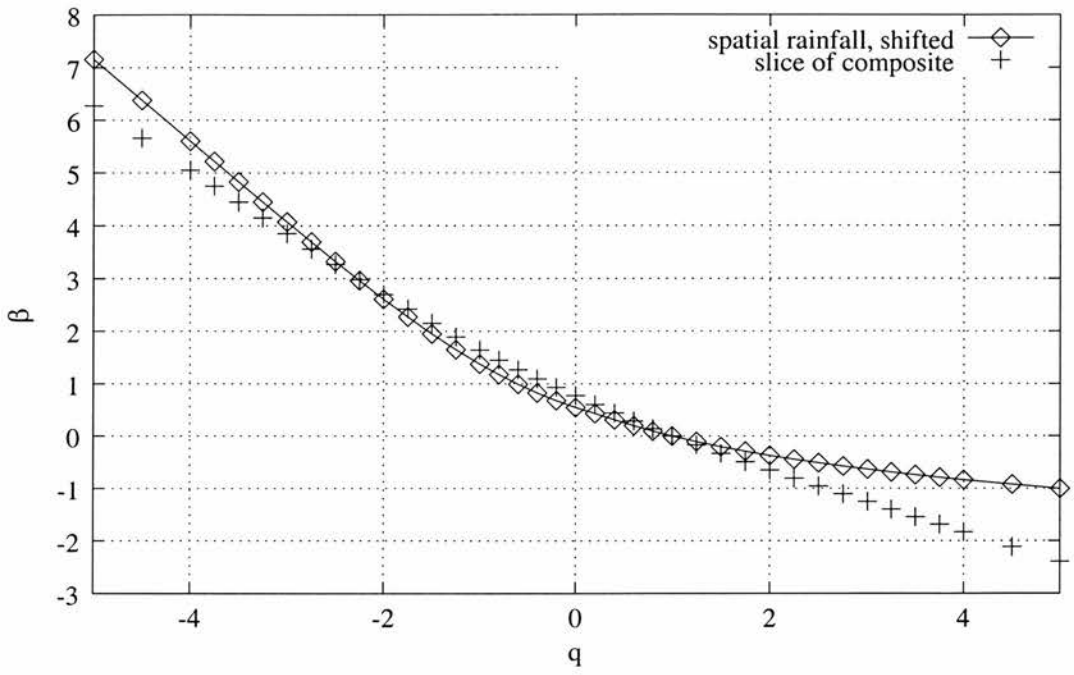


Figure 5.21: $\beta(q)$ of the spatial rainfall data, shifted according to the slice hypothesis, and of the slice

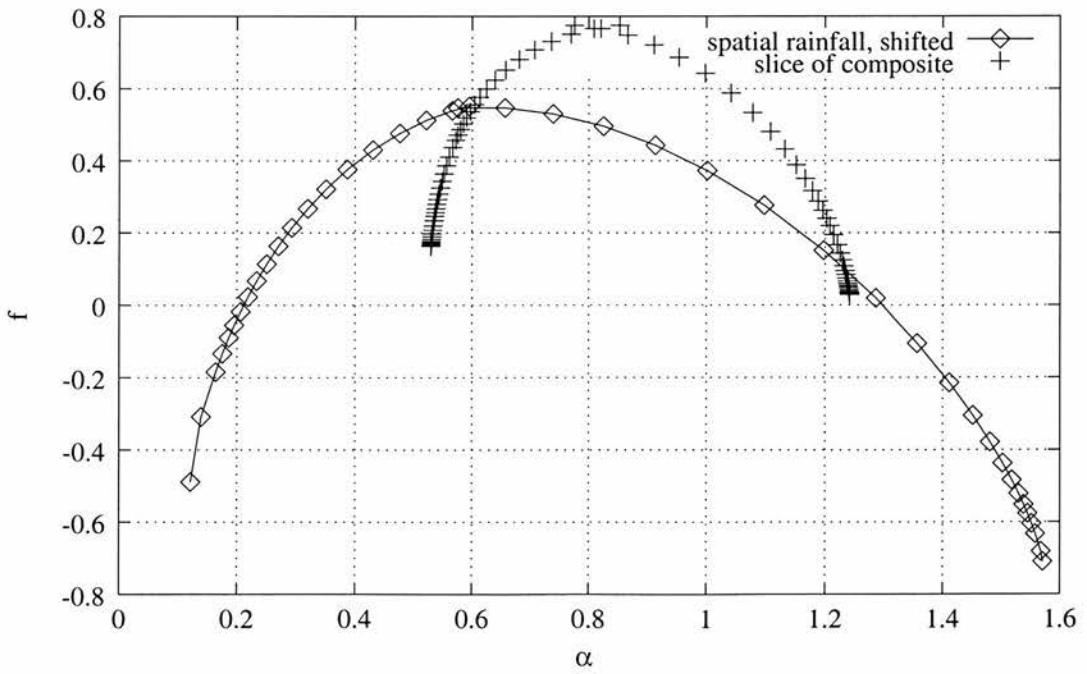


Figure 5.22: $f(\alpha)$ of the spatial rainfall data, shifted according to the slice hypothesis, and of the slice

There are some obvious difficulties with this assumption. The overall rainfall pattern develops in a much more complex way than just a translation with time. Geographical features such as hills or lakes can have effects which will not be picked up at a distant fixed site. A slice of a rainfall field parallel to the direction of motion is a special slice with features that may well not be typical. A system generally moves along a curved path rather than along a straight line. (This effect is probably not relevant for the analysis, since multifractal features of a distribution are invariant under smooth distortions, so a slice by a ‘smooth curve’ is likely to be as effective as a slice by a line.)

Despite the difficulties, there is the undoubted advantage that it is possible to obtain much finer data using temporal readings. For a system moving 5km/h readings every 5 minutes at a fixed site correspond to readings at spatial intervals of the order of 0.5km and in principle there is no reason why readings should not be made at even shorter intervals. On the other hand time series are available for long periods of time, corresponding to spatial scales much larger than those that can be observed by radar or satellite.

To investigate this we compare the multifractal auxiliary function and spectrum from spatial and temporal data. Two examples are presented here. First we compare the multifractal functions of spatial rainfall distributions taken at two different times on 03/12/1997 with those of temporal data taken by a tipping bucket rain gauge in Columbia, Missouri, in the area of this storm, at 5min intervals, from 28/11/1997, 06:15 to 05/12/1997, 08:55, see figures 5.23 and 5.24. Figures 5.25 and 5.26 show the multifractal auxiliary function

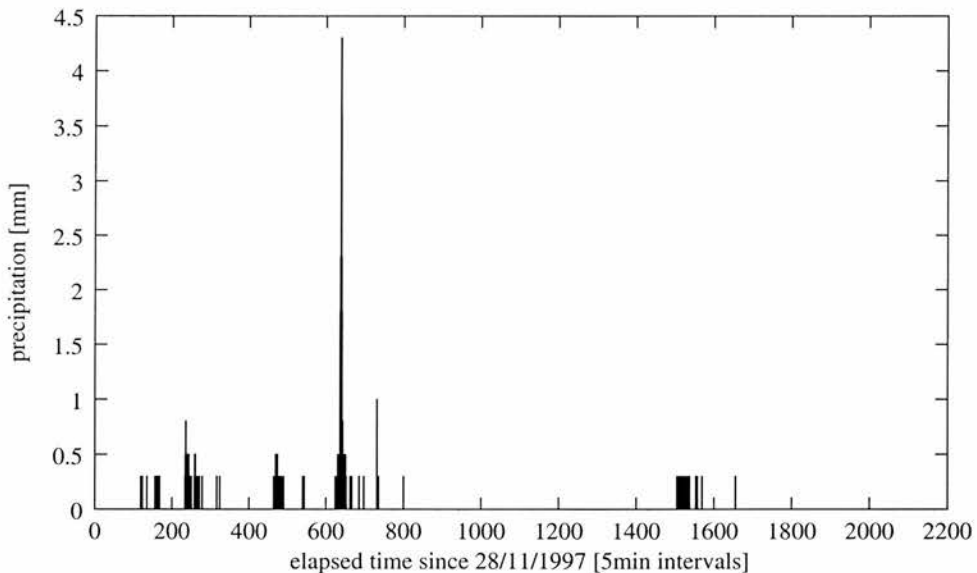


Figure 5.23: Temporal rainfall data, 5min intervals from 28/11/1997 to 5/12/1997

and spectrum of the spatial rainfall distribution in figure 5.20, shifted according to the slice hypothesis, and of the rainfall time series.

In the second example we compare the multifractal functions of spatial data taken on 03/05/1997 at 00:00 with those of temporal data taken by a tipping bucket rain gauge in Rosemount, Minnesota, in the area of the storm, at 30min intervals, from 01/10/1996 to 19/06/1997, see figures 5.27 and 5.28.

In both cases there is a surprisingly good correspondence between the auxiliary functions and multifractal spectra of the spatial data, shifted according to the slice hypothesis, and those of the temporal data for positive q . For negative q the Legendre transform $f(\alpha)$ of the temporal data falls off very rapidly. This is due to the cut-off effect resulting from the use of tipping bucket rain gauges, see section 1.3.3. In the second example the resolution of the temporal data is coarser than in the first example and the time span covered

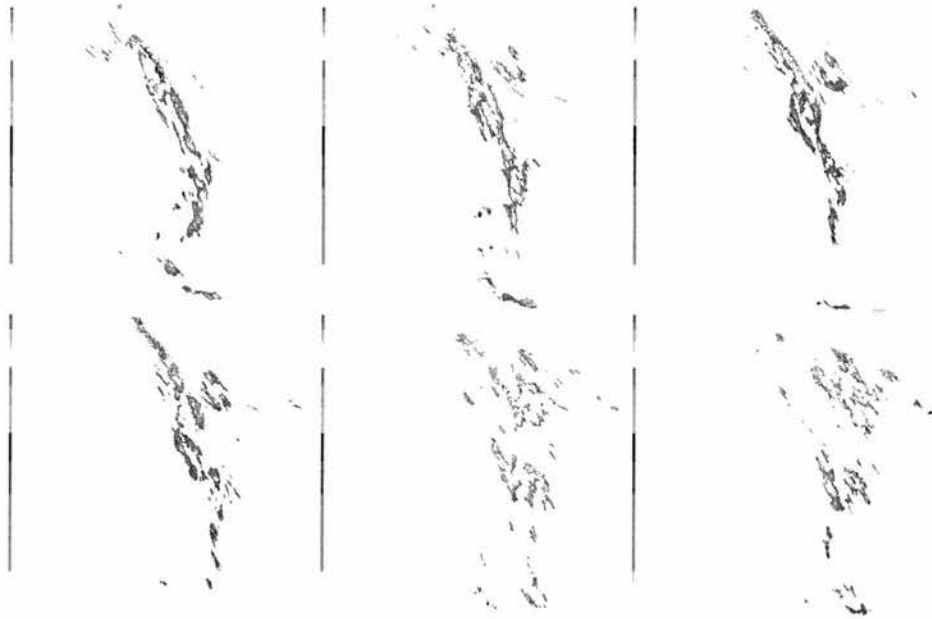


Figure 5.24: Spatial rainfall distributions on 03/12/1997 from 13:00 to 18:00 at hourly intervals

by the data cannot be compared to an observable length scale of spatial data.

5.5.4 Discussion

Of the two methods of applying the slice hypothesis to rainfall data, the approach taking readings at a fixed rain gauge appears to give better results in our experiments, and might be a basis for estimating multifractal parameters.

Nevertheless, consideration should be given to whether the rainfall distribution is of the type of data for which the slice hypothesis is valid. The shape of rainfall distributions is either determined by local phenomena, such as small-scale hydrological or convective processes, or by large scale phenomena, causing for example frontal rainfall.

In the case of frontal rainfall the overall system is translated with time. The translational changes in the distribution are more significant than those caused by variations in temperature, pressure etc. induced by geographical features. Thus in this case, the underlying assumption that the temporal data at a fixed site corresponds to a slice of the spatial rainfall field is not unreasonable. One shall be aware that a slice obtained this way may be atypical since it is parallel to the direction of translation of the rainfall field. Nevertheless, any distortion caused by this effect is lessened if the rainfall field itself is reasonably isotropic.

In the case of convective rain one might doubt that the temporal data represents a slice, since the change in the rain field is mainly caused by complex local and small-scale hydrological processes and to a lesser degree by translation.

From examining the standard examples in section 5.4 we find that the slice hypothesis is most appropriate for distributions that are homogeneous and isotropic. Hence the approach using temporal data may be most appropriate for rainfall biased towards frontal rainfall where the non-translational changes are smooth.

It might be worthwhile using temporal data of a higher resolution, thus avoiding the cut-off effect, although this only has a significant effect for negative q , corresponding to regions of very sparse density with little importance for hydrological applications.

This suggests that, despite the simplistic assumption relating the temporal data and

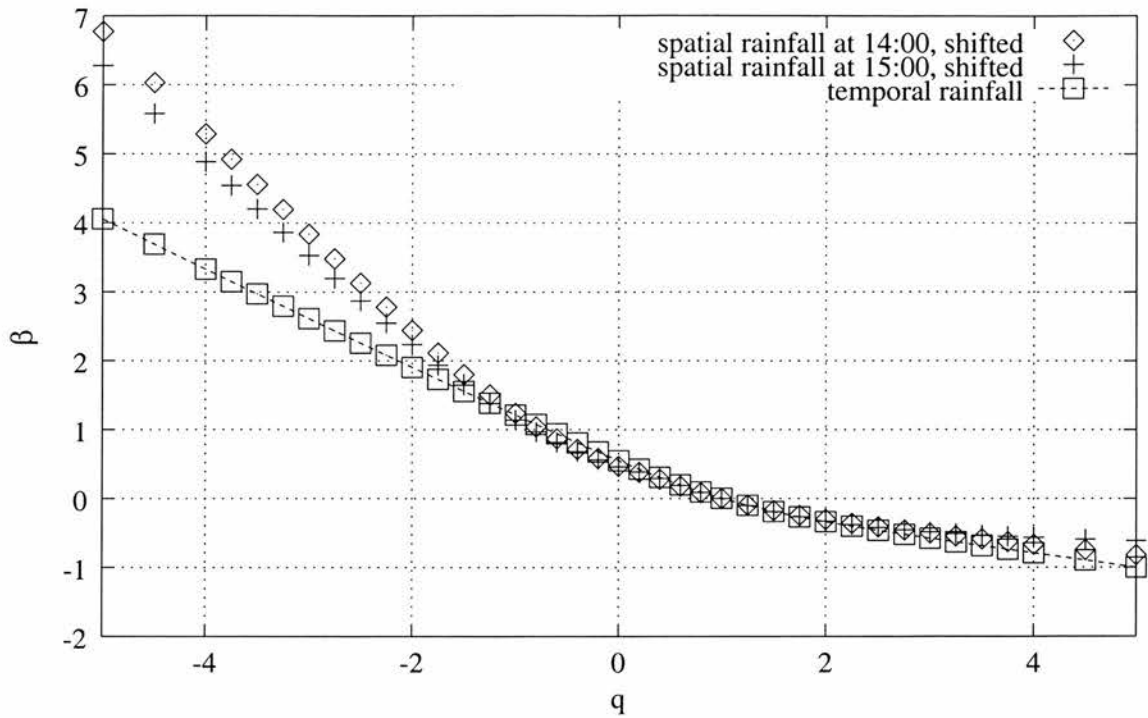


Figure 5.25: $\beta(q)$ of spatial rainfall data, shifted according to the slice hypothesis and of rainfall time series, December 1997

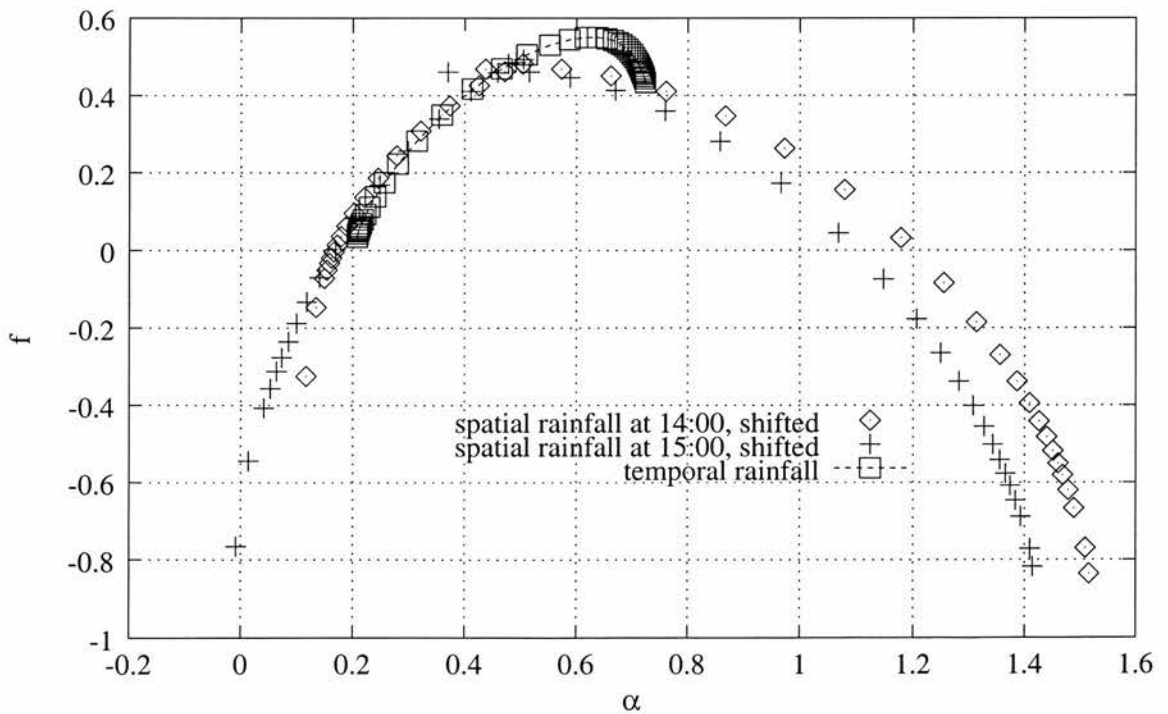


Figure 5.26: $f(\alpha)$ of spatial rainfall data, shifted according to the slice hypothesis and of rainfall time series, December 1997

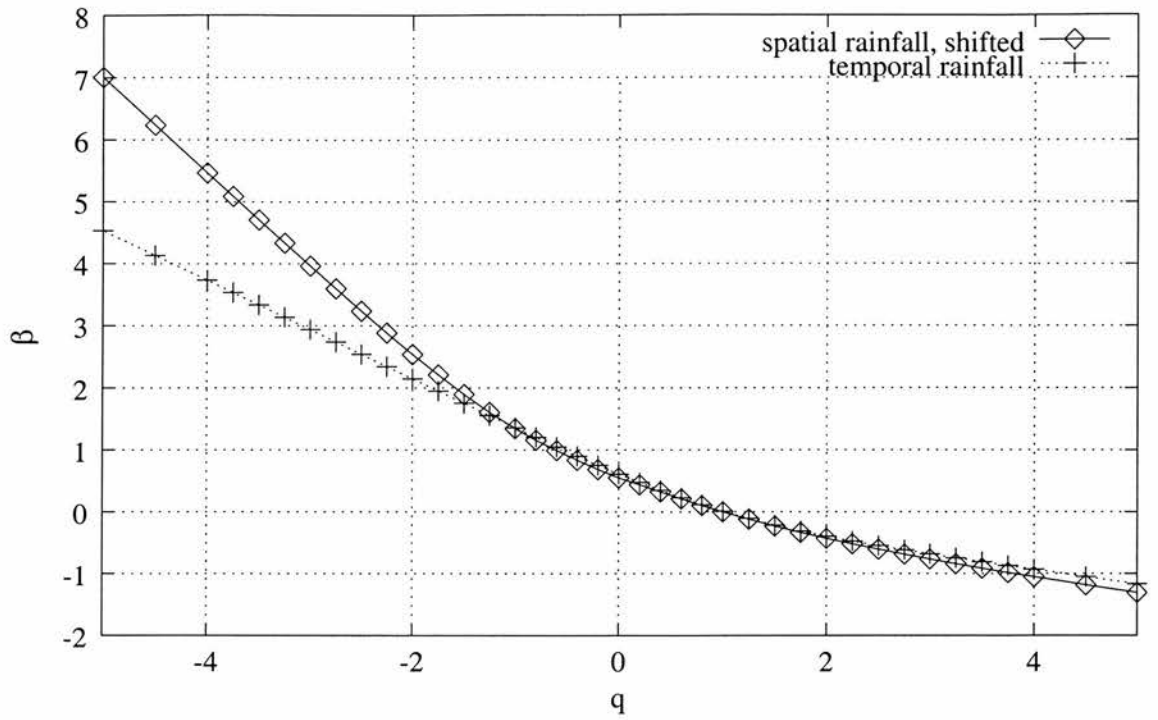


Figure 5.27: $\beta(q)$ of spatial rainfall data, shifted according to the slice hypothesis and of rainfall time series, May 1997

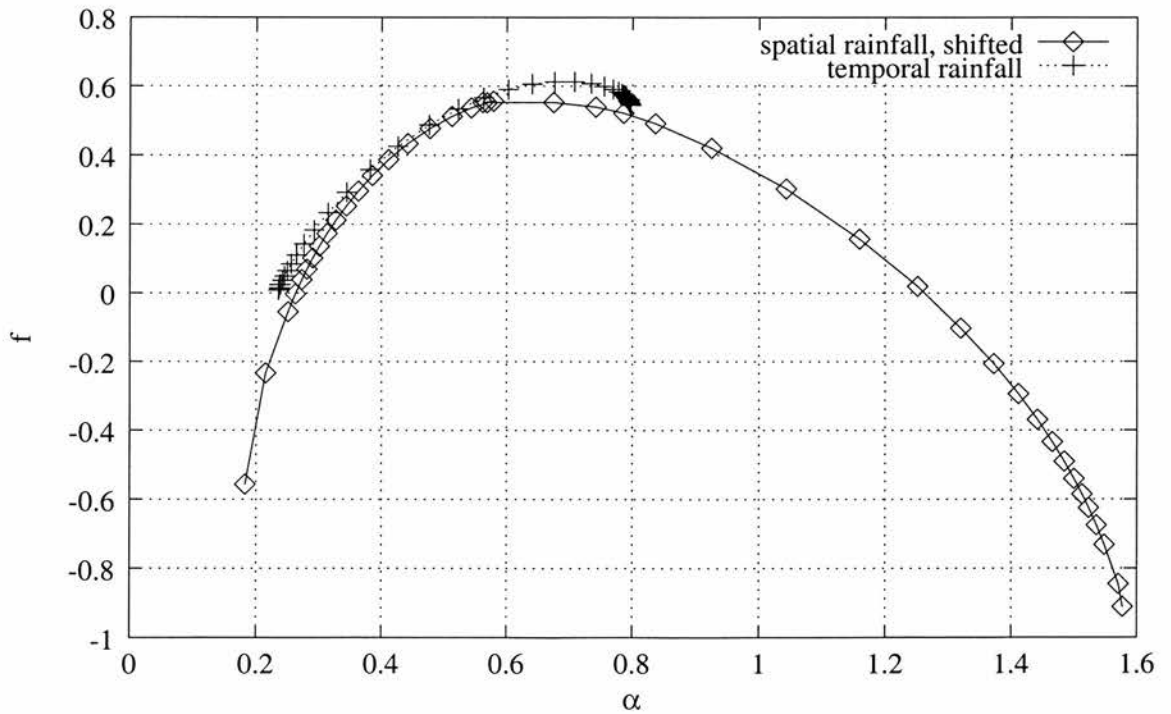


Figure 5.28: $f(\alpha)$ of spatial rainfall data, shifted according to the slice hypothesis and of rainfall time series, May 1997

spatial data, being able to work with finer data may make this approach worthwhile. In particular it might be used for determining appropriate random cascades with multifractal properties of spatial rainfall distributions by using the schemes described in chapter 4. These random cascades might be used for modelling rainfall, as in chapter 3.

There is scope for considerably more work in this direction. Much finer data needs to be analysed to determine which time and length scales are relevant for relating multifractality of spatial and temporal data in this way. If this can be progressed, it might lead to a usable approach for deducing key rainfall features to be used in applications such as rainfall modelling and in particular disaggregation of precipitation in simulations as in chapter 3.

Chapter 6

Conclusions

We summarise the main points raised in the thesis. Interconnections between the different chapters are emphasised and open problems are considered.

In this thesis the multifractal properties of rainfall were studied. The general background on multifractal theory and its connections to rainfall analysis were described in chapter 1. Basic definitions of fractals and fractal dimension, in particular box-counting and Hausdorff dimension, were given, followed by an introduction into multifractal analysis with definitions of the fine, coarse and Legendre transform multifractal spectra. The multifractal properties of some well-known measures were examined; with random cascades of particular interest. A way of generating these measures was presented and their Legendre transformation spectra were calculated. In the third section algorithms for calculating the Legendre transform spectrum were calculated. Different algorithms for use on discrete data and on data supported by a mesh were compared. Some preliminary results of box-counting algorithms on some well-known multifractal measures were given in order to assess which methods are most suitable for multifractal analysis of rainfall distributions.

In the fourth section the motivation for applying multifractal analysis to hydrological problems was given. The main motivation for this research was the need to find novel and more realistic methods of describing rainfall distributions in climate modelling. A review of hydrological literature relating to multifractals, in particular random cascade measures, was given. The discrepancy between the scales of typical rainfall distributions found by measurements and those realised in modelling is described and problems arising from this discrepancy were discussed. Finally a justification of using random cascade measures to rainfall disaggregation in climate modelling was given.

In the second chapter a self-affine variant of the Sierpiński triangle and an invariant measure supported by this set were introduced. The box dimension of the self-affine Sierpiński triangle and in certain cases the auxiliary function and the Legendre multifractal spectrum of the measure were determined. This was done to provide a new example for analysis and to provide a non-self-similar example on which to test algorithms for experimental determination of multifractal spectra. This example was also used on the work on sections in chapter 5.

In chapter 3 possibilities of using multifractal random cascade measures for disaggregating rainfall in climate simulations were examined. A random cascade disaggregation of spatial rainfall was incorporated into the one-dimensional hydrological component of the UK Meteorological Office Surface Exchange Scheme (MOSES) used in their General Circulation Model (GCM). The changes in the water balance, in particular the throughfall and the evaporation from the canopy were assessed. It was shown that a disaggregation using random cascades gave closer values to the reference simulation of canopy evaporation and throughfall variables than the conventional approach. In addition this chapter provided

novel insights into the effects of incorporating spatial memory on the water balance.

The random cascades used depend on a number of parameters. Therefore it is desirable to choose these parameters in such a way that the resulting mass distributions and real-life rainfall distributions have similar multifractal properties. Spatial rainfall data detailed enough for multifractal analysis is not widely available. In the last two chapters possible solutions of these two problems were indicated: firstly schemes were developed for creating cascades with given specific multifractal properties (chapter 4), then a novel method for finding multifractal properties of spatial rainfall distribution by analysing temporal readings was proposed (chapter 5).

In chapter 4 the dependance of multifractal properties of random cascades on their cascade parameters were examined and ways of estimating appropriate random cascade parameters were proposed. Several novel schemes for estimating cascade parameters from given multifractal functions were described. The feasibility of these schemes was tested by replicating the multifractal properties of some well-known multifractal measures by random cascades. Finally the multifractal properties of a rainfall field were replicated by a random cascade.

In chapter 5 the relationship between the multifractal functions of a plane measure and those of sections of the measure by a line was discussed. Utilising recent mathematical ideas about this relationship and by approximating the section by a thin slice we formulated the “slice hypothesis”. By examining a theoretical example we discussed certain limitations of the slice hypothesis. We computed the multifractal functions of several well-known self-similar and self-affine measures and their slices. By comparing them we validated the slice hypothesis under certain conditions. The slice hypothesis may be used to estimate multifractal properties of spatial rainfall fields by analysing rainfall data representing slices of rainfall fields. We suggested that rainfall time series and slices of composite radar images might suffice for this purpose. This was confirmed by examining field data from a radar composite in the USA and an appropriate time series.

This work is on the borderline of two massively complex topics: multifractal analysis and climate simulation. Hence it is not surprising that, although some progress on the use of multifractal analysis in this area was made, many questions are left open and a number of problems still need to be solved. The computations in chapter 3 showed that the price for achieving better results in simulating the water balance equations is an increase in computing time and memory consumption. By optimising the disaggregation algorithm improvements would be possible. One such improvement could be achieved by a parametrised disaggregation using multifractal functions rather than performing cascade disaggregation. On the other hand spatial memory, that is information about the spatial distribution of the water balance variables, would not be preserved in this approach. Another open question is the choice of cascade parameters in the simulation. It would be useful to have a library of parameters for each major storm type. For this a thorough multifractal analysis of different storms would be necessary. The results of chapter 5 would be helpful in generating such a library. For this, finer temporal data would be necessary and more work on the comparison of multifractal functions of spatial and temporal data would need to be done. The effect of disaggregation on the water balance with different canopies such as grass or rainforest could be analysed in order to assess the changes in the water balance on the whole area of GCM, which of course is not covered homogeneously by just one type of canopy. In chapter 4 it was found that there are certain multifractal measures for which we cannot find random cascade measures with identical multifractal properties. For practical applications it is probably not necessary to find random cascades with absolutely matching multifractal properties. Therefore it would be desirable to know how closely a given multifractal function can be approximated by that of a random cascade measure. Further, other classes of random cascades might be considered that could give

rise to new schemes of finding random cascades with specific multifractal features.

Bibliography

- M. Alber. Improved multifractal box-counting algorithm, virtual phase transitions and negative dimensions. *Physical Review E*, 57:5489–5493, 1998.
- M. Arbeiter and N. Patzschke. Random self-similar multifractals. *Mathematische Nachrichten*, 181:5–42, 1996.
- R. Badii and G. Broggi. Measurement of the dimension spectrum $f(\alpha)$: Fixed-mass approach. *Physics Letters A*, 131:339–343, 1988.
- R. Badii and A. Politi. Hausdorff dimension and uniformity factor of strange attractors. *Physical Review Letters*, 52:1661–1664, 1984.
- S. Borgani, G. Murante, A. Provenzale, and R. Valdarnini. Multifractal analysis of the galaxy distribution: Reliability of results from finite data sets. *Physical Review E*, 47:3879–3888, 1993.
- W. E. Caswell and J. A. Yorke. Invisible errors in dimension estimates. In G. Mayer-Kress, editor, *Dimensions and Entropies in Chaotic Systems*. Springer, 1986.
- A. J. Dolman and D. Gregory. The parametrization of rainfall interception in GCMs. *Quarterly Journal of the Royal Meteorological Society*, 118:455–467, 1992.
- I. J. Dwyer and D. W. Reed. Effective fractal dimension and corrections to the mean of annual maxima. *Journal of Hydrology*, 157:13–34, 1994.
- E. A. B. Eltahir and R. L. Bras. A description of rainfall interception over large areas. *Journal of Climate*, 6:1002–1008, 1993a.
- E. A. B. Eltahir and R. L. Bras. Estimation of the fractional coverage of rainfall in climate models. *Journal of Climate*, 6:639–644, 1993b.
- D. Entekhabi and P. S. Eagleson. Land surface hydrology parameterization for atmospheric general circulation models including subgrid scale spatial variability. *Journal of Climate*, 2:816–831, 1989.
- C. J. G. Evertsz and B. B. Mandelbrot. Multifractal measures. In *Chaos and Fractals - New Frontier of Science*, pages 921–953. Springer Verlag, 1992.
- K. J. Falconer. *Fractal Geometry - Mathematical Foundations and Applications*. John Wiley, 1990.
- K. J. Falconer. The dimension of self-affine fractals II. *Mathematical Proceedings of the Cambridge Philosophical Society*, 111:169–179, 1992.
- K. J. Falconer. Probabilistic methods in fractal geometry. *Progress in Probability*, 37:3–13, 1995.

- K. J. Falconer. *Techniques in Fractal Geometry*. John Wiley, 1997.
- K. J. Falconer and B. Lammering. Fractal properties of generalized Sierpiński triangles. *Fractals*, 6:31–41, 1998.
- K. J. Falconer and D. T. Marsh. The dimension of affine-invariant fractals. *Journal of Physics A*, 21:L121–L125, 1988.
- K. J. Falconer and T. C. O’Neil. Convolutions and the geometry of multifractal measures. *Mathematische Nachrichten*, 204:61–82, 1999.
- P. Grassberger and I. Procaccia. Characterization of strange attractors. *Physical Review Letters*, 50:346–349, 1983.
- D. Gregory and R. N. B. Smith. *Unified Model Documentation Paper 25: Canopy, surface and soil hydrology*. UK Meteorological Office, 1st edition, 1990.
- G. Grimmett and D. Stirzaker. *Probability and Random Processes*. Oxford University Press, 1982.
- V. K. Gupta and E. Waymire. Multiscaling properties of spatial rainfall and river flow distributions. *Journal of Geophysical Research*, 95:1999–2009, 1990.
- V. K. Gupta and E. C. Waymire. A statistical analysis of meoscale rainfall as a random cascade. *Journal of Applied Meteorology*, 32:251–267, 1993.
- T. C. Halsey, M. H. Jensen, L. P. Kadanoff, I. Procaccia, and B. I. Shraiman. Fractal measure and their singularities: The character of strange sets. *Physical Review A*, 33: 1141–1151, 1986.
- A. Henderson-Sellers and A. Pitman. Vegetation and climate interactions in semiarid regions - introduction. *Vegetatio*, 91:R9, 1991.
- H. E. Hurst, R. P. Black, and Y. M. Simaika. *Long-term Storage: An Experimental Study*. Constable, 1965.
- K. D. Johnson, D. Entekhabi, and P. S. Eagleson. The implementation and validation of improved land-surface hydrology in an atmospheric circulation model. *Journal of Climate*, 6:1009–1026, 1993.
- J. King. The singularity spectrum for general Sierpinski carpets. *Advances in Mathematics*, 116:1–11, 1995.
- A. N. Kolmogorov. Local structure of turbulence in an incompressible liquid for very large reynolds optnumbers. *Proceedings of the Academy of Science, USSR., Geochemical Section*, 30:199–303, 1941.
- P. Kumar and E. Foufoula-Georgiou. A multicomponent decomposition of spatial rainfall fields 1. segregation of large- and small-scale features using wavelet transforms. *Water Resources Research*, 29:2515–2532, 1993a.
- P. Kumar and E. Foufoula-Georgiou. A new look at rainfall fluctuations and scaling properties of spatial rainfall using orthogonal wavelets. *Journal of Applied Meteorology*, 32:209–222, 1993b.
- B. Lammering. Slices of multifractal measures and applications to rainfall distributions. Technical report, accepted by *Fractals*, to appear in Dec., 2000.

- B. Lammering and I. J. Dwyer. Improvement of water balance in land surface schemes by random cascade disaggregation of rainfall. *International Journal of Climatology*, 20: 681–695, 2000.
- S. Lovejoy. The statistical characterization of rain areas in terms of fractals. In *Proceedings of the 20th Conference on Radar Meteorology*, pages 476–483. American Meteorological Soc., 1981.
- S. Lovejoy. Area-perimeter relation for rain and and cloud areas. *Science*, 216:185–187, 1982.
- S. Lovejoy and B. B. Mandelbrot. Fractal properties of rain, and a fractal model. *Tellus*, 37A:209–232, 1985.
- S. Lovejoy and D. Schertzer. Fractals, rain drops and resolution dependence of rain measurements. *Journal of Applied Meteorology*, 29:1167–1170, 1990a.
- S. Lovejoy and D. Schertzer. Multifractals, universality classes and satellite and radar measurements of cloud and rain fields. *Journal of Geophysical Research*, 95:2021–2034, 1990b.
- S. Lovejoy and D. Schertzer. Multifractals and rain. In A. W. Kundzewicz, editor, *New Uncertainty Concepts in Hydrology and Hydrological Modelling*, pages 62–103. Cambridge University Press, 1995.
- J. Mach, F. Mas, and F. Sagués. Two representations in multifractal analysis. Universitat de Barcelona, January 1996.
- B. B. Mandelbrot. Intermittent turbulence in self-similar cascades: divergence of high moments and dimension of the carrier. *Journal of Fluid Mechanics*, 62:331–358, 1974.
- B. B. Mandelbrot. Negative dimensions and multifractals. *Physica A*, 163:306–315, 1990.
- B. B. Mandelbrot. Random multifractals: negative dimensions and the resulting limitations of the thermodynamic formalism. *Proceedings of the Royal Society of London A*, 434:79–88, 1991.
- B. B. Mandelbrot. Negative dimensions and Hölders, multifractals and their Hölder spectra, and the role of lateral preasymptotics in science. In *The Journal of Fourier Analysis and Applications - Kahane Special Issue*, pages 409–432. CRC-Press, 1995.
- B. B. Mandelbrot, C. J. G. Evertsz, and Y Hayakawa. Exactly self-similar left-sided multifractal measures. *Physical Review A*, 42:4528–4536, 1990.
- B. B. Mandelbrot and J. R. Wallis. Noah, Joseph, and operational hydrology. *Water Resources Research*, 4:909–918, 1968.
- B. B. Mandelbrot and J. R. Wallis. Computer experiments with fractional gaussian noises. *Water Resources Research*, 5:228–259, 1969.
- D. Marsan, D. Schertzer, and S. Lovejoy. Causal space-time multifractal processes: Predictability and forecasting of rain fields. *Journal of Geophysical Research*, 101:26333–26346, 1996.
- V. J. Martinez, B. J. T. Jones, R. Dominguez-Tenreiro, and R. van de Weygaert. Clustering paradigms and multifractal measures. *Astrophysics Journal*, 357:50–61, 1990.

- P. Mattila. *Geometry of Sets and Measures in Euclidean Spaces*. Cambridge University Press, 1995.
- J. L. McCauley. *Chaos, Dynamics and Fractals*. Cambridge University Press, 1993.
- L. Olsen. A multifractal formalism. *Advances in Mathematics*, 116:82–196, 1995.
- L. Olsen. Geometric constructions in multifractal geometry. *Periodica Mathematica Hungarica*, 37:81–99, 1998a.
- L. Olsen. Self-affine multifractal Sierpinski sponges in \mathbb{R}^d . *Pacific Journal of Mathematics*, 183:143–199, 1998b.
- L. Olsen. Multifractal geometry. *Progress in Probability*, 46, 2000.
- J. Olsson. *Scaling and Fractal Properties of Rainfall*. PhD thesis, Lund University, 1996a.
- J. Olsson. Temporal rainfall disaggregation by a multiplicative random cascade model. manuscript, 1996b.
- J. Olsson. Evaluation of a scaling cascade model for temporal rainfall disaggregation. *Hydrology and Earth System Science*, 2:19–30, 1998.
- C. Onof, P. Northrop, H. S. Wheater, and V. Isham. Spatiotemporal storm structure and scaling property analysis for modeling. *Journal of Geophysical Research*, 101:26415–26425, 1996.
- C. Onof and H. S. Wheater. Analysis of the spatial coverage of British rainfall fields. *Journal of Hydrology*, 176:97–113, 1996.
- T. M. Over and V. K. Gupta. Statistical analysis of mesoscale rainfall: Dependence of a random cascade generator on large-scale forcing. *Journal of Applied Meteorology*, 33:1526–1542, 1994.
- T. M. Over and V. K. Gupta. A space-time theory of mesoscale rainfall using random cascades. *Journal of Geophysical Research*, 101:26319–26331, 1996.
- R. Pastor-Satorras and R. H. Riedi. Numerical estimates of generalized dimensions $d(q)$ for negative q . *Journal of Physics A*, 29:391–398, 1996.
- H. O. Peitgen, H. Jürgens, and D. Saupe. *Chaos and Fractals - New Frontiers of Science*. Springer Verlag, 1992.
- J. B. Pesin. *Dimension Theory in Dynamical Systems*. University of Chicago Press, 1997.
- J. E. Pinzón, C. E. Puente M. B. Parlange, and W. Eichinger. A multifractal analysis of lidar measured water vapour. *Boundary-Layer Meteorology*, 76:323–347, 1995.
- A. Pitman, A. Henderson-Sellers, and Z. L. Yang. Sensitivity of regional climates to localized precipitation in global models. *Nature*, 346:734–737, 1990.
- J. Polcher, K. Laval, L. Dümenil, J. Lean, and P. R. Rowntree. Comparing three land surface schemes used in general circulation models. *Journal of Hydrology*, 180:373–394, 1996.
- L. F. Richardson. *Weather Prediction by Numerical Processes*. Cambridge University Press, 1926.

- R. H. Riedi. An improved multifractal formalism and self-similar measures. *Journal of Mathematical Analysis and Applications*, 189:462–490, 1995.
- P. R. Rowntree and J. Lean. Validation of hydrological schemes for climate models against catchment data. *Journal of Hydrology*, 155:301–323, 1994.
- D. Schertzer and J. Lovejoy. Resolution dependence and multifractals in remote sensing and geographical information systems, Lecture notes, McGill University, 1996.
- D. Schertzer and S. Lovejoy. The dimension of atmospheric motion. In *Turbulence and Chaotic Phenomena in Fluids*, IUTAM Symp, pages 141–144. Kyoto U, Japan, Elsevier North-Holland, New York, 1983.
- D. Schertzer and S. Lovejoy. Physical modeling and analysis of rain and clouds by anisotropic scaling multiplicative processes. *Journal of Geophysical Research*, 92:9693–9714, 1987.
- D. Schertzer, S. Lovejoy, F. Schmitt, Y. Chigirinskaya, and D. Marsan. Multifractal cascade dynamics and turbulent intermittency. *Fractals*, 5:427–471, 1997.
- W. J. Shuttleworth. Macrohydrology - the challenge for process hydrology. *Journal of Hydrology*, 100:31–56, 1988.
- G. Taylor. Statistical theory of turbulence. *Proceedings of the Royal Society of London A*, 164:476–490, 1938.
- G. Thomas and A. Henderson-Sellers. An evaluation of proposed representations of subgrid hydrologic processes in climate models. *Journal of Climate*, 4:898–910, 1991.
- D. Veneziano, R. L. Bras, and J. D. Niemann. Nonlinearity and self-similarity of rainfall in time and a stochastic model. *Journal of Geophysical Research*, 101:26371–26392, 1996.
- D. V. Widder. *The Laplace Transformation*. Princeton University Press, 1946.
- L. Xu, D. P. Lettenmair, and E. F. Wood. One-dimensional statistical dynamic representation of subgrid spatial variability of precipitation in the two-layer variable infiltration capacity model. *Journal of Geophysical Research*, 101:21403–21422, 1996.
- I. Zawadzki. Fractal structure and exponential decorrelation in rain. *Journal of Geophysical Research*, 92:9586–9590, 1987.